UNIVERSITY OF COPENHAGEN
FACULTY OF SCIENCE

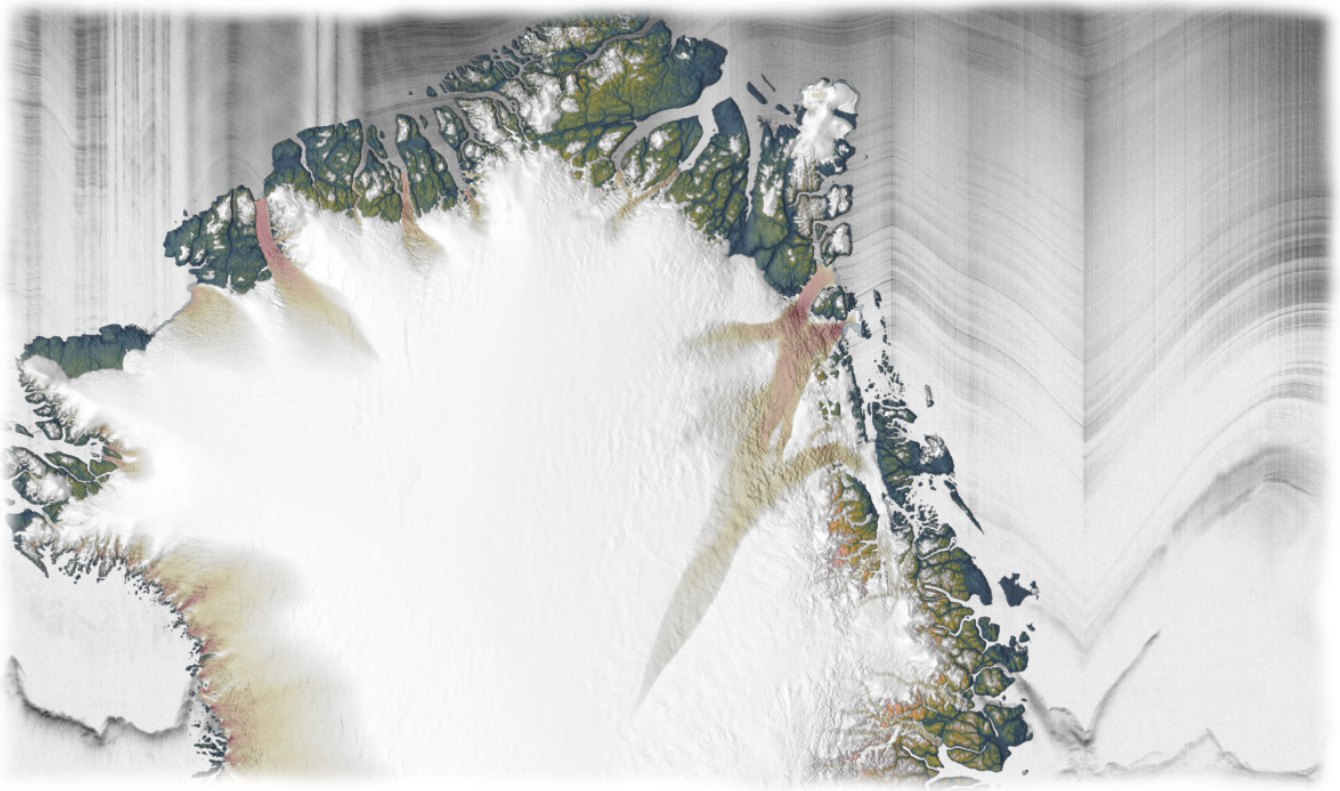

PhD thesis

Radar investigation of the Northeast Greenland Ice Stream

Deriving the crystal orientation fabric

Niels Fabrin Nymand

Supervisors: Dorthe Dahl-Jensen and Christine S. Hvidberg
International Supervisor: David A. Lilien

Submitted: December 20, 2024

This thesis has been submitted to the PhD School of The Faculty of Science, University of Copenhagen

Abstract

The Northeast Greenland Ice Stream (NEGIS) is the largest ice stream of the Greenland Ice Sheet, spanning over 600 km and with a drainage basin that covers 16% of the Ice Sheet. Dynamic mass loss currently accounts for around half of the total mass loss of the Greenland Ice Sheet and is primarily driven by ice streams that transport ice from the interior to the coast. Unlike most ice streams, NEGIS is not controlled by the basal topography, making it extremely difficult to model accurately. The crystal orientation fabric (COF), describing the way ice crystals are oriented within the ice, is known to be important for understanding the flow in ice streams, as the stiffness of ice can vary by two orders of magnitude depending on COF and the orientation of applied stress. The COF evolves differently under different strains making it valuable to get information about the flow history of a region. This thesis explores the use of polarized radar to study the COFs of NEGIS. In the summer of 2022, we conducted a comprehensive survey of NEGIS using a multi-polarized radar system that was meant to give unique insights into the dynamics of the ice stream. Two studies are presented based on this data.

In the first study, we developed a novel method for deriving the orientation and strength of the depth-averaged horizontal anisotropy of the COF from pairs of reflections that originate from the same physical layers. These "double reflections" are a direct consequence of the bulk birefringence of the ice that split incoming linearly polarized radar waves into two waves with different phase speeds. The results of applying this method reveal an asymmetry across the NEGIS center flow line that has not previously been observed. This asymmetry adds to growing evidence for a more variable ice stream than previously assumed.

In the second study, the task of deriving the COF is formulated as an inverse problem. Based on a simple model for radar propagation in birefringent ice, we are able to set up a simple inversion routine for the anisotropic scattering of the ice and orientation of the COF. The horizontal anisotropy as a function of depth is solved as a linear inverse problem based on travel time differences derived from cross-correlating co-polarized signals. Results from four different upstream locations relative to the EastGRIP ice core are presented. Generally the anisotropic scattering and COF orientation is enough to adequately explain observations. This is due to the strong birefringence that causes a loss of coherence. The locations show strong anisotropic scattering and COF orientations that are rotated between 2° and 10° relative to flow. The horizontal anisotropy generally agrees well with the EastGRIP ice core, suggesting a transition from a vertical girdle with a horizontal maximum to a fabric with weak horizontal anisotropy close to the base of the ice.

Resumé

Den nordøstgrøndlandske istrøm, forkortes NEGIS på engelsk, er den største isstrøm i Grønland og strækker sig over mere en 600 km og står for 16% af Indlandsisens samlede afløbsareal. Dynamisk massetab udgør omkring halvdelen af det samlede massetab fra Indlandsisen og drives primært af isstrømme, der transporterer is fra de centrale regioner af Indlandsisen og ud til kysten. I modsætning til de fleste andre isstrømme er NEGIS ikke kontrolleret af bundtopografien, hvilket gør det vanskeligt at modellere. Orienteringen af iskrystalstrukturen, der beskriver hvordan iskrystaller er orienteret i isen, spiller en vigtig rolle i forståelsen af isstrømmes bevægelse, da isens stivhed kan variere med op til to størrelsesordener afhængigt af iskrystalstrukturen. Iskrystalstrukturen udvikler sig forskelligt under forskellige deformationsforhold, hvilket betyder at den kan indeholde information om områdets strømningshistorik. Denne afhandling undersøger brugen af polariseret radar til at studere iskrystalstrukturen i NEGIS. I sommeren 2022 gennemførte vi en omfattende undersøgelse af NEGIS med et multipolariseret radarsystem, der skulle give unikke indsigter i isstrømmens dynamik. Ud fra disse data præsenteres to studier.

I det første studie udviklede vi en ny metode til at udlede orienteringen og styrken af den horisontale anisotropi af krystalstrukturen fra par af refleksioner, der stammer fra de samme fysiske lag. Disse "dobbelte refleksioner" er en direkte konsekvens af isens dobbeltbrydnings egenskaber, der opdeler lineært polariserede radarbølger i to bølger med forskellige fasehastigheder. Resultaterne udledt af metoden viser en asymmetri på tværs af NEGIS' centrale flydelinje, som ikke tidligere er blevet observeret. Denne asymmetri føjer til det allerede voksende evidensgrundlag for, at isstrømmen er mere variabel, end tidligere antaget.

I det andet studie beskriver vi bestemmelsen af iskrystalstrukturen som et invers problem. Baseret på en simpel model for radarbølgers udbredelse i is er vi i stand til at opstille en simpel inversionsalgoritme for den anisotropiske spredning og orienteringen af isens krystalstruktur. Den horisontale anisotropi, forskellen mellem isens to brydningsindeks, som funktion af dybden løses som et lineært invers problem, baseret på tidsforskelle der er udledt ved at krydskorrelere copolariserede signaler. Der præsenteres resultater fra fire forskellige opstrømslokationer i forhold til EastGRIP iskernen. Generelt er den anisotropiske spredning og iskrystalorienteringen tilstrækkelig til at forklare observationerne. Dette skyldes den store forskel i brydningsindeks, der forårsager et tab af kohærens. Lokationerne viser stærk anisotropisk spredning og en krystalstruktur der er roteret mellem 2° og 10° i forhold til flyderetningen. Den horisontale anisotropi stemmer generelt godt overens med EastGRIP iskernen og antyder en overgang fra en krystalstruktur med en stor horisontal anisotropi til en med lille horisontal anisotropi tæt på bunden af isen.

Acknowledgments

First and foremost, I want to express my gratitude to my principal supervisor, Dorthe Dahl-Jensen, for her guidance and support throughout this PhD. Her trust in my work and encouragement to pursue my own ideas have been instrumental in shaping me as an aspiring scientist. Despite her incredibly demanding schedule, she always found time for insightful meetings. I am especially thankful for the opportunities to participate in fieldwork and experience some of the most remote and astonishing places on Earth.

I would also like to extend my deepest thanks to David A. Lilien, whose incredible expertise and willingness to help have been a cornerstone of my PhD. From troubleshooting code to navigating the challenges of peer reviews and even crevasse rescue drills in his driveway, his vast knowledge of ice flow and radioglaciology has been truly inspiring.

To Christine S. Hvidberg, thank you for encouraging me to apply for this PhD in the first place. I never imagined that I would venture into the world of glaciology when I first started studying physics, but I am extremely happy I did. Your enthusiasm for the field is very contagious, and your drive is inspiring. Thank you for all the help and guidance throughout this PhD.

To my colleagues at PICE, thank you for making it a pleasure to come to work every day. I am especially grateful to my fellow PhD students for sharing the highs and lows of academic life and to my office mates Mikkel, Dina, and Miguel for making our shared space a fantastic place to work.

Lastly, I want to acknowledge the support of my family and friends. Their encouragement and understanding provided the foundation for me to focus on and achieve this goal.

Abbreviations

ADC	Analog-to-digital convert
ApRES	Autonomous phase-sensitive radio-echo sounder
c-axis	Crystallographic axis, optical axis
COF	Crystal orientation fabric
DAC	Digital-to-analog converter
EastGRIP	East Greenland Ice Core Project
FMCW	Frequency-modulated continuous wave
GRIP	Greenland Ice Core Project
IRH	Internal reflection horizons
NEEM	North Greenland Eemian Ice Drilling
NEGIS	Northeast Greenland Ice Stream
pRES	Phase-sensitive radio echo sounder
RES	Radio echo sounder
SAR	Synthetic aperture radar
UHF	Ultra high frequency
UWB	Ultra wide band

Polarization definitions

V	V-polarization. Along-track polarization
H	H-polarization. Across-track polarization
HH	Transmit at H and receive at H
HV	Transmit at H and receive at V
VV	Transmit at V and receive at V
VH	Transmit at V and receive at H
co-polarized	Transmit and receive at the same polarization (HH and VV)
cross-polarized	Transmit and receive at orthogonal polarizations (HV and VH)

Contents

List of Figures

Chapter 1

Introduction & Background

The Cryosphere

The cryosphere refers to the frozen component in the Earth system (IPCC, 2022) and includes snow, sea ice, glaciers, ice sheets, permafrost, and more. While the cryosphere is mostly concentrated in the polar and high mountainous regions, the changes in these regions can be felt all over. The Earth's climate system is a balance between the incoming energy from the sun and energy returned to space by the Earth. Part of the solar radiation is reflected by the surface of the Earth, and the cryosphere plays an important role in this due to the high albedo of snow and ice. Changing any component of the energy balance means that the Earth has to either heat or cool to compensate. A changing cryosphere due to climate change can be amplified or reduced by feedbacks in the climate system. Rising temperatures reduce the time with snow on the ground and ice on the ocean, reducing the amount of energy reflected back out of the Earth's system, leading to an energy imbalance causing increasing temperatures and melting. This feedback mechanism can also be flipped by an increasing snow and ice extent causing cooling. Melting of the two largest ice masses on Earth, the Greenland and Antarctic ice sheets, not only reduces the volume of the cryosphere but also increases the ocean area and volume, which, unlike the cryosphere, is very good at absorbing the energy from the sun. Of course, this is only one feedback mechanic in the cryosphere and climate system, and if the balance is this delicate, the Earth would be completely glaciated or completely ice-free.

Recent history of ice on Earth

For the past 2.6 million years, the Earth has been in an ice age known as the Quaternary (Ehlers & Gibbard, 2011) period, consisting of a series of colder (glacial) and warmer periods (interglacial). Our current interglacial period, the Holocene, started around 11.7 thousand years (kyr) ago at the end of the last glacial that started around 115 kyr ago (NEEM community members, 2013). These climatic fluctuations have been

characterized by a 41 kyr cycle for the first part of the Quaternary but switched to a 100 kyr cycle in the past 800 kyr (Ehlers & Gibbard, 2011), allowing for a much wider expansion of glaciers and ice sheets. Ice age cycles have been tied to changes in orbital parameters of the Earth (eccentricity, obliquity, and precession), which cause fluctuations in the solar energy in The Northern Hemisphere, which can then trigger the feedback mechanism described above (Rapp, 2011). During the coldest period of the last glacial, The Last Glacial Maximum, the sea level was about 125-130 meters lower (Yokoyama et al., 2018), and most of this water was being stored in massive ice sheets covering large chunks of Northern Europe and North America. This has left behind traces that can still be seen today, like moraines, lakes, and valleys forming the current landscape, isostatic adjustment causing large landmasses to lift and depress, and boulders located far from their origin. At the termination of the last glacial period, the large ice sheets over Europe and North America retreated, with two large ice sheets remaining: Greenland and Antarctica. Some evidence shows that around 8-5 kyr ago, the Greenland Ice Sheet had retreated to an ice volume smaller than today, followed by a re-advance to a maximum Holocene extent around 1450-1850 CE, and the Antarctic ice sheet had reached its current position 5 kyr ago (IPCC, 2023).

Current state of ice on Earth

Currently, we are seeing a global retreat in land and sea ice attributed to anthropogenically driven climate change (IPCC, 2023). Simply put, ice sheets, ice caps, and glaciers have to be in a balance between mass accumulated through snowfall and mass lost through melt, sublimation, and calving to keep their size. Increasing temperatures will change this balance, which is also what we observe as a consequence of climate change. It is not given that an increase in temperature will result in a net loss, as a warmer atmosphere can also contain more moisture, which can increase accumulation. Nevertheless, what is being observed is a retreat of most mountain glaciers and ice caps and a negative mass balance of the Greenland and Antarctic ice sheets. Since 1901, the two largest contributors to sea level change, excluding the thermal expansion of the oceans, have been glaciers and the Greenland Ice Sheet, contributing with around 70 mm and 40 mm of sea level change respectively (IPCC, 2023). The glaciers, not including glaciers in Antarctica and Greenland, have in a period between 1901 to 2009 been estimated to have reduced in volume by almost 20% (Marzeion et al., 2012).

The future for ice on Earth

The future for ice on Earth, in the form of glaciers, ice caps, ice sheets, and sea ice, is extremely uncertain, but it has a very important role in the bigger climate system. The two polar ice sheets have enough freshwater stored to raise the global sea level by more than 60 meters (Morlighem et al., 2017), making them the largest potential contributors to future sea level rise. Currently, Greenland is the main driver of sea level change of

the two, but the potential of Antarctica is massive (IPCC, 2023).

The Greenland Ice Sheet

The Greenland Ice Sheet is the largest ice mass in the Northern Hemisphere and has been studied extensively in recent decades.

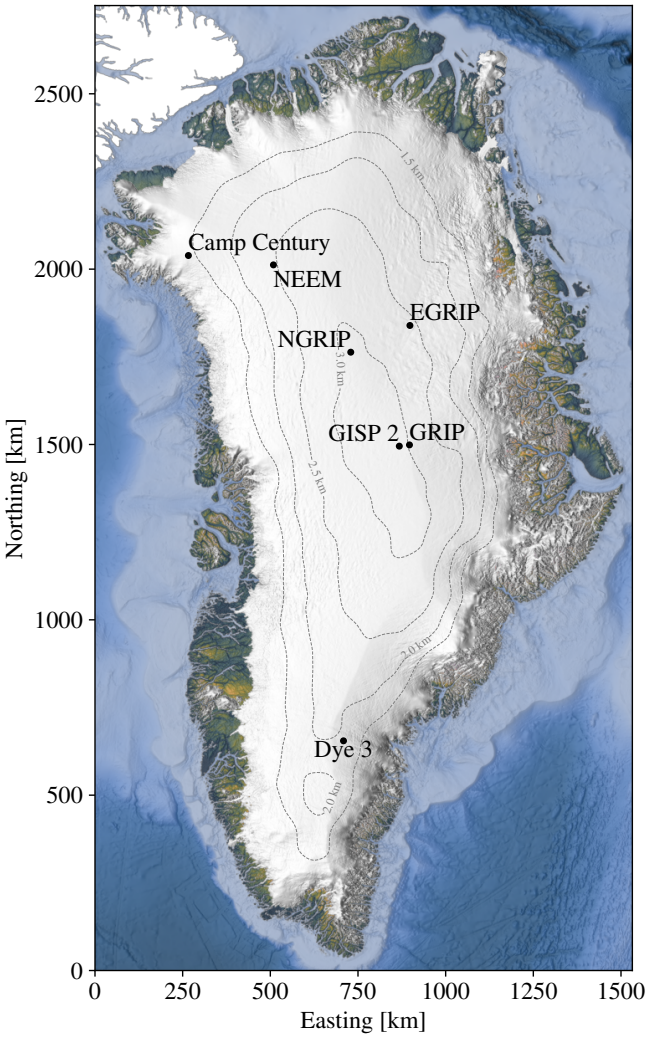

Figure 1.1: Map of Greenland and deep drilling projects. Contours show the ice thickness (Morlighem, 2022)

The ice sheet is about 2000 km north to south, 1000 km east to west, and up to more than 3 km thick, resulting in a freshwater storage equivalent to raising the global sea level by 7.4 m (Morlighem et al., 2017). Being able to predict its future in a warming world is therefore of great interest, and the first step in that process is to look into its past. Because ice sheets and glaciers are grown from the surface via precipitation year after year, the deeper we go, the further back in time we can look. The isotopic composition of the water molecules gives us a proxy for the temperature at deposition (Dansgaard et al., 1969). After the snow has been compressed into ice under the weight of the subsequent year's snowfall, the air bubbles trapped inside the ice are small samples of the past atmosphere. Not only can we learn something about the past ice sheet but also about past climatic conditions. Many ice coring projects in Greenland aim to get a good climate record as far back in time as possible, starting with the ice core drilled at the American military base Camp Century (Dansgaard et al., 1969). In the NEEM ice coring project (NEEM community members, 2013), they were able to reconstruct the temperatures as far back as the last inter-glacial period (the Eemian), providing valuable information about what conditions the ice sheet has been subjected to in the past. Another important reason to drill ice cores is to better understand the physical properties of the ice,

which help inform and constrain ice flow models that are used to reconstruct the past and predict the future of the Greenland Ice Sheet under different warming scenarios (IPCC, 2023).

Ice dynamics

While we usually think of ice as being a solid, ice behaves like a very viscous fluid as it slowly deforms under applied stress in a process known as *creep* (Cuffey & Paterson, 2010) or ice flow. Ice found in glaciers and ice sheets is a polycrystalline material, and the flow properties are a mixture of the single crystal properties and the interactions between the crystals.

Single crystal deformation

The water molecules in ice found in glaciers and ice sheets are arranged in layers of hexagonal rings (Cuffey & Paterson, 2010)[1], where the plane parallel to these layers is called the *basal plane* of the crystal. The normal vector to the basal plane is referred to as the *c-axis*, which is also the optical axis of the crystal. The deformation of single crystals is dominated by slip parallel to the basal planes (Duval et al., 1983), called *basal slip*, see figure 1.2. This process was first described in 1891 by James McConnel (McConnel, 1891), where he noticed a very rapid deformation of a single ice crystal under load. He noted that "*the crystal had behaved as if it consisted of an infinite number of indefinitely thin sheets of paper*", giving rise to the often used deck of cards analogy. Two other slip systems exist but are extremely difficult to activate as even a small misalignment of the setup will yield basal slip (Duval et al., 1983). This strong preference for basal slip translates into ice being a highly anisotropic material.

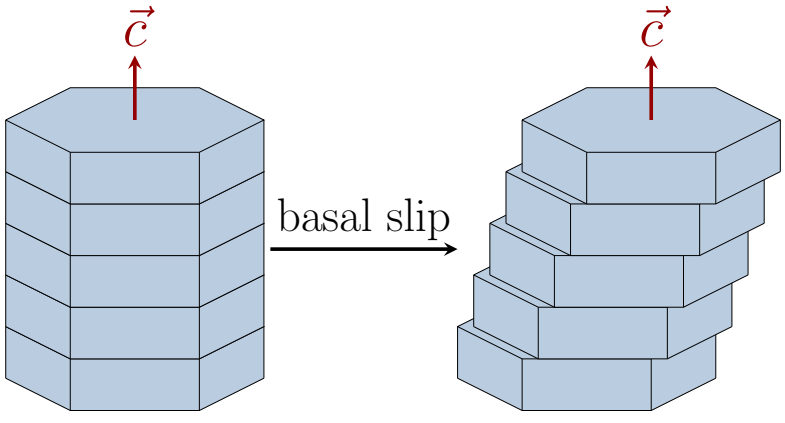

Figure 1.2: Illustration of basal slip in a single crystal consisting of five hexagonal layers. $\vec{c}$ is the c-axis of the crystal.

[1]This is not necessarily true for all ice, but ice found in glaciers and ice sheets are predominately of the type Ih, which is a hexagonal crystal

Polycrystalline deformation

The deformation of polycrystalline ice is much slower than single-crystal deformation. The intuitive explanation for this is that crystals are being confined by neighboring crystals resisting any movements (Glen, 1975). Neighboring crystals may also differ in orientation, making basal slip for a given stress configuration difficult for one crystal and easy for another. In fact, because basal slip is so dominating and slip between crystal boundaries is also fairly easy, a sample of polycrystalline ice can accommodate deformation by basal slip by having the crystals rotate away from tensional axes (Alley, 1992). A simple sketch of crystal rotation for polycrystals subjected to uniaxial tension is shown in figure 1.3.

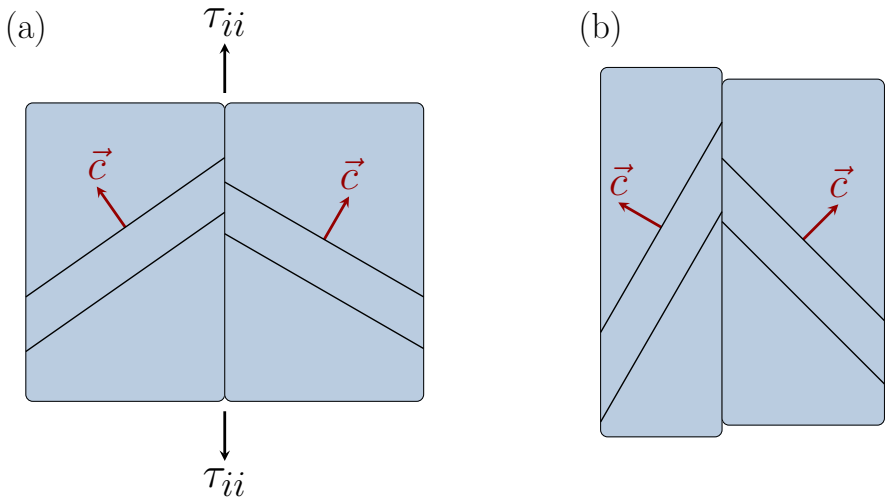

Figure 1.3: Sketch inspired by Alley (1992) of crystal rotation from polycrystal deformation. (a) shows two crystals under uniaxial tension, τ_{ii}, just before deformation. (b) shows deformation accommodated by basal glide and rotation of the c-axes.

This mechanism offers an explanation for how polycrystal deformation is related to single-crystal deformation, in that a rotation of the c-axis must follow if we only allow slip along the basal planes. A consequence of this is that "*c-axis always rotate towards the compressional axes and away from tensional axes*" (Alley, 1992). In this context, isotropic ice is polycrystalline ice where the c-axes of the individual crystals are uniformly distributed on a unit sphere, i.e., there is no preferred orientation. In experiments, it is possible to show how isotropic ice can develop a preferred orientation with increasing strain (Azuma & Higashi, 1985). On scales much larger than individual crystals, the distributions of crystal orientations are often referred to as *crystal orientation fabrics* (COFs), crystallographic preferred orientations (CPOs), or sometimes simply *fabrics*. Two other important mechanisms for altering the COF are *rotational recrystallization* and *migration recrystallization*. Rotational recrystallization is when sub-grains (crystals) form close to the grain boundaries with orientations that are similar but not exactly the same as their parent grains (Richards et al., 2021). The effect of

rotational recrystallization is an outward diffusion of the c-axis orientation away from the initial orientations (Richards et al., 2021). Migrational recrystallization is a process where crystals grow into neighboring crystals depending on their difference in deformation energy stored in the dislocations within the respective crystals (Richards et al., 2021). The effect of migrational recrystallization is an increase in the COF intensity along the orientation of the migrating crystal.

Ice flow

The internal deformations of the polycrystals constitute a flow under applied stress. From experiments Glen (1952) was able to show that there exists a non-linear relationship between the strain rate and stress, and came up with the relation,

$$\dot{\epsilon} = A\tau^n \tag{1.1}$$

where $\dot{\epsilon}$ is the strain rate, τ is shear stress, n is the creep exponent and A is a prefactor that depends strongly on temperature and fabric (Cuffey & Paterson, 2010). While Equation 1.1 is often referred to as Glen's Law, it is an empirical fit to the laboratory results where he first found $n = 4$ (Glen, 1952), and later $n = 3.2$ (Glen, 1955), and thereby demonstrating that ice is a non-Newtonian fluid. Equation 1.1 only describes a single component stress, but for real glaciers and ice sheets, the stress acts in all three dimensions. A generalized Glen's Law, also called the Nye-Glen Isotropic Law, developed by (Nye, 1957), can be written as,

$$\dot{\epsilon}_{ij} = A\tau_E^{n-1}\tau_{ij} \tag{1.2}$$

where $\dot{\epsilon}_{ij}$ and τ_{ij} are the (i^{th}, j^{th}) components of the strain rate and deviatoric stress tensors, respectively. Deviatoric refers to the stress that deviates from the mean normal stress (pressure), $\tau_{ii} = \sigma_{ii} - \frac{1}{3}(\sigma_{xx}+\sigma_{yy}+\sigma_{zz})$, where $\boldsymbol{\sigma}$ is the true stress tensor. Because ice is incompressible, the pressure does not contribute to the deformation. τ_E is the second invariant of the stress tensor, also called the effective stress. The first invariant is the trace of $\boldsymbol{\tau}$, which must be zero due to the assumption of incompressibility. A consequence of $n \neq 1$ is that the viscosity of ice, $\eta = \frac{1}{2}(A\tau_E^{n-1})^{-1}$, depend on the effective stress (Cuffey & Paterson, 2010). Ice becomes softer as the stress increases.

Anisotropy

While equation 1.2 is the most commonly used flow law for ice, it ignores an inherent property of ice - it is anisotropic. In other words, for anisotropic COFs, the viscosity depends - not only on the magnitude - but also on the orientation of the stress. The stiffness of glacier ice with a strongly developed COF has been measured to vary by 2 orders of magnitude for different orientations of the applied stress (Shoji & Langway, 1988). The crystal orientation fabric is often presented as Schmidt diagrams, defined

as an equal area projection of the c-axes intersection with the surface of a sphere, or sometimes just as an orthographic projection of the orientation density plotted on a sphere. Only one hemisphere needs to be projected due to the antipodal symmetry of the ice crystals. When reporting the c-axis measurements for a sample, it is common to use normalized eigenvalues of the second-order structure tensor, sometimes called the orientation tensor (Woodcock, 1977). Following Advani and Tucker (1987), the second-order structure tensor can be written in terms of the c-axis as follows,

$$\langle \mathbf{c}^2 \rangle = \langle \mathbf{c} \otimes \mathbf{c} \rangle = \int_{\phi=0}^{2\pi} \int_{\theta=0}^{\pi} \hat{\mathbf{c}} \otimes \hat{\mathbf{c}} \rho(\theta, \phi) \sin(\theta) d\theta d\phi \tag{1.3}$$

where $\hat{\mathbf{c}} = [\sin\theta\cos\phi, \sin\theta\sin\phi, \cos\theta]^T$ is an arbitrary c-axis written in terms of θ and ϕ, $\rho(\theta, \phi)$ is a density function defined such that $\rho(\theta, \phi)\sin(\theta)d\theta d\phi$ is the probability of finding a crystal c-axis within $[\theta, \theta + d\theta]$ and $[\phi, \phi + d\phi]$. $\otimes$ is the dyadic (outer) product. The second-order structure tensor reduces the information from the density function into a single second-order tensor. In the process, we lose information about the distribution, and higher-order structure tensors are needed to capture complex distributions (Advani & Tucker, 1987). The eigenvectors of $\langle \mathbf{c}^2 \rangle$ $(\mathbf{e}_x, \mathbf{e}_y, \mathbf{e}_z)$ define the principal axes of the COF, and the corresponding eigenvalues $(\lambda_x, \lambda_y, \lambda_z)$ are used to characterize the anisotropy of the COF. The eigenvalues are usually normalized such that $\lambda_x + \lambda_y + \lambda_z = 1$. See figure 1.4 for examples of COFs commonly found in glaciers and ice sheets constructed from the eigenvalues and eigenvectors of $\langle \mathbf{c}^2 \rangle$.

Observations

When working with any model, whether it is Glen's flow law for modeling ice sheets or a weather forecast model, one of the most important components is to have observations. If we do not know how the weather is when we start doing the forecast, our starting point is wrong, and the forecast will most certainly be wrong, even if the model is representing real-world physics accurately (which, of course, is never completely true). In this section, I will give a small overview of three observational methods, among many others, that are used to gain insights into glaciers and ice sheets, specifically the Greenland Ice Sheet, and are used to improve ice flow modeling.

Ice cores

The most direct way of getting information from the deeper parts of the ice is to drill ice cores and bring the ice to the surface for investigation. During the sixties, the U.S. Army Cold Regions Research and Engineering Laboratory drilled an ice core all the way through the 1390m thick ice at Camp Century. The ice core was later analyzed by Willi Dansgaard together with Sigfús J. Johnsen, Jørgen Møller, and Chester C. Langway for its heavy water isotope composition from which they were able to reconstruct a climate

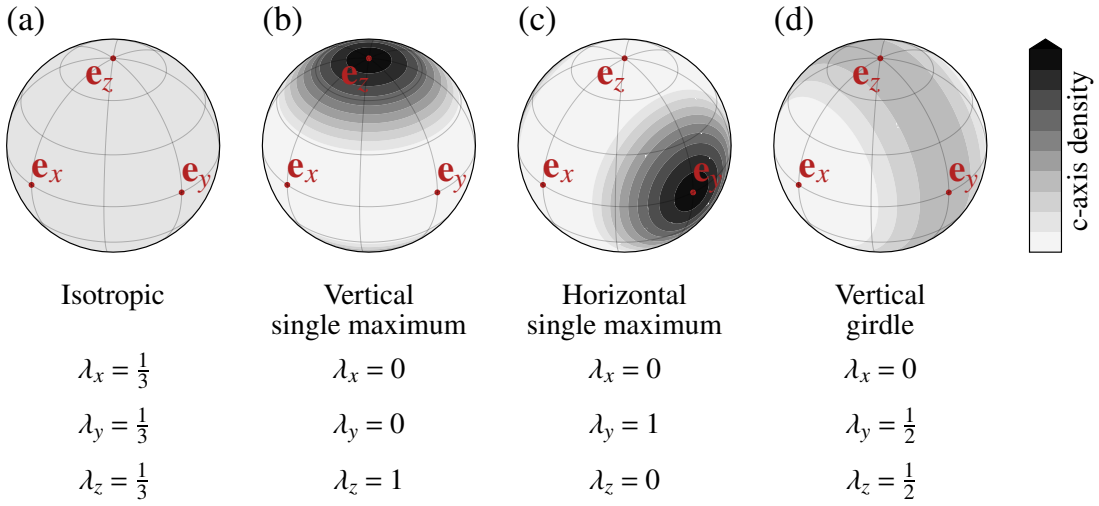

Figure 1.4: Four common COFs found in glaciers and ice sheets generated from the second-order structure tensor with the indicated eigenvalues and plotted using an orthographic projection. For the naming, $\mathbf{e}_z$ is assumed to be vertical. (a) uniform c-axis density, or isotropic COF, is often seen close to the surface. (b) A single vertical maximum is often seen at slow-flowing ice, caused by vertical compression aligning the c-axis. (c) A horizontal single maximum can be found at high shear zones, such as shear margins. (d) The vertical girdle can be found where there is an extensional flow, like an ice stream, causing the c-axis to rotate away from the tensional axis.

record for the past almost 100,000 years (Dansgaard et al., 1969). The Greenland and Antarctic Ice Sheets have a climate archive stored inside, which has sparked many deep ice-coring projects. Water isotopes stored in the ice not only contain information about the climate but also information about the surface elevation of the Greenland Ice Sheet when the snow was deposited (Vinther et al., 2009), which can work as an important constraint to ice flow modeling efforts to reconstruct the past ice sheet (Tabone et al., 2024; Lauritzen et al., 2024). Physical properties of the ice, like crystal size and orientation, are also recorded and provide very important data when calibrating and validating anisotropic ice flow models (Richards et al., 2023; Gerber et al., 2023; Lilien et al., 2023).

Seismics

One major limitation of ice cores is that they only provide information at a single point in the horizontal plane, and due to the cost and time associated with drilling a deep ice core - they are also very rare. There is no method that can get as much information about the ice as an ice core, but depending on what you want, other methods provide much cheaper and faster alternatives. For the case of learning about crystal orientation fabrics, an alternative to ice cores could be seismic data. Just like ice has anisotropic rheology due to the strong preference for basal-slip of individual crystals, ice is also

elastically anisotropic. Wavelengths of typical seismic waves are much larger than the common crystal size. Therefore, it is appropriate to consider the bulk anisotropy, or the COF, when deriving the elasticity tensor (Diez et al., 2015). In general, seismic waves propagate through an elastic medium as three different wave modes, one pressure wave (P-wave) and a shear wave (S-wave)[2] which can be resolved into a horizontal and a vertical component (sometimes referred to as SH and SV)(Lautrup, 2019). A common method for characterizing the COF of anisotropic materials from seismic data is to look at travel-time anomalies from shear-wave splitting, where the shear wave is split into two components with different phase velocities (Wuestefeld et al., 2010; E. C. Smith et al., 2017). Other properties can also be derived from seismic data, like the density of the firn layer (Fichtner, Hofstede, N. Kennett, et al., 2023) and basal conditions (A. M. Smith, 1997). Setting up a seismic survey requires geophones installed in the snow/firn to get a mechanical coupling with the ice below and then either wait for earth- or ice-quakes or have an active source like an explosion. An alternative to traditional three-component seismographs is optical fibers, which can more easily be placed over a large area or down an ice core borehole (Fichtner, Hofstede, N. Kennett, et al., 2023; Fichtner, Hofstede, Gebraad, et al., 2023).

Radar

Seismic data can potentially provide detailed estimates of the COF, but they are limited in their coverage, as installing instruments on the surface is required. The third and last method can cover large areas as it enables data recording while moving. By now, we have established that ice is anisotropic in terms of rheology and elastic properties. It is, therefore, not a surprise that ice is also optically anisotropic, or more specifically - ice crystals are birefringent. In the next chapter, I will give a more detailed walk-through of the theory of *ice sounding*. Radars used for ice sounding generally use frequencies between $\sim$ 10 MHz and $\sim$ 1 GHz as ice is effectively transparent in this range (Plewes & Hubbard, 2001). Internal reflections, often referred to as internal reflection horizons (IRH), are caused by sudden changes in the complex permittivity of ice (Fujita & Mae, 1994). It is believed that there are three main mechanisms controlling formations of IRH - changes in density, acidity, and crystal orientation fabric (Fujita et al., 1999). If an IRH can be related to a specific event, like a volcanic eruption, for example, it is called an isochrone, which can be used to extend the depth-age scale from ice cores to the rest of the ice sheet (MacGregor et al., 2015; Lilien et al., 2021; Gerber et al., 2021). One of the main advantages of using radar to investigate glaciers and ice sheets is the logistically simple setup. A radar, consisting of a transmitter, receiver, and antenna panels, can be flown or driven across the surface of the ice while recording internal reflections from the ice or from the ice-base interface.

[2] P originally stands for primary and S for secondary, which refers to the arrival times of the two wave types when recording an earthquake on a seismogram.

The Northeast Greenland Ice Stream

There is no clear definition of what an ice stream is, but one definition from Cuffey and Paterson (2010) is: "*A region of grounded ice sheet in which the ice flows much faster than in the regions on either side*". In between the fast-flowing ice and the slow-moving surroundings are the shear margins, which are characterized by high gradients in the horizontal flow field. A common feature for most ice streams is that their flow is topographically constrained by troughs in the bed (Cuffey & Paterson, 2010). However, one exception to this is the Northeast Greenland Ice Stream (NEGIS), first identified by Fahnestock et al. (1993) from surface features derived from satellite images. The ice stream extends all the way from the coast to the ice divide of the Greenland Ice Sheet, more than 600 km, and its drainage basin covers 16% of the ice sheet (Khan et al., 2014), making it a significant factor in the total mass balance of the Greenland Ice Sheet. Figure 1.5 shows satellite-derived surface velocities for all of Greenland (a) and NEGIS (b). The high velocities far inland contrast with the otherwise slow moving ice surrounding the ice stream. In an effort to better understand ice streams, the East Greenland Ice Core Project (EastGRIP or EGRIP) set out for the first time to drill an ice core to the base of an active ice stream (Vallelonga et al., 2014). Having a camp inside an ice stream has also supported many projects, such as seismic and radar surveys focused on understanding and gathering data on ice streams (Franke et al., 2020; Zeising et al., 2023; Fichtner, Hofstede, Gebraad, et al., 2023; Gerber et al., 2023; Jansen et al., 2024)

The origins of NEGIS are still debated, but one hypothesis is a geothermal hotpot at the onset of the ice stream. Based on simple ice flow models together with radar-derived IRH Fahnestock et al. (2001) found basal melt rate at the onset of NEGIS of 0.1 m/yr, which would require a heat flux of 970 $\mathrm{mWm^{-2}}$ at the base. A different radar study of the basal conditions at NEGIS found similar melt rates inside the ice stream (Keisling et al., 2014). A later modeling study by Smith-Johnsen et al. (2020) supported the geothermal heat flux of 970 $\mathrm{mWm^{-2}}$. They found it to be the minimum heat flux that could reproduce surface velocities of NEGIS and suggested that a geothermal source in conjunction with hydrothermal circulation could explain this. In response to Smith-Johnsen et al. (2020) Bons et al. (2021) argued that a heat flux of 970 $\mathrm{mWm^{-2}}$ would be geologically unique and is incompatible with any known geological processes, even if multiple processes are working together. Another piece of evidence against the hypothesis of geothermal hotspots is the discovery of a now-extinct NEGIS-type ice stream well north of the current NEGIS (Franke, Bons, et al., 2022). A coarse dating of the extinct ice stream suggests it was active during the Holocene and perhaps active at the same time as NEGIS. A localized geothermal hotspot under the onset of NEGIS would thereby not explain the initialization of the now-extinct ice stream. While a geothermal hotspot may not alone explain NEGIS, the modeling results of Smith-Johnsen et al. (2020) show that something exceptional is needed to initiate a NEGIS-

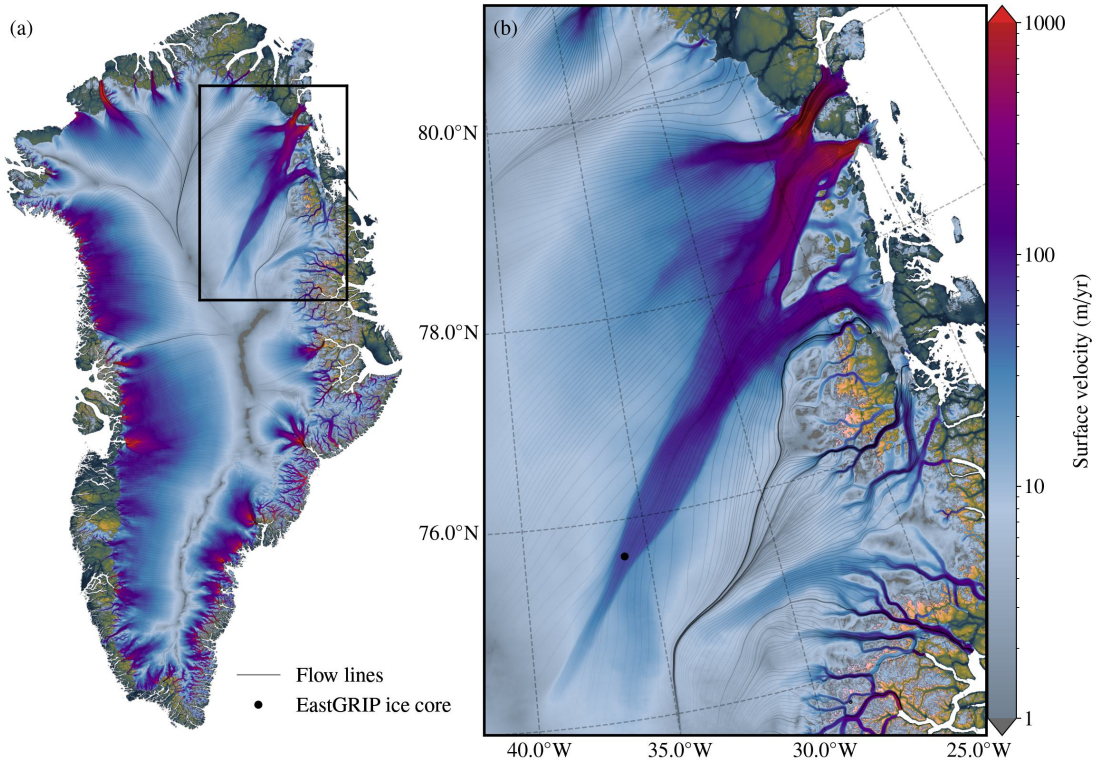

Figure 1.5: Surface velocity of the Greenland Ice Sheet (Joughin et al., 2018) (a), and the surface velocity zoomed in on the Northeast Greenland Ice Stream (b). The location of the EastGRIP ice core site is marked with a black dot.

type flow, and being able to capture it is essential for being able to do accurate modeling of the Greenland Ice Sheet. A recent study by Jansen et al. (2024) found that the shear margins at NEGIS are around 2000 years old. This would mean that the present ice steam configuration is potentially quite young and has changed flow configuration in the recent past. This, together with findings of accelerating shear margins from Grinsted et al. (2022), suggest that NEGIS is not done evolving, highlighting the importance of better understanding the processes driving and initiating an ice stream like NEIGS if we are to predict the future of the Greenland Ice Sheet. The current flow can be modeled by inverting for the basal friction from the surface velocities, thereby fitting the model to the current surface velocity field. However, when modeling the flow inside an ice stream, one has to be careful. As discussed earlier, the deformation of polycrystals will tend to align c-axes along the compressional axis or away from the tensional axis. Flowlines converge at the ice stream, and inside the ice stream, the ice is sped up, causing extensional stresses. Following the rule of c-axis alignment to compression, we would expect a crystal orientation fabric inside the ice stream to form a circle that is normal to the flow direction, also called a girdle fabric. The girdle fabric hardens the ice to further deformation. Outside the ice stream, we have "normal" glacier conditions where ice is mainly deformed by gravity, causing a vertical alignment, or vertical single

maximum fabric. At the shear margin, things are slightly less intuitive to explain as the compressional or extensional axis is not as easy to visualize. If we assume that the stress on a parcel of ice can be explained by only two non-zero components in the stress tensor, $\tau_{xy} = \tau_{yx}$, the strain would be equivalently explained by compression/extension at a 45-degree angle. However, the real strain experienced by the parcel of ice is a mix of this and a rotation caused by the non-zero vorticity in the velocity field. The result will be a horizontal single maximum pointing to the shear plane at some angle. This can soften the shear margins to shear deformation. Not including the hardening and softening processes of the ice in ice flow models can, for example, result in misleading basal conditions based on inversion techniques (Rathmann & Lilien, 2022). However, a very good reason not to include this is the added computational complexity and the lack of COF observations. A simple sketch of the flow and the three fabric types in and around an ice stream is shown in figure 1.6. The exterior ice is characterized by slow-moving ice frozen to the bed, causing a vertical gradient in the horizontal velocity field. The interior is fast-flowing ice gliding over the bed due to melt water lubrication.

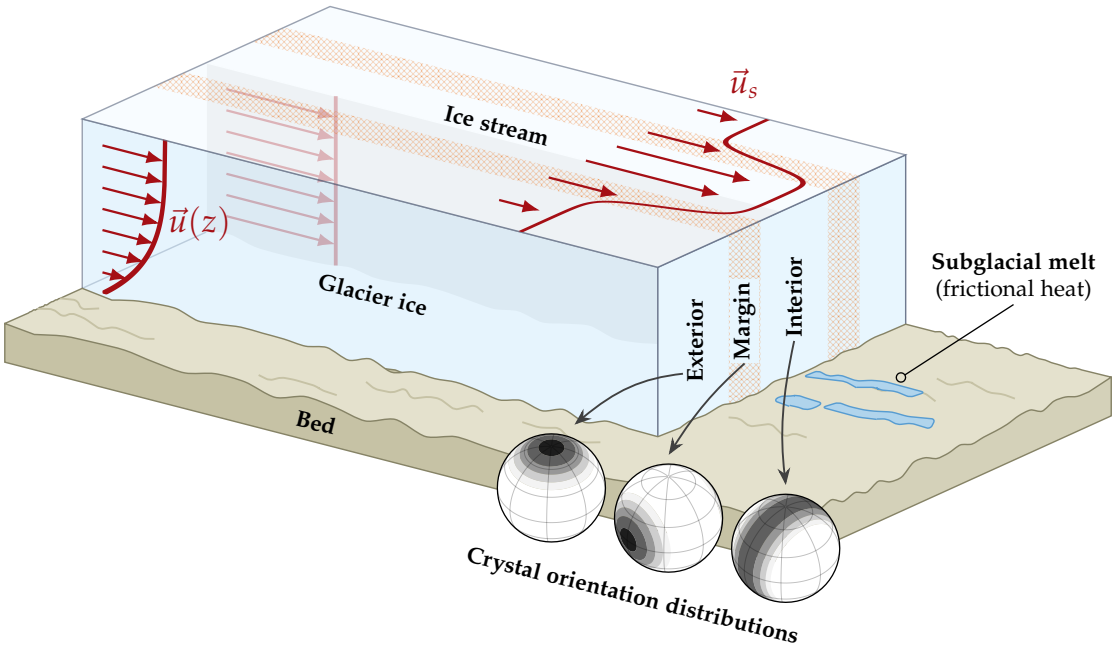

Figure 1.6: Simple sketch of a NEGIS-type ice stream without any topographical constraints. Red arrows and solid lines show a velocity curve at the surface, $\vec{u}_s$, and as a function of depth, $\vec{u}(z)$.

Chapter 2

Ice sounding

Sounding refers to transmitting a signal through a media and waiting for the signal to be reflected and returned to a receiver that records the *echo*. An example could be depth sounding to determine ocean bathymetry by transmitting acoustic waves (sound) through the water column and recording the return time of the echos generated from contrasting acoustic properties of the water and the ocean bed. A different approach to sounding is to use radio waves, also called *radio-echo sounding* (RES), where acoustic waves are replaced by electromagnetic waves at radio frequencies. Ice sounding is the use of radio waves to sound ice. As mentioned in the previous chapter, ice sounding is done with specially designed radars. Radars that we find at the airport or on ships are designed to scan the surroundings and track moving objects, but ice sounding radars are, in a way, much simpler, as they always transmit and receive from the same direction. One of the most common use cases for ice sounders is to retrieve information about the depth of the ice and the basal topography by timing the arrival of the basal reflector. The base of the ice is a very strong reflector, but also internal reflectors have been showing up on the *echograms* since the first radar surveys of Greenland in the 60s and 70s (Gudmandsen, 1975). Radars have been used to propose new drill sites (Dahl-Jensen et al., 1997; Vallelonga et al., 2014), as they are a cheap and fast way to get information about the depth and approximate age of the ice by transferring a time scale from an existing ice core to a new location via IRHs and ice flow models (Buchardt & Dahl-Jensen, 2008; Lilien et al., 2021). This chapter aims to give the theoretical background on electromagnetic wave propagation in ice, from the governing equations to the birefringence of single ice crystals to the propagation of radio waves in polycrystalline ice, and the basics of how an ice sounder works. The general theoretical background is a mix of relevant chapters from two textbooks, Introduction to Electrodynamics by Griffiths (2013) and Optics by Hecht (2017), and then related to single ice crystals and polycrystalline ice. The motivation for this chapter is to provide the background for the fundamental physics on which this thesis and ice sounding in general, rests.

Electromagnetic wave propagation in ice

We usually think of ice as being transparent because we can see through the ice on a lake or an ice cube, however even small impurities can make ice cloudy for visible light. Adding snow and firn on top of the ice makes it impossible to see through glaciers and ice caps, but for frequencies in the megahertz to gigahertz range - glacial ice and snow become practically transparent. The wavelengths typically used for ice sounding are centimeters to meters in the ice. The equations governing the propagation of any electromagnetic waves are the Maxwell equations, here written as (Griffiths, 2013),

$$\begin{aligned} \nabla \cdot \mathbf{D} &= \rho_f & \nabla \times \mathbf{E} &= -\frac{\partial \mathbf{B}}{\partial t} \\ \nabla \cdot \mathbf{B} &= 0 & \nabla \times \mathbf{H} &= \mathbf{J}_f + \frac{\partial \mathbf{D}}{\partial t} \end{aligned} \quad \text{, where } \begin{cases} \mathbf{D} \equiv \varepsilon_0 \mathbf{E} + \mathbf{P}_m \\ \mathbf{H} \equiv \frac{1}{\mu_0}\mathbf{B} + \mathbf{M} \end{cases} \tag{2.1}$$

where $\mathbf{E}$ is the electric field, $\mathbf{P}_m$ is the material polarization, $\mathbf{B}$ is the magnetic field, $\mathbf{M}$ is magnetization, $\mathbf{J}_f$ is free current density, ρ_f is the free charge density, μ_0 and ε_0 is the permeability and permittivity of free space, respectively. $\mathbf{D}$ is known as the electric displacement. Worth noting is that $\mathbf{P}_m$ is the polarization of the medium, defined as dipole moment per unit volume, and has units C/m^2, which is not the same as the unitless vector defining the polarization of a wave.

Ice is a dielectric material (insulator), meaning that there are no free charges, expressed as $\mathbf{J}_f = \mathbf{0}$ and $\rho_f = 0$. In a dielectric, any charge is associated with an atom or molecule, and applying an electric field causes these charges to displace (Griffiths, 2013). On top of not having any free charges ice is also a linear dielectric, meaning that the polarization, $\mathbf{P}_m$ is proportional to the electric field, $\mathbf{P}_m = \varepsilon_0 \boldsymbol{\chi} \mathbf{E}$, where ε_0 is the permittivity of free space and $\boldsymbol{\chi}$ is the electric susceptibility. For isotropic materials, $\boldsymbol{\chi}$ is just a scalar, but for anisotropic materials like ice, it is represented as a second-order tensor. In general, the susceptibility depends on position when the material is non-homogeneous, which is generally the case for polycrystalline ice. From this we see that the electric displacement reduces to $\mathbf{D} = \varepsilon_0 \boldsymbol{\varepsilon} \mathbf{E}$ where $\boldsymbol{\varepsilon} = (\mathbf{I} + \boldsymbol{\chi})$ and $\mathbf{I}$ is the identity matrix. $\boldsymbol{\varepsilon}$ is called the relative permittivity tensor, but from here and onward, the permittivity is assumed to mean the relative permittivity unless stated otherwise. It also holds for a linear media that $\mathbf{H} = \frac{1}{\mu_0 \mu}\mathbf{B}$[1], where μ is relative permeability, which for ice is taken to be $\mu = 1$. All this put together, gives Maxwell's equations for ice,

Maxwell's equations for ice

$$\begin{aligned} &(1)\ \nabla \cdot \mathbf{D} = 0 & &(3)\ \nabla \times \mathbf{E} = -\frac{\partial \mathbf{B}}{\partial t} \\ &(2)\ \nabla \cdot \mathbf{B} = 0 & &(4)\ \nabla \times \mathbf{B} = \mu_0 \varepsilon_0 \boldsymbol{\varepsilon} \frac{\partial \mathbf{E}}{\partial t}. \end{aligned} \tag{2.2}$$

[1]Here it is assumed that the permeability of ice is isotropic, which is justified by the susceptibility being so small that even if it is not isotropic the effect is negligible

One interesting result of ice being anisotropic is that the polarization $\mathbf{P}_m$ does not necessarily point in the same direction as the applied electric field. Maxwell's equations, as presented in equations 2.2, are true for almost all linear dielectric materials, not just ice.

While it is true that electromagnetic waves in ice obey the first-order coupled differential equations displayed in 2.2, it is not obvious in their current form what they have to do with waves. Normally, when we think of waves, we think of a field, $\mathbf{u}$, obeying a second-order differential equation of the form,

$$\nabla^2\mathbf{u} = \frac{1}{c^2}\frac{\partial^2\mathbf{u}}{\partial t^2}, \tag{2.3}$$

where c is the propagation speed of the wave, determined from material constants. We can arrive at the wave equation for the electric field by applying the curl to equations 2.2.3 and inserting equation 2.2.4,

$$\nabla\times(\nabla\times\mathbf{E}) = -\nabla\times\frac{\partial\mathbf{B}}{\partial t} = -\frac{\partial}{\partial t}(\nabla\times\mathbf{B}) \Rightarrow$$
$$\nabla(\nabla\cdot\mathbf{E}) - \nabla^2\mathbf{E} = -\mu_0\varepsilon_0\boldsymbol{\varepsilon}\frac{\partial^2\mathbf{E}}{\partial t^2}.$$

For an isotropic material the permittivity is a scalar, $\boldsymbol{\varepsilon} \to \varepsilon$ and the electric displacement is proportional to the electric field, and hence $\nabla\cdot\mathbf{D} = \varepsilon\nabla\cdot\mathbf{E} = 0$, and the familiar wave equation pops out,

$$\text{isotropic wave equation: } \nabla^2\mathbf{E} = \mu_0\varepsilon_0\varepsilon\frac{\partial^2\mathbf{E}}{\partial t^2}, \tag{2.4}$$

and the propagation speed can be shown to be $c = (\mu_0\varepsilon_0\varepsilon)^{-1/2}$, where the speed of light in vacuum is $c_0 = (\mu_0\varepsilon_0)^{-1/2}$. For anisotropic materials, the electric displacement is not generally proportional to the electric field, and hence $\nabla\cdot\mathbf{E} \neq 0$, resulting in the anisotropic wave equation,

$$\boxed{\nabla^2\mathbf{E} - \nabla(\nabla\cdot\mathbf{E}) = \mu_0\varepsilon_0\boldsymbol{\varepsilon}\frac{\partial^2\mathbf{E}}{\partial t^2}.} \tag{2.5}$$

It is not immediately obvious what the propagation speed is for the anisotropic case, except that it is not the same in all directions as for the isotropic case. One way to get a better insight into equation 2.5 is to inset a plane wave solution and solve for the wave vector $\mathbf{k}$,

$$\mathbf{E} = |\mathbf{E}_0|\mathbf{P}\exp\left(j(\mathbf{k}\cdot\mathbf{r} - \omega t)\right), \tag{2.6}$$

where $\mathbf{r} = (x, y, z)^T$ is the position in space, $\mathbf{E}_0$ is the electric field at time $t = 0$ and position $\mathbf{r} = (0, 0, 0)^T$, $\mathbf{P}$ is the wave polarization and ω is the angular frequency of the plane wave. The wave vector is a three-dimensional vector, $\mathbf{k} = (k_x, k_y, k_z)^T$, and the phase speed/propagation speed of a plane wave along the i^{th} direction is $c_i = \frac{\omega}{k_i}$.

Equation 2.5 is fairly general for wave propagation in anisotropic linear dielectrics, but what about wave propagation in ice?

Wave propagation in a single ice crystal

Ice is a hexagonal crystal with uniaxial symmetry. General for materials like this is that they are optically anisotropic, or more specifically, uniaxial birefringent (Hecht, 2017). The symmetry axis is called the optical axis, and it turns out to be the same as the c-axis defined earlier on page 13. The permittivity of ice consists of two numbers corresponding to light polarized parallel to the optical axis, $\varepsilon_{\parallel}$, and perpendicular to the optical axis, $\varepsilon_{\perp}$. In tensor form, the permittivity of a single ice crystal can be written as (Fujita et al., 2000),

$$\boldsymbol{\varepsilon}_c = \begin{pmatrix} \varepsilon_{\perp} & 0 & 0 \\ 0 & \varepsilon_{\perp} & 0 \\ 0 & 0 & \varepsilon_{\parallel} \end{pmatrix} \quad \text{for: } \vec{\mathbf{c}} \parallel \mathbf{z} \tag{2.7}$$

for the z-axis parallel to the optical axis. The permittivities depend on the frequency of light and temperature but for radio frequencies at -15°C the real part of the permittivity[2] is here taken to be $\varepsilon_{\perp} = 3.15$ (T. Matsuoka et al., 1996) with an anisotropy of $\Delta\varepsilon \equiv \varepsilon_{\parallel} - \varepsilon_{\perp} = 0.034$ (T. Matsuoka et al., 1997). The permittivities depend slightly on the frequency and temperature, but the difference $\Delta\varepsilon$ does not significantly depend on the frequency, and only very weakly on temperature (T. Matsuoka et al., 1997).

Inserting the plane wave solution into equation 2.5 with $\boldsymbol{\varepsilon} = \boldsymbol{\varepsilon}_c$, yield the following equation,

$$\begin{pmatrix} -(k_y^2 + k_z^2)E_x + k_y k_x E_y + k_z k_x E_z \\ -(k_x^2 + k_z^2)E_y + k_z k_y E_z + k_y k_x E_x \\ -(k_x^2 + k_y^2)E_z + k_z k_x E_x + k_z k_y E_y \end{pmatrix} = -\mu_0 \varepsilon_0 \omega^2 \begin{pmatrix} \varepsilon_{\perp} E_x \\ \varepsilon_{\perp} E_y \\ \varepsilon_{\parallel} E_z \end{pmatrix} \tag{2.8}$$

which is a homogeneous system of linear equations and can be written as a matrix equation,

$$\begin{pmatrix} -(k_y^2+k_z^2)+\frac{\omega^2}{c_0^2}\varepsilon_{\perp} & k_y k_x & k_z k_x \\ k_y k_x & -(k_x^2+k_z^2)+\frac{\omega^2}{c_0^2}\varepsilon_{\perp} & k_z k_y \\ k_z k_x & k_z k_y & -(k_x^2+k_y^2)+\frac{\omega^2}{c_0^2}\varepsilon_{\parallel} \end{pmatrix} \begin{pmatrix} E_x \\ E_y \\ E_z \end{pmatrix} = \begin{pmatrix} 0 \\ 0 \\ 0 \end{pmatrix} \tag{2.9}$$

where $c_0^2 = (\mu_0 \varepsilon_0)^{-1}$. Non-trivial solutions, $\mathbf{E} \neq (0,0,0)^T$, can be found by setting the

[2]Relative permittivity. Unless stated, the permittivity always refers to the relative permittivity.

determinant of the matrix on the left-hand side equal to zero,

$$\begin{vmatrix} -(k_y^2+k_z^2)+\frac{\omega^2}{c_0^2}\varepsilon_\perp & k_yk_x & k_zk_x \\ k_yk_x & -(k_x^2+k_z^2)+\frac{\omega^2}{c_0^2}\varepsilon_\perp & k_zk_y \\ k_zk_x & k_zk_y & -(k_x^2+k_y^2)+\frac{\omega^2}{c_0^2}\varepsilon_\parallel \end{vmatrix} = 0 \tag{2.10}$$

From this, the non-trivial solutions have to satisfy the following equation (see appendix A for more details),

$$\underbrace{\left(\frac{k_x^2}{\varepsilon_\perp}+\frac{k_y^2}{\varepsilon_\perp}+\frac{k_z^2}{\varepsilon_\perp}-\frac{\omega^2}{c_0^2}\right)}_{\text{ordinary wave}}\underbrace{\left(\frac{k_x^2}{\varepsilon_\parallel}+\frac{k_y^2}{\varepsilon_\parallel}+\frac{k_z^2}{\varepsilon_\perp}-\frac{\omega^2}{c_0^2}\right)}_{\text{extraordinary wave}}=0. \tag{2.11}$$

There are two solutions to $\mathbf{k}$ that satisfy equation 2.9 and are commonly known in optics as the *ordinary* and *extraordinary* waves.[3]. What characterizes the ordinary wave is that no matter the direction of $\mathbf{k}$ the permittivity is the same, and the propagation speed of the wave is therefore always $c_0/\sqrt{\varepsilon_\perp}$. In other words, the ordinary wave effectively sees an isotropic medium. The extraordinary wave is different because the propagation speed is $c_0/\sqrt{\varepsilon_\parallel}$ in the xy plane, and $c_0/\sqrt{\varepsilon_\perp}$ along z.

Polarization inside an ice crystal

What happens to the polarization of the electric field inside the ice crystal? It is here illustrated with two examples.

1. For the simple case where $\mathbf{k} = (k_x, 0, 0)^T$ both the ordinary wave (O-wave), $k_x = \frac{\omega}{c_0}\sqrt{\varepsilon_\perp}$, and extraordinary wave (E-wave), $k_x = \frac{\omega}{c_0}\sqrt{\varepsilon_\parallel}$, gets excited and propagate at different speeds, but what about the polarization of the two waves? Returning to equation 2.9 and inserting the two solutions for k_x and solving for $\mathbf{P}$ yield the following (see appendix A for derivation),

$$\text{O-wave: } \mathbf{P} = \begin{pmatrix}0\\1\\0\end{pmatrix} \quad \text{for } \mathbf{k} = \frac{\omega}{c_0}\begin{pmatrix}\sqrt{\varepsilon_\perp}\\0\\0\end{pmatrix} \tag{2.12}$$

$$\text{E-wave: } \mathbf{P} = \begin{pmatrix}0\\0\\1\end{pmatrix} \quad \text{for } \mathbf{k} = \frac{\omega}{c_0}\begin{pmatrix}\sqrt{\varepsilon_\parallel}\\0\\0\end{pmatrix} \tag{2.13}$$

[3]The terms came from Erasmus Bartholinus, a professor of mathematics from the University of Copenhagen, in his publication from 1669 where he studied the birefringence of calcite (Garboe, 1954). When looking through calcite at a dot on an otherwise blank surface, the dot will appear twice with a small separation. When rotating the piece of calcite, one of the dots stays fixed, and the other dot circles around the first. Bartholinus called the ray from the stationary dot the ordinary refracted ray, and the one circling around it he called the extraordinary refracted ray (Garboe, 1954). He called the phenomenon double refraction.

The electric field of the ordinary wave is polarized along y, orthogonal to the optical axis, and the extraordinary wave is polarized along z, parallel to the optical axis.

2. In a bit more general case, consider a wave traveling at an angle α to the optical axis, $\mathbf{k} = k_0(\sin\alpha, 0, \cos\alpha)^T$. In this case both the ordinary and extraordinary waves are excited,

$$\text{O-wave: } \mathbf{P} = \begin{pmatrix} 0 \\ 1 \\ 0 \end{pmatrix} \quad \text{for } \mathbf{k} = \frac{\omega}{c_0}\sqrt{\varepsilon_\perp}\begin{pmatrix} \sin\alpha \\ 0 \\ \cos\alpha \end{pmatrix} \tag{2.14}$$

$$\text{E-wave: } \mathbf{P} = \begin{pmatrix} -\frac{\varepsilon_\parallel \cos\alpha}{\varepsilon_{\text{eff}}} \\ 0 \\ \frac{\varepsilon_\perp \sin\alpha}{\varepsilon_{\text{eff}}} \end{pmatrix} \text{ for } \mathbf{k} = \frac{\omega/c_0\sqrt{\varepsilon_\perp \varepsilon_\parallel}}{\sqrt{\varepsilon_\perp \sin^2\alpha + \varepsilon_\parallel \cos^2\alpha}}\begin{pmatrix} \sin\alpha \\ 0 \\ \cos\alpha \end{pmatrix} \tag{2.15}$$

where $\varepsilon_{\text{eff}} = \sqrt{\varepsilon_\perp \sin^2\alpha + \varepsilon_\parallel \cos^2\alpha}$, and assuming that $\alpha \neq 0$ which would correspond to propagation along the optical axis, and no extraordinary wave is excited. The full derivation can be found in appendix A. For $\alpha = \pi/2$, the result for propagation along x is recovered. The more general case demonstrates that the ordinary wave, no matter the orientation of $\mathbf{k}$, is always polarized perpendicular to the optical axis and propagates at a speed independent of α, which is not true for the extraordinary wave. Also, the ordinary and extraordinary electric fields are always orthogonal.

Index of refraction

The index of refraction for a material is the ratio of the speed of light in a vacuum and the speed of light in the medium. For ice, there are two: one for the ordinary wave and a second for the extraordinary wave. The index of refraction can be related to the wave vector as $n = |\mathbf{k}|c_0/\omega$, and the two indices of refraction can then be derived from equations 2.14 and 2.15,

$$n_o = \sqrt{\varepsilon_\perp}, \quad n_e = \frac{n_o}{\sqrt{1 + \left(\frac{n_o^2}{\sqrt{\varepsilon_\parallel}} - 1\right)\sin^2\alpha}} \tag{2.16}$$

where n_o is the index of refraction of the ordinary wave and n_e is the index of refraction of the extraordinary wave, here rewritten in terms of n_o and $\varepsilon_\parallel$. n_e and the polarization of the electric field depend on α. This means that the polarization and the difference between n_o and n_e (the birefringence) depend on the c-axis orientation relative to an incident wave. This result is the foundation for measuring the crystal orientations of thin slices of ice by using interference coloration (Owen & Hendrikse, 2023). The practical nature of measuring the crystal orientations is quite complicated, but it stems from the fact that the index of refraction of the extraordinary wave depends on the misalignment of the c-axis and the incident wave vectors.

Wave propagation in a polycrystalline ice

Ice sheets and glaciers consist of millions of individual ice crystals, and as discussed above, the propagation speed in ice depends on the orientation of the crystals. For radio-echo sounding, the wavelengths of light used are usually tens of centimeters, and the diameter of individual ice crystals is usually in the millimeter range (Thorsteinsson et al., 1997; Svensson et al., 2009). Therefore, the wavefront of a wave traveling through the ice will feel the effect of hundreds of individual crystals during a single oscillation. While the individual crystals are birefringent, in the case of polycrystalline ice with an isotropic COF (see figure 1.4a), the ice would appear isotropic to radio waves. On the other hand, if the ice has a preferred orientation, it would show some form of birefringence. Or at least that is the basic assumption. Hargreaves (1978) derived a relation between the permittivity of individual ice crystals and the bulk permittivity of polycrystalline ice,

$$\boldsymbol{\varepsilon}_b = \sum_i f_i \boldsymbol{\varepsilon}_c^{(i)} \tag{2.17}$$

where f_i and $\boldsymbol{\varepsilon}_c^{(i)}$ are the volume fraction and permittivity tensor of the i^{th} crystal inside a given volume of ice, respectively. While equation 2.17 seem somewhat intuitive, the bulk permittivity is a weighted sum of individual crystal permittivity, it is not a trivial or general result. From this equation, it is clear that if all crystals are evenly sized and randomly oriented, then the three diagonal components $\boldsymbol{\varepsilon}_b$ are equal, and the ice is isotropic. Equation 2.17 can also be written in an integral form using a density function, $\rho(\theta, \phi)$, similarly to equation 1.3. The bulk permittivity tensor then becomes (Hargreaves, 1978),

$$\boldsymbol{\varepsilon}_b = \int_{\phi=0}^{2\pi} \int_{\theta=0}^{\pi} \boldsymbol{\varepsilon}_c(\theta, \phi) \rho(\theta, \phi) \sin\theta d\theta d\phi \tag{2.18}$$

where $\boldsymbol{\varepsilon}_c(\theta, \phi) = \mathbf{R}_z(\phi)^T \mathbf{R}_y(\theta)^T \boldsymbol{\varepsilon}_c \mathbf{R}_y(\theta) \mathbf{R}_z(\phi)$ is the single crystal permittivity rotated into an arbitrary orientation on a unit sphere (θ, ϕ), and $\mathbf{R}_z(\phi)$ and $\mathbf{R}_y(\theta)$ are the rotation matrices for rotations about the z and y axis by ϕ and θ, respectively. For isotropic ice the density distribution is uniform, $\rho(\theta, \phi) = \rho_0 = \frac{1}{4\pi}$, and it can be shown that,

$$\text{Isotropic COF:} \quad \boldsymbol{\varepsilon}_b = \frac{1}{3}(2\varepsilon_\perp + \varepsilon_\parallel)\mathbf{I}, \tag{2.19}$$

where $\mathbf{I}$ is the (3x3) identity matrix. Rathmann et al. (2022) showed how equation 2.18 can be written in terms of the second-order structure tensor,

$$\boldsymbol{\varepsilon}_b = \frac{1}{3}(2\varepsilon_\perp + \varepsilon_\parallel)\mathbf{I} + \Delta\varepsilon \left(\langle \mathbf{c} \otimes \mathbf{c} \rangle - \frac{1}{3}\mathbf{I} \right). \tag{2.20}$$

which then can be written in terms of its eigenvalues,

$$\boldsymbol{\varepsilon}_b = \begin{pmatrix} \varepsilon_\perp + \Delta\varepsilon\lambda_x & 0 & 0 \\ 0 & \varepsilon_\perp + \Delta\varepsilon\lambda_y & 0 \\ 0 & 0 & \varepsilon_\perp + \Delta\varepsilon\lambda_z \end{pmatrix}, \tag{2.21}$$

which is a parametrization of the permittivity, which was first suggested by Fujita et al. (2006). Using $\boldsymbol{\varepsilon}_b$ in equation 2.9 and solving equation 2.10 does not yield a nice result that can be factorized into an ordinary and extraordinary wave as for the single crystal. This is because polycrystalline ice is not uniaxial like single ice crystals but instead biaxial. However, if one of the components of $\mathbf{k}$ is set to zero, it can be factorized into two distinct waves,

$$\underbrace{\left(\frac{k_x^2}{\varepsilon_y} + \frac{k_z^2}{\varepsilon_y} - \frac{\omega^2}{c_0^2}\right)}_{\text{ordinary wave}} \underbrace{\left(\frac{k_z^2}{\varepsilon_x} + \frac{k_x^2}{\varepsilon_z} - \frac{\omega^2}{c_0^2}\right)}_{\text{extraordinary wave}} = 0 \quad \text{for: } \mathbf{k} = (k_x, 0, k_z)^T, \tag{2.22}$$

where $\varepsilon_i = \varepsilon_\perp + \Delta\varepsilon\lambda_i$. Expressing the wave vector as for the single ice crystal case, $\mathbf{k} = k_0(\sin\alpha, 0, \cos\alpha)^T$, will yield a very similar result, just where $\varepsilon_\perp$ is replaced with ε_y for the ordinary wave, and for the extraordinary wave $\varepsilon_\perp$ is replaced by ε_x and $\varepsilon_\parallel$ is replaced by ε_z.

Polarization and permittivity for ice sounding

In ice sounding, the wave propagation is usually perpendicular to the surface, which will most likely be along the vertical direction, $\mathbf{k}_z = (0, 0, k_z)^T$. This, combined with the fact that common COFs, as seen in figure 1.4, usually have an eigenvector that is very close to being vertical, reduces the problem such that any bulk permittivity tensor can be written as,

$$\boldsymbol{\varepsilon}_b(\phi) = \begin{pmatrix} \varepsilon_\perp + \Delta\varepsilon\lambda_x - \Delta\varepsilon\Delta\lambda\sin^2\phi & \Delta\varepsilon\Delta\lambda\cos\phi\sin\phi & 0 \\ \Delta\varepsilon\Delta\lambda\cos\phi\sin\phi & \varepsilon_\perp + \Delta\varepsilon\lambda_y + \Delta\varepsilon\Delta\lambda\sin^2\phi & 0 \\ 0 & 0 & \varepsilon_\perp + \Delta\varepsilon\lambda_z \end{pmatrix}, \tag{2.23}$$

where $\boldsymbol{\varepsilon}_b(\phi) = \mathbf{R}_z(\phi)^T \boldsymbol{\varepsilon}_b \mathbf{R}_z(\phi)$ and $\Delta\lambda = \lambda_x - \lambda_y$. For propagation along the z-axis will reduce equation 2.22 to,

$$\left(\frac{k_z^2}{\varepsilon_y} - \frac{\omega^2}{c_0^2}\right)\left(\frac{k_z^2}{\varepsilon_x} - \frac{\omega^2}{c_0^2}\right) = 0 \quad \text{for: } \mathbf{k} = (0, 0, k_z)^T, \tag{2.24}$$

where it no longer makes sense to characterize the waves as ordinary and extraordinary. The polarization for the two solutions is as follows,

$$\mathbf{P} = \begin{pmatrix} \cos\phi \\ \sin\phi \\ 0 \end{pmatrix} \equiv \mathbf{P}_x \qquad \text{for: } \mathbf{k} = \frac{\omega}{c_0} \begin{pmatrix} 0 \\ 0 \\ \sqrt{\varepsilon_x} \end{pmatrix} \tag{2.25}$$

$$\mathbf{P} = \begin{pmatrix} -\sin\phi \\ \cos\phi \\ 0 \end{pmatrix} \equiv \mathbf{P}_y \quad \text{for: } \mathbf{k} = \frac{\omega}{c_0} \begin{pmatrix} 0 \\ 0 \\ \sqrt{\varepsilon_y} \end{pmatrix} \tag{2.26}$$

which, perhaps not surprisingly, corresponds to the two horizontal eigenvectors of $\boldsymbol{\varepsilon}_b(\phi)$. This means that only two orthogonally polarized waves can exist in horizontally anisotropic ice, $\varepsilon_x \neq \varepsilon_y$, and they propagate at phase speeds $c_0/\sqrt{\varepsilon_x}$ and $c_0/\sqrt{\varepsilon_y}$. This fact can be used to derive the anisotropy of ice using polarized radar, which will be discussed in much more detail later. The results of equations 2.25 and 2.26 are illustrated in figure 2.1.

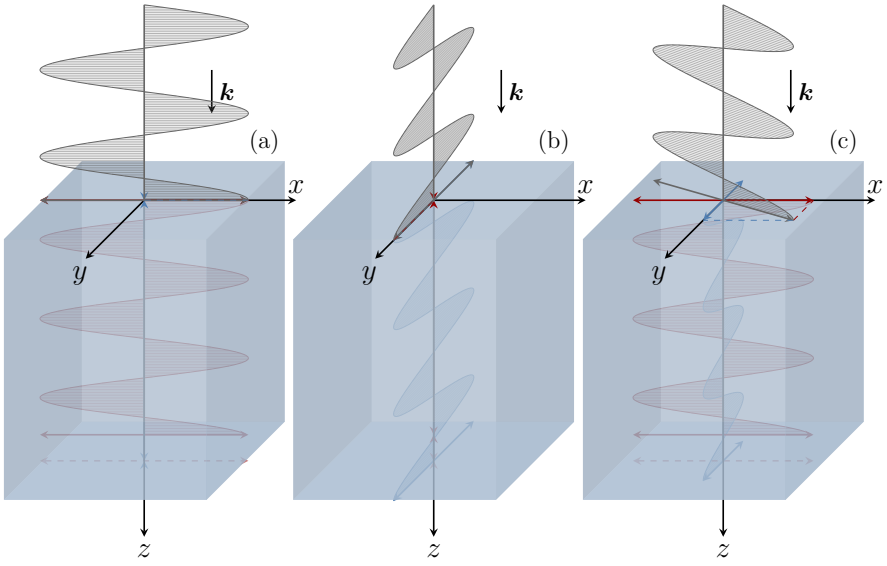

Figure 2.1: Polarizations in birefringent polycrystalline ice. The incoming wave, the black curve, is polarized according to the horizontal principal axes of the COF, x and y. (a) and (b) are incoming polarizations along x and y, respectively. In both cases, the wave keeps its polarization. In (c), the incoming wave is polarized at an angle and split into two waves polarized along x and y. The phase speed differs along the two principal axes, illustrated by different wavelengths and offsets in the ice.

Radar systems for ice sounding

A radar is a system capable of transmitting and recording electromagnetic radiation, usually in the microwave frequency (Skolnik, 2007). Within this broad definition, there exist countless different systems designed for specific applications, like a Doppler radar

for measuring the speed of an object or a rain radar detecting and quantifying the severity of rain. Within these many applications, different radar designs/principles are utilized to balance accuracy and signal-to-noise ratio with practical constraints such as cost, size, and energy consumption. Within the field of radioglaciology, two systems are commonly used, the mono-pulse and chirped-waveform systems (Schroeder et al., 2020). A mono-pulse system transmits a monochromatic wave for a short time interval, where the length of the time interval is called the pulse length. The pulse length determines how close two objects (layers in the ice) can be before their recorded echos overlap. A short pulse gives a good range resolution but a poor signal-to-noise ratio. This is because the signal-to-noise ratio of the output from the radar receiver depends on the total energy of the received signal (Skolnik, 2007). Increasing the power during transmission can compensate for the short pulse, which only works until a certain limit. That means that a mono-pulse system has to find a compromise between the range resolution and the needed signal-to-noise ratio to sound at a given depth. One solution to this problem is using a frequency-modulated or chirped pulse. In this case, the range resolution is inversely proportional to the bandwidth of the chirp and does not depend on the pulse length (Skolnik, 2007). If B is the bandwidth and c_{ice} is the speed of light in ice for radar waves, then the range resolution can be written as,

$$\Delta R = \frac{c_{ice}}{2B}. \tag{2.27}$$

This means that much longer pulses can be used without compromising the range resolution. The range resolution of the frequency-modulated radar systems is due to a process called *pulse compression*, where the received pulse is correlated with a copy of the transmitted signal. Pulse compression will be discussed in more detail in the next chapter. The frequency-modulated continuous wave radar (FMCW) is a different type of chirped-waveform radar system. It does not transmit pulses but a continuous wave that modulates its frequency throughout transmission. FMCW systems have the same theoretical range resolution as a chirped pulse with the same bandwidth, but due to the long transmit time, they can use very low power and achieve a good signal-to-noise ratio. The low power also enables simultaneous transmission and receiving, which is often not possible for pulse-based systems because the high transmit power could destroy the receiver.

The mono-pulse systems are arguably the simplest radar design and have been used for many ice-sounding applications, such as ice thickness (Gudmandsen, 1969; Karlsson et al., 2024), internal layers (Gudmandsen, 1975; Fujita et al., 1999), birefringence and anisotropy (Hargreaves, 1977; Fujita & Mae, 1994; Fujita et al., 2006). However, most modern radar systems for ice sounding utilize frequency modulation in combination with the ability to detect the phase of the return signal (Gogineni et al., 2001; Rodriguez-Morales et al., 2014; Brennan et al., 2014; Yan et al., 2020). In connection with computers becoming more powerful and digital storage becoming much faster and

at a much greater capacity, it has become possible to record an almost raw signal of amplitude and phase which is stored as a complex number. These systems allow for processing steps that were previously done analog before writing to disk, like pulse compression and downsampling, to be done digitally after recording. Of course, everything comes at a price, and these types of radar systems require powerful servers with an array of data drives to keep up with the massive amount of information being collected. Processing all this data can be a computationally demanding task.

Chapter 3

Data acquisition and processing

In this chapter, I will give an overview of the 2022 survey of NEGIS, which forms the basis of my work with radar-derived COF, and the radar system used. During the PhD, I also participated in a radar survey of Müller Ice Cap in arctic Canada in 2023 (Lilien et al., 2024). Common for both surveys is the radar system used, namely the ultra-wideband (UWB) quad-polarized radar system developed by the University of Alabama (Yan et al., 2020; L. Li et al., 2020). At NEGIS, we also deployed a second radar system, the UHF Mills-T radar, which the University of Alabama also developed. I have not included any data from or discussion of the UHF Mills-T radar.

UWB radar

The ultra-wideband quad-polarized radar system, referred to as the UWB radar, is a multichannel coherent ice sounder capable of transmitting and receiving at two mutually orthogonal polarizations. We called it quad-polarized because it can record four different configurations of transmit-receive polarizations, so strictly speaking, it is dual-polarized, but the ability to switch polarization between transmit and receive makes it relatively unique. It uses frequency-modulated pulses (chirps), and during both the NEGIS and Müller ice cap campaigns, the radar was working at a center frequency of 330 MHz and a bandwidth of 300 MHz. The high bandwidth gives it an extremely good range resolution, and using equation 2.27 with $c_{ice} = 1.69 \cdot 10^8$ m/s gives it a theoretical range resolution of around 30 cm, i.e., being able to distinguish between layers in the ice only separated by 30 cm. The pulse length can be configured digitally, and for NEGIS in 2022, it was set to alternate between 10 µs and 1 µs chirps, and at the Müller ice cap, we used 2 µs chirps. In both cases, the radar was set up to have a pulse-repetition frequency of 5 kHz. A figure of the UWB radar, as it was operated at NEGIS in 2022, can be found in figure 3.1. The radar consists of a digital-to-analog converter (DAC) that converts 8 digital channels to 8 analog signals that are then sent to the transmitter, where the signals are amplified. The transmitter splits the signals into 10 channels before entering the high-power switch, where the signals are either sent through the H or V ports to the

antenna panels. The return signal enters the antenna elements and is sent back to the high power switch where the signal from H or V is combined into 8 channels, sent to the receiver for amplification, and finally sent to the analog-to-digital convert (ADC). The switch is controlled by the digital system, and polarizations can be configured by the radar operator.

The antenna panels consist of 12x12 dual-polarized antenna elements capable of transmitting and receiving at along-track (V) and across-track (H) polarizations.

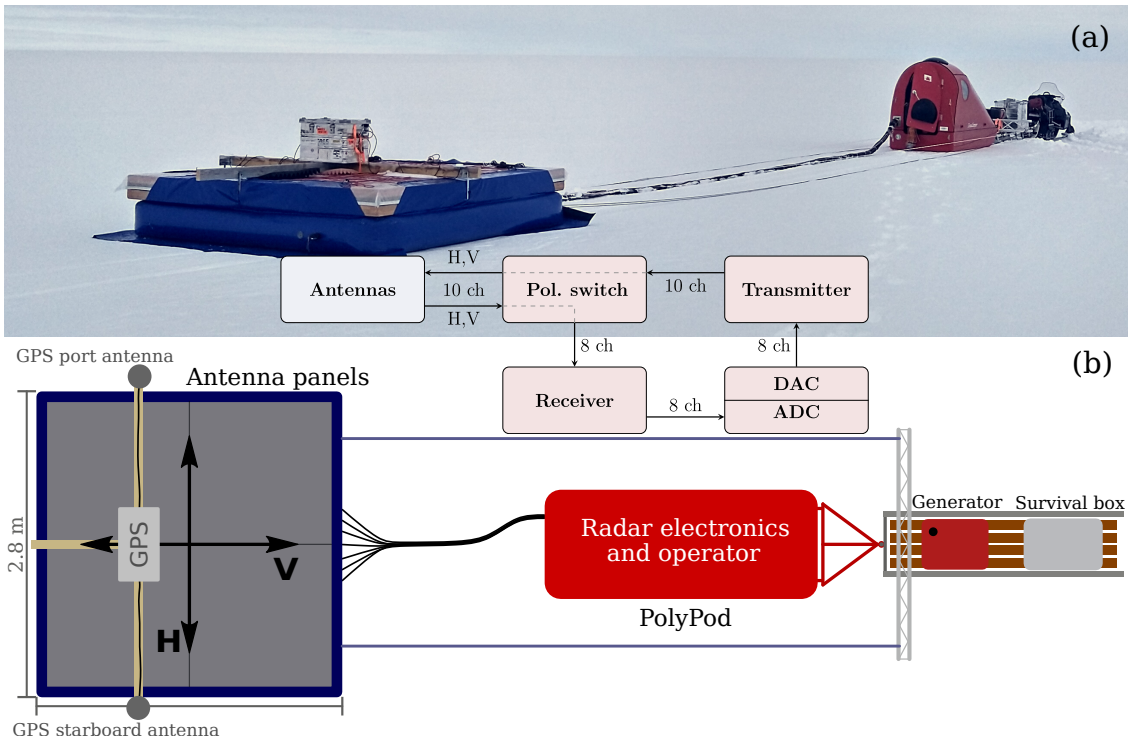

Figure 3.1: (a) Picture of the UWB radar as operated during the NEGIS field campaign in 2022. (b) A sketch of the setup, as seen from above, with the antenna panels towed behind the PolyPod with all the radar electronics (block diagram) and operator, and a small sled with a generator and survival box. On top of the antenna panels are mounted two GPS antennas used for precision orientation. H and V indicate the two polarization directions.

Data processing

Before the signal is written to disk, the system does 128 hardware integrations to boost the signal strength and reduce storage needs. The data is written to 8 solid state drives, one for each channel. After data collection, the raw files all run through the same processing. First, the raw data is coherently decimated, where neighboring traces are summed together, assuming coherence. The number of traces is variable and depends on the conditions. Next, the decimated data is frequency shifted to center the frequency spectrum around 0 Hz. For the UWB radar, the signal is shifted by a local oscillator from

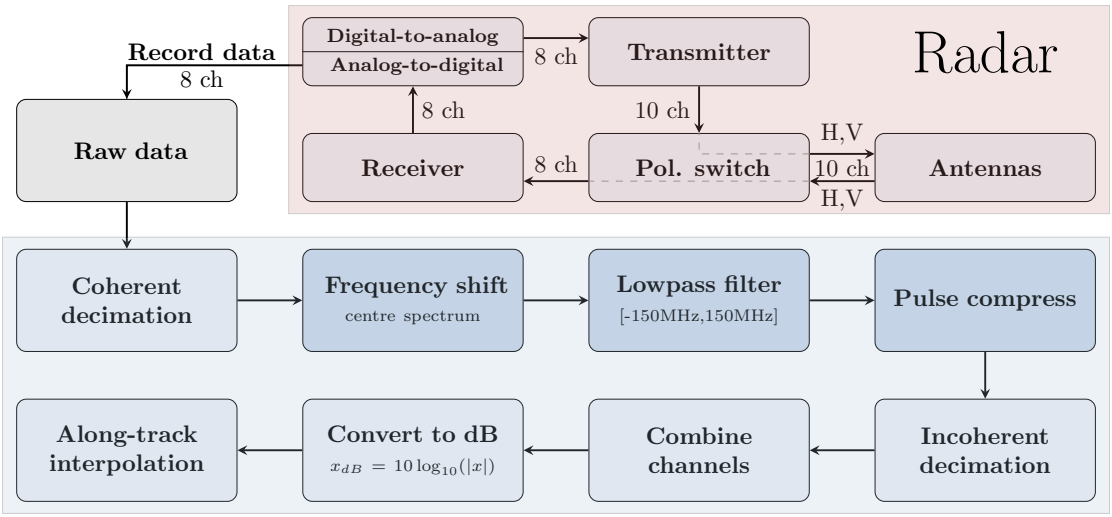

Figure 3.2: Processing diagram for the UWB radar. Text next to arrows in the red block refers to the number of signals, or channels, that are being passed on between the radar elements. Light blue blocks are optional/variable processing steps, and dark blue blocks are obligatory/fixed processing steps.

330MHz to 80MHz before being written to disk, and the frequency shift is then there to remove the 80MHz offset. Assuming that the recorded signal can be represented as a sum of complex exponentials of different frequencies and amplitudes, then a constant frequency shift of f_{shift} can be achieved by multiplying the signal with $\exp(j2\pi f_{shift}t)$,

$$\left(\sum_i A_i \exp\left(j2\pi f_i t\right)\right) \exp(j2\pi f_{shift}t) = \sum_i A_i \exp\left(j2\pi(f_i + f_{shift})t\right)$$

where A_i is the amplitude of the signal with frequency f_i, and t is time. Next, a lowpass filter is applied to dampen any signal outside the frequency range [-150 MHz,150 MHz]. This is followed by pulse compression, where a digitally generated chirp, identical to the one transmitted by the radar, is cross-correlated with the signal. A linear frequency-modulated chirp has an instantaneous frequency curve on the form,

$$f(t) = \frac{B}{T}t - \frac{B}{2} + f_c \quad \text{for: } t \in [0, T] \tag{3.1}$$

where T is the chirp length and f_c is the center frequency, or carrier frequency. After frequency shift $f_c = 0$. The phase of the chirp is proportional to the integral of the frequency curve, resulting in the following expression for the chirp,

$$s_{chirp}(t) = \exp\left(j2\pi\left(\frac{B}{2T}t^2 - \frac{B}{2}t + f_c t\right)\right) \quad \text{for: } t \in [0, T]. \tag{3.2}$$

Frequency shift, lowpass filtering, and pulse compression are the three processing steps that are always done in the same way across surveys. After pulse compression, the data is again decimated, but we do not assume coherence this time. Instead, we do a sub-

sample time shifting of neighboring traces to match a reference trace before integrating. Matching the traces is done by calculating the correlation between the target trace and the reference trace for each subsample time shift and picking the time shift corresponding to the highest correlation. Subsample time shifting is explained in appendix B. Until now, every processing step has been done individually for each channel, but to achieve an even better signal-to-noise ratio, the 8 channels are combined. They are combined through the exact same process as the incoherent decimation, where one of the channels is picked as the reference channel.

In reality, there is a step that is not included in the diagram in figure 3.2, as it is not always necessary, namely filtering out bad traces. During the field season in 2022 at NEGIS, we would sometimes experience quite a lot of interference, making some of the recorded traces unusable. These traces can be filtered out if necessary by removing any trace with a 99^{th} percentile amplitude above a certain threshold, which natural reflections cannot cause.

Channel combining is the last step in the standard processing line, and the last two steps included in figure 3.2, convert to decibel and along-track interpolation, are mostly for convenience when plotting the final echograms. Converting to dB can also be skipped and then, after along-track interpolation, can be followed by a migration algorithm, for example, wavenumber domain algorithms or range-Doppler algorithms (Bamler, 1992). We have not had much success implementing such algorithms that improve the overall data significantly, even though it should be possible if done carefully. For the data collected at the Müller Ice Cap, we implemented a simple range-Doppler algorithm that managed to focus the bed reflector and get a more accurate estimate of the ice thickness. This was necessary due to the highly varying basal topography of the ice cap.

NEGIS in 2022

In June and July of 2022, we did a radar survey of NEGIS with the UWB radar, with a focus on the anisotropic properties of the ice stream, and a smaller survey with the UHF radar focusing on imaging the large folds in the ice just outside the southeastern shear margins of NEGIS (Franke, Jansen, et al., 2022; Jansen et al., 2024). Figure 3.3 shows an overview of the radar lines we drove in 2022, approximately 500 km of UWB lines and 260 km of UHF lines.

Figures 3.4 and 3.5 show HH, HV, VV and VH echograms collected with the UWB radar along and across NEGIS, respectively. The vertical scale is two-way travel time (TWT) relative to the surface. From the data collected parallel to flow, it is evident from a visual inspection of the echograms that polarization matters, clearly showing some form of anisotropy. The VV data's return power is lower than the HH data, made more evident by the A-scope comparison (Figure 3.4e). Hargreaves (1977) show that the returned signal for a receive antenna perpendicular to the transmit antenna, cross-polarization, will have a 90-degree periodicity in the return amplitude with antenna

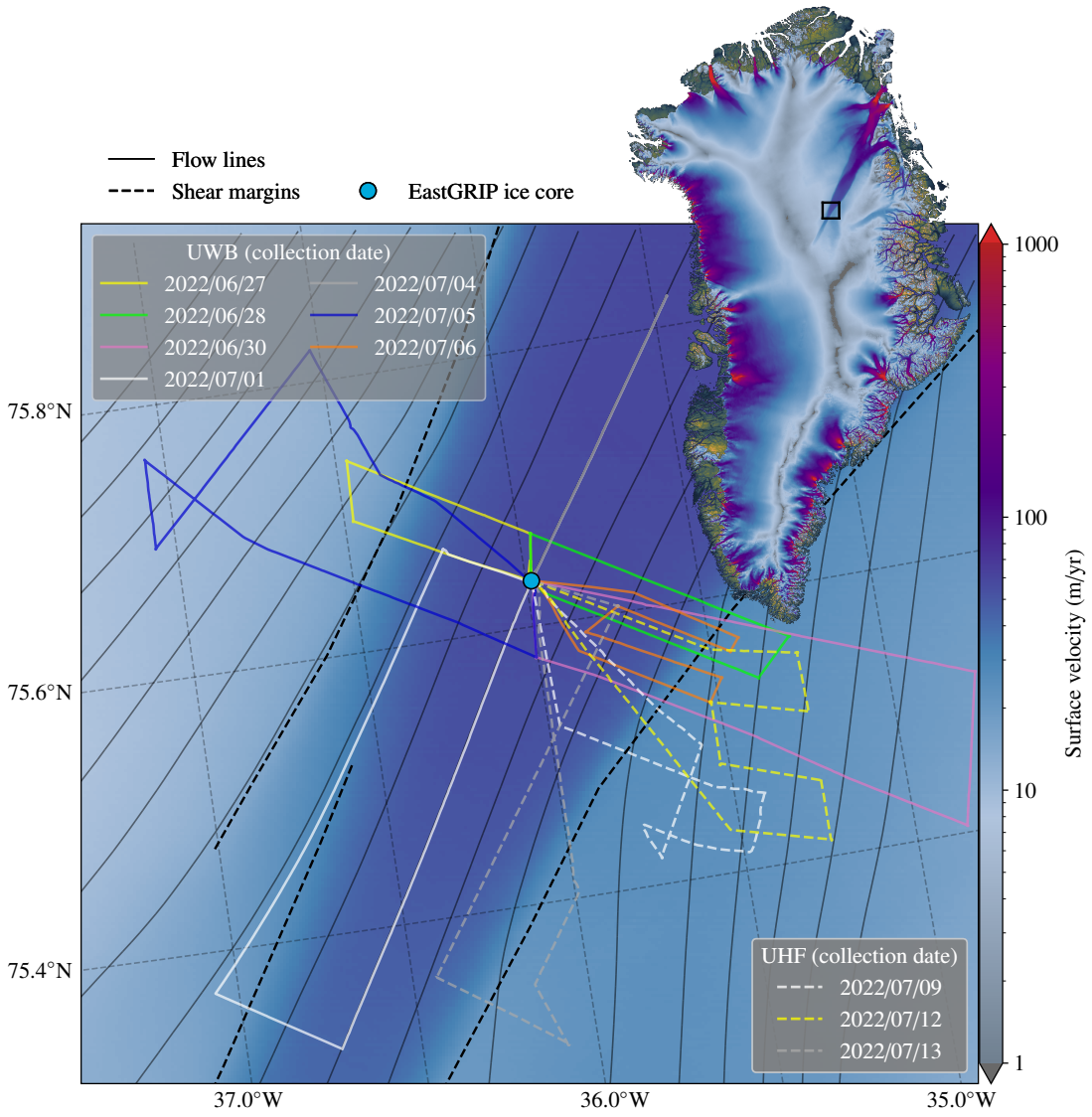

Figure 3.3: Overview of radar lines driven with the UWB and UHF radars at NEGIS in 2022 plotted on top of surface velocities. Colored Solid lines are UWB data, and colored dashed lines are UHF data. Flow lines are shown in solid dark gray lines, approximate locations of shear margins are shown in black dashed lines, and the location of EastGRIP is shown as a blue dot. The black square on the full Greenland map shows the outline of the borders of the main plot.

orientation in a birefringent medium. In other words, the return power in the HV and VH data is expected to be identical, as they are just 90-degree rotations of each other. This looks to hold true upon inspection of Figure 3.4(c,d). What is also worth noting for the HV and VH echograms in figure 3.4 is that the return power at greater depths is greatly reduced from around 35 km along-track distance and onwards. Following Hargreaves (1977) we would expect no return power for HV and VH in a birefringent medium when the polarizations are along the principal components of the COF, assuming constant

orientation of the principal components with depth. There are always small variations in the orientation as the COF develops from isotropic at the surface to an anisotropic COF with depth. This, combined with continuous variations in antenna orientation due to driving imperfections, will never yield a full power extinction, even if noise is absent. The fact that the bed can be easily detected in the cross-polarized echograms in figure 3.4(c,d) is evidence that the antenna polarizations are not completely aligned with the principal components. This could be due to the driving imperfections causing random perturbations in the antenna orientation during collection, the principal components are not constant with depth, the transmit polarization is not purely H or V (cross-polarization leakage). The cross-polarization leakage for the UWB antenna panels is -30 dB or better for most of the frequency spectrum (L. Li, 2021), suggesting it is a minor issue.

The echograms across NEGIS, Figure 3.5 look significantly different compared to along NEGIS. The slope of the layers changes a lot within a relatively short distance, and there are areas where the internal reflections almost disappear. These areas are the shear margins, and the loss of reflections is due to steeply sloping layers (Jansen et al., 2024) that reflect all the energy away from the nadir, causing almost echo-free zones. Because the radar is moving, the steep layers are potentially detected as off-nadir reflections. Through carefully constructed SAR processing or migration, it should be possible to partially recover the true locations of these reflections.

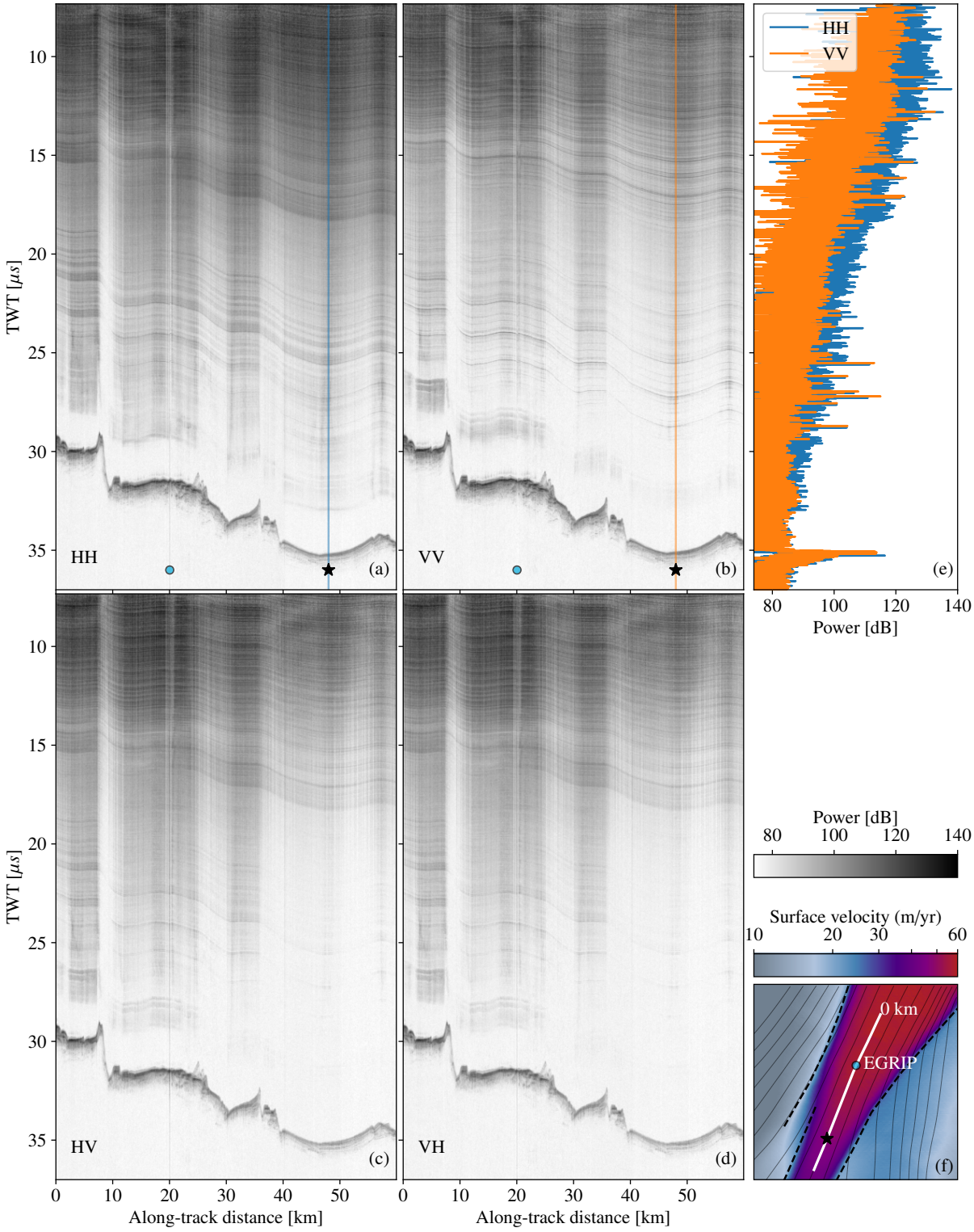

Figure 3.4: Two co-polarized echograms (a,b) and two cross-polarized echograms (c,d) collected along NEGIS with the UWB radar. EGRIP is located around 20 km along-track distance, marked by the blue dot on the HH and VV echograms (a,b) and velocity map (f). The echograms are compiled using lines 2022/07/01 and 2022/07/04 as seen in figure 3.3. (e) shows A-scopes of the HH and VV signals at locations indicated by the blue and orange vertical lines on (a,b) and a star on (f).

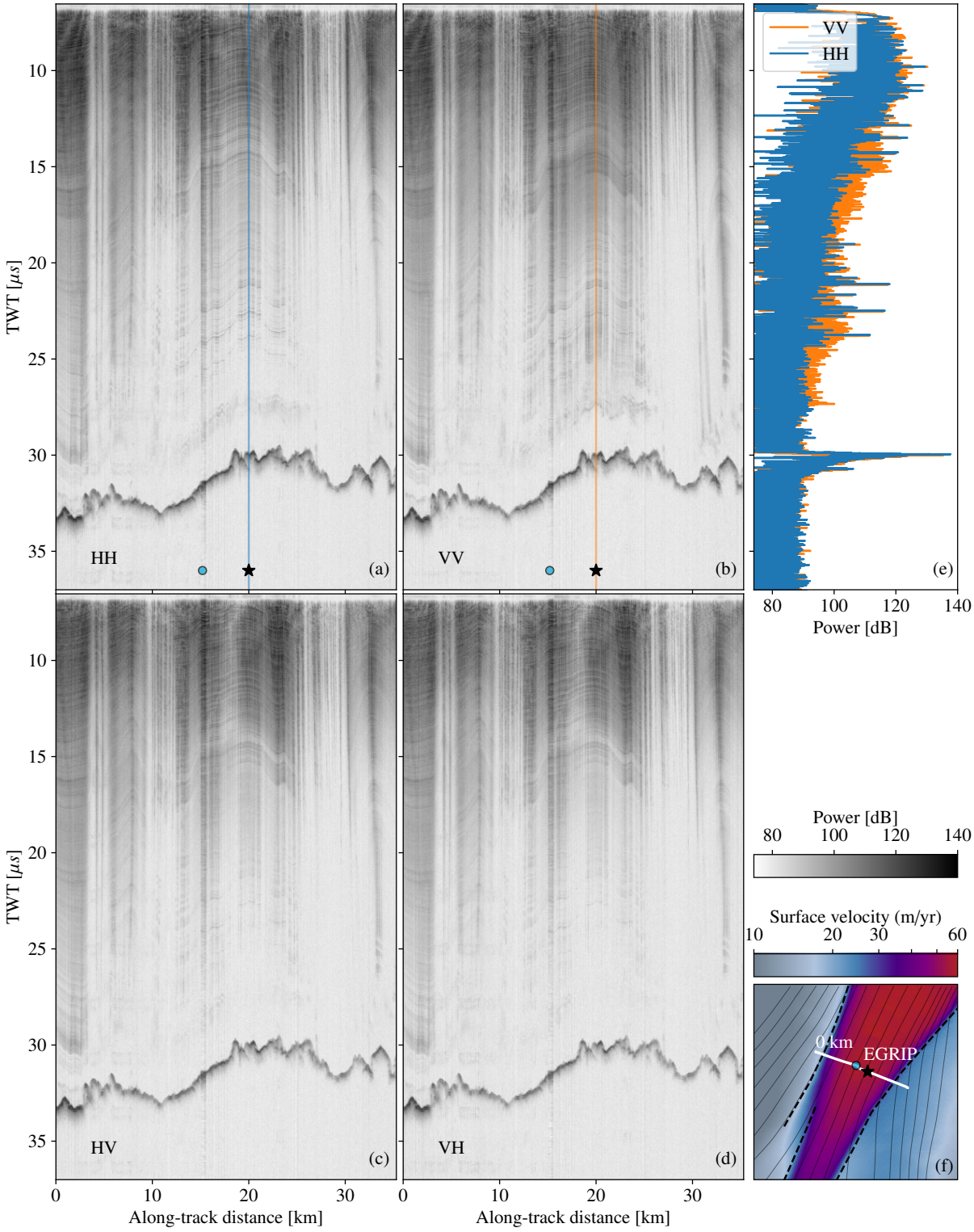

Figure 3.5: Two co-polarized echograms (a,b) and two cross-polarized echograms (c,d) collected across NEGIS with the UWB radar. EGRIP is located around 16 km along-track distance, marked by the blue dot on the HH and VV echograms (a,b) and velocity map (f). The echograms are compiled using lines 2022/06/27 and 2022/06/28 as seen in figure 3.3. (e) shows A-scopes of the HH and VV signals at locations indicated by the blue and orange vertical lines on (a,b), and a star on (f).

Chapter 4

Radar derived COF

In chapter 2, the polarization and propagation of radio waves in ice were derived for COFs with a vertical principal component. The two equations 2.25 and 2.26 derived for a bulk permittivity tensor with a vertical eigenvector and arbitrarily oriented horizontal eigenvectors. These two equations form the basis for deriving information about the crystal orientation fabrics in ice sheets and glaciers. Assuming horizontal anisotropy, $\varepsilon_x \neq \varepsilon_y$, then any transmitted radar wave will be polarized according to $\mathbf{P}_x$ and $\mathbf{P}_y$, and the propagation speed of these two waves will be determined by the bulk permittivities, ε_x and ε_y, which we write in terms of the horizontal eigenvalues of the second-order structure tensor, λ_x and λ_y. In figures 3.4 and 3.5, it is evident from visual inspection that the polarization of the radar matters for the return signal, but it is not obvious that the echograms also contain evidence of birefringence. The visual difference in the return power is more related to the anisotropic scattering of the ice, i.e., the reflection coefficient along the different polarization orientations is different. The most apparent evidence of birefringence comes when comparing the travel times of the reflectors in the HH and VV echograms.

Travel-time difference

In figure 4.1 are the approximate travel-time differences of the bed reflector in the along and across NEGIS profiles. The bed reflectors were picked using ImpDAR (Lilien et al., 2020). The travel-time difference, Δt, was calculated as the difference in two-way travel time between the HH and VV echogram. Positive values mean the travel time is greater in HH than in VV. Along the center flow-line of NEGIS (A-A′), the travel-time difference is positive and relatively constant with an average of $\approx$ 80 ns, and perhaps a slight increase upstream. Across NEGIS (B-B′), the travel-time difference is more variable but with an average of $\approx$ -50 ns. At both shear margins, the travel-time difference almost disappears, and at the southwestern margin (close to B′), it even turns positive. It should be noted that there is a high degree of uncertainty when tracing the basal reflector, especially when the tolerance is in the order of tens of nanoseconds. The

base of the ice sheet is an inconvenient reflector to compare travel times, as is evident from the broad and less defined peaks from the basal reflector compared to internal reflectors in the A-scopes of figure 3.4e and 3.5e. However, the basal reflector is almost always in the data. It is clear that there is a non-zero travel-time difference, and both the along and across profiles show that the travel times for polarizations parallel to the general flow tend to be shorter compared to polarizations perpendicular to flow. In other words, the propagation speed is greater for polarizations parallel to flow due to a lower permittivity. The relationship between the bulk permittivity and second-order structure tensor, see equation 2.21, provides a way to convert the travel-time difference to information about the horizontal eigenvalues of the second-order structure tensor, as will be explored in the following.

Horizontal eigenvalue difference

The two-way travel time of a wave can be expressed as the slowness, $\mathscr{S}$, integrated over the propagation path. For a nadir-sounding radar, it can be expressed as follows,

$$t(d) = 2\int_0^d \mathscr{S}(z)dz, \tag{4.1}$$

where the factor two comes from the fact it is a two-way travel time, and d is the depth of the reflector. For a birefringent medium like ice, the waves are polarized along the horizontal eigenvectors of the second-order structure tensor of the COF, which define the x and y-axis for the following. Their travel times can be expressed in terms of the eigenvalues as follows,

$$t_x(d) = 2\int_0^d \mathscr{S}_x(s)dz, \quad \mathscr{S}_x(z) = \frac{1}{c_0}\sqrt{\varepsilon_\perp + \Delta\varepsilon\lambda_x(z)} \tag{4.2}$$

$$t_y(d) = 2\int_0^d \mathscr{S}_y(s)dz, \quad \mathscr{S}_y(z) = \frac{1}{c_0}\sqrt{\varepsilon_\perp + \Delta\varepsilon\lambda_y(z)} \tag{4.3}$$

Because $\Delta\varepsilon\lambda_i \ll \varepsilon_\perp$ is always true, the first order Taylor expansions of $\mathscr{S}_x$ and $\mathscr{S}_y$ about $\Delta\varepsilon\lambda_i = 0$ are a very accurate approximations. The travel-time difference can then be related to the eigenvalue differences,

$$\begin{aligned}
\Delta t(d) = t_x(d) - t_y(d) &= \frac{2}{c_0}\int_0^d \left(\sqrt{\varepsilon_\perp + \Delta\varepsilon\lambda_x(z)} - \sqrt{\varepsilon_\perp + \Delta\varepsilon\lambda_y(z)}\right) dz \\
&\approx \frac{2}{c_0}\int_0^d \left(\sqrt{\varepsilon_\perp} + \frac{\Delta\varepsilon\lambda_x(z)}{2\sqrt{\varepsilon_\perp}} - \sqrt{\varepsilon_\perp} - \frac{\Delta\varepsilon\lambda_y(z)}{2\sqrt{\varepsilon_\perp}}\right) dz \\
&= \frac{\Delta\varepsilon}{c_0\sqrt{\varepsilon_\perp}}\int_0^d \Delta\lambda(z)dz = \frac{d\Delta\varepsilon}{c_0\sqrt{\varepsilon_\perp}}\overline{\Delta\lambda}(d)
\end{aligned} \tag{4.4}$$

where $\overline{\Delta\lambda}(d) \equiv \frac{1}{d}\int_0^d \Delta\lambda(z)$ is the mean eigenvalue difference at depth d. Rearranging

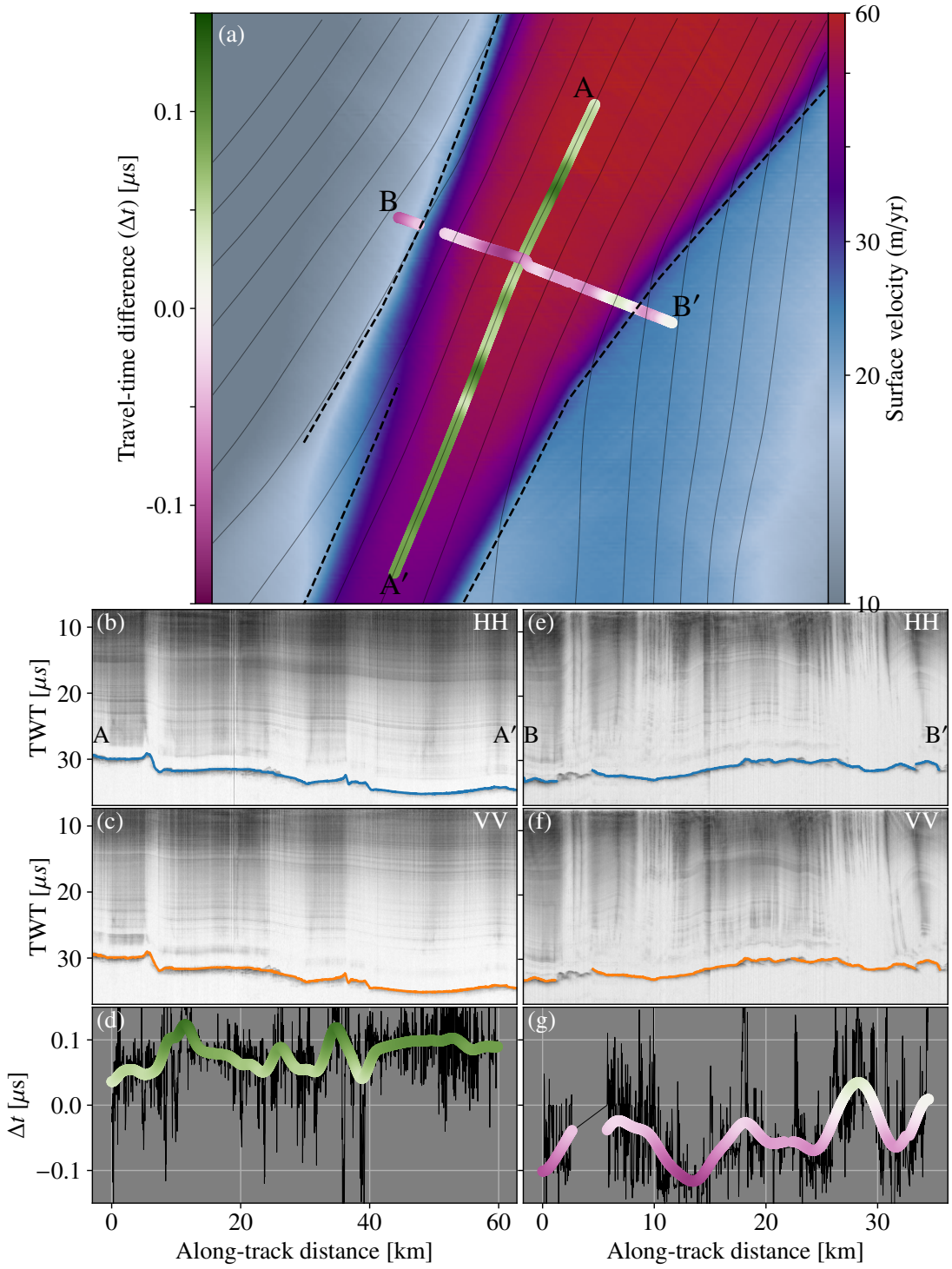

Figure 4.1: Travel-time difference derived from the bed reflectors of the HH and VV echograms collected along (b,c) and across (e,f) NEGIS. Blue and orange lines in (b-f) mark the location of the bed reflectors in the respective echograms. Thin black lines in (d) and (g) show the two-way travel-time difference between the bed reflectors in HH and VV, and the colored lines are the smoothed travel-time difference using a Gaussian filter with a standard deviation of 1km. Green and purple colors indicate the strength of travel-time difference and are plotted on top of a NEGIS velocity map (a).

this yields the mean eigenvalue difference as a function of the travel-time difference,

$$\boxed{\overline{\Delta\lambda}(d) = \frac{c_0\sqrt{\varepsilon_\perp}}{d\Delta\varepsilon}\Delta t(d)}. \tag{4.5}$$

The inclusion of the depth in equation 4.5 makes things slightly complicated because the depth will, in most cases, need to be determined by the travel time of the radar wave, which depends on the eigenvalue difference. However, for most cases, the difference in the depth estimate you get from assuming the most anisotropic case compared to isotropic is less than 0.5%. The sampling frequency of the UWB radar is 500MHz, which is a sampling interval of 2ns, and the travel time is on the order of tens of ns. It is, therefore, appropriate to assume isotropic ice for determining d, as the uncertainty of Δt will dominate the result.

Assuming isotropic propagation speed for determining d will yield the following result,

$$d = \frac{c_0}{2\sqrt{\overline{\varepsilon}}}(t_x + t_y)/2 \quad \text{for: } \overline{\varepsilon} = \tfrac{2}{3}\varepsilon_\perp + \tfrac{1}{3}\varepsilon_\parallel.$$
$$\overline{\Delta\lambda}(d) = \frac{4\sqrt{\varepsilon_\perp\overline{\varepsilon}}}{\Delta\varepsilon}\frac{\Delta t(d)}{t_x(d) + t_y(d)}$$

A slightly different approach can also be taken, where instead of approximating the slowness with a first-order Taylor expansion, the eigenvalue difference is assumed constant with depth, $\Delta\lambda(d) = \Delta\lambda$, in which case,

$$\Delta\lambda = \frac{\Delta t(d)}{t_x(d) + t_y(d)}\frac{4\overline{\varepsilon}}{\Delta\varepsilon}. \tag{4.6}$$

The two approaches are identical for any practical application, as the difference between $\varepsilon_\perp$ and $\overline{\varepsilon}$ is less than 0.3%.

Limits of travel-time difference

Travel-time differences provide a very direct way to estimate the eigenvalue difference of the COF, but there are a few limitations to the method described above. First, you need two orthogonal co-polarized signals. This can be achieved by having the capability to switch between polarizations as you go, like the UWB radar, finding points where survey tracks cross orthogonally (Gerber et al., 2023), or being able to rotate the antennas and repeat the measurement (Zeising et al., 2023). A second limitation is that the polarization of the two signals has to be sufficiently parallel to the principal axes of the COF. As illustrated in figure 2.1, a misalignment will cause a mix of the two allowed waves. For the case of 45-degree misalignment, the HH and VV signals will look close to identical, and no travel-time difference will be observed. From the travel-time difference in figure 4.1, it seems like there is no anisotropy at the shear margins, which is where

the greatest horizontal anisotropy is expected to be (Gerber et al., 2023). This can be interpreted as evidence that the radar is oriented sufficiently far from the principal axes of the COF, but how far? In the next chapter, I will present a new method for using the areas where the apparent anisotropy disappears, not only to get the horizontal eigenvalue difference but also to estimate the orientation of the horizontal eigenframe of the COF.

Phase-sensitive polarimetric radar

A set of radar types that are specifically suitable for studying the anisotropy of ice is phase-sensitive polarimetric radars, a category that the UWB radar falls under, as well as the popular ApRES systems (Brennan et al., 2014; Nicholls et al., 2015) originally developed for studying basal melt rates. Due to its ease of use and possibility to rotate the receive and transmit antennas independently, it has also been used in studying COF (Jordan et al., 2020; Ershadi et al., 2022; Zeising et al., 2023). What is often done with these types of systems is to rotate the antennas in small increments through 180 degrees to get an azimuthal dependence on the recorded signals, similar to what was done in the early days of studying polarization of radar waves in ice (Hargreaves, 1977). Ice sheets were first discovered to be birefringent as George R. Jiracek (1967) discovered that the return power from the base of the ice was not independent of the orientation of the transmitter and receivers. However, with phase-sensitive radar, it is possible to study not only the signal strength but also the phase, and with digital recording, the phase and amplitude of the signals can be tracked throughout the ice column. The phase difference of the slow and fast waves is naturally related to the COF anisotropy, which is the basic idea behind the coherence methods described below.

The coherence of two orthogonal co-polarized signals, $s_{HH}(t)$ and $s_{VV}(t)$, can be expressed as (Dall, 2010),

$$C_{HHVV}(t) = \frac{\langle s_{HH}(t) s^*_{VV}(t) \rangle}{\sqrt{\langle |s_{HH}(t)|^2 \rangle} \sqrt{\langle |s_{HH}(t)|^2 \rangle}} \tag{4.7}$$

where $\langle \dots \rangle$ is the expectation value and * is the complex conjugate. The expectation value is taken to be over some finite time window of length T, in which case equation 4.7 can be rewritten as,

$$C_{HHVV}(t) = \frac{\int_t^{t+T} s_{HH}(t') s^*_{VV}(t') dt'}{\sqrt{\int_t^{t+T} |s_{HH}(t')|^2 dt'} \sqrt{\int_t^{t+T} |s_{VV}(t')|^2 dt'}} \tag{4.8}$$

The coherence, C_{HHVV}, is a complex number with magnitude between 0 and 1, and phase that estimates the phase difference between the two signals s_{HH} and s_{VV}. The

coherence can be considered a measure of how similar the two signals are. The coherence phase is naturally related to the phase speeds of the two wave components, and multiple studies have used the gradient of the coherence phase to estimate the eigenvalue difference as a function of depth (Jordan et al., 2019, 2020; T. J. Young et al., 2021; Ershadi et al., 2022). It requires that the principal axes of the COF are known, but this can, in some cases, also be derived from the same method. The method is very elegant, as it can get the eigenvalue difference as a function of depth without the need for strong reflectors to trace, like the travel-time difference, and has been proven to give good results. One limitation is that azimuthal coverage of both HH and VV is required, or a full polarimetric radar (HH, HV, VV, VH) is required to synthesize the azimuthal response. However, when Zeising et al. (2023) tried to apply the method presented by Ershadi et al. (2022) to ApRES data collected at NEGIS near the EastGRIP camp, it proved problematic and was abandoned. In Zeising et al. (2023), they mention that this was due to the COF rotating several times with depth. However, a recent study Zeising et al. (2024) found that the issue was related to the strength of the anisotropy versus the radar's range resolution. NEIGS is unique compared to most other places where this method has been used before because it has a very strong horizontal anisotropy combined with depths of more than 2 km. This means that the difference in phase speed between the two waves will separate them to such a degree that a reflection in HH has no overlap with the same reflection in VV, in the COF-aligned case, and hence no coherence. The issue stems from comparing the received signals in travel time and not in true depth. Migrating the signals to true depth requires us to know the anisotropy of the ice, which is what we try to estimate in the first place.

Radar model

A model for how a radar wave's phase and amplitude evolve through birefringent ice can be a useful tool in interpreting radar data. This section summarizes the model presented by Fujita et al. (2006) in a framework used in chapter 6.

The model is based on sequential matrix multiplication that describes the evolution of the phase and amplitude of a radar wave traveling through a layered medium, where each layer has predefined permittivity, conductivity, and scattering coefficients. The electrical field transmitted by the antennas, $\mathbf{E}_T$, is written in the reference system of the antennas, i.e., the electric field component parallel, E_{PT}, and orthogonal, E_{OT}, to the antenna orientation,

$$\mathbf{E}_T = \begin{pmatrix} E_{PT} \\ E_{OT} \end{pmatrix}. \tag{4.9}$$

The downward propagating wave incident to the scattering boundary at the i$^{\text{th}}$ layer is called

$$\mathbf{E}_i = \begin{pmatrix} E_{P,i} \\ E_{O,i} \end{pmatrix}. \tag{4.10}$$

The upward propagating wave scattered from the boundary of the i$^{\text{th}}$ layer is called,

$$\mathbf{E}'_i = \begin{pmatrix} E'_{P,i} \\ E'_{O,i} \end{pmatrix}. \tag{4.11}$$

The received signal from the i$^{\text{th}}$ layer at the antenna is called,

$$\mathbf{E}^R_i = \begin{pmatrix} E_{PR,i} \\ E_{OR,i} \end{pmatrix}. \tag{4.12}$$

The model then consists of a 2x2 transmission matrix $\mathbf{T}$ and a 2x2 scattering matrix $\mathbf{S}$, which, for convenience, is written in the eigenframe of the ice and then rotated into the reference frame of the antennas.

The transmission, through the i$^{\text{th}}$ layer, is written as[1]

$$\mathbf{T}_i = \begin{pmatrix} T_{i,x} & 0 \\ 0 & T_{i,y} \end{pmatrix}, \quad \begin{aligned} T_{i,x} &= \exp\left(-jk_0\Delta z_i + jk_{i,x}\Delta z_i\right) \\ T_{i,y} &= \exp\left(-jk_0\Delta z_i + jk_{i,y}\Delta z_i\right) \end{aligned} \tag{4.13}$$

where $k_{i,x}$ and $k_{i,y}$ are the wavenumbers in the ice along the two horizontal principal components of the COF, Δz_i is the thickness of the i$^{\text{th}}$ layer, and $k_0 = 2\pi/\lambda_0 = 2\pi f_0/c$ is the wavenumber in vacuum.

The wavenumbers in the ice can be written in terms of the permittivities along x and y for the layer, $\varepsilon_{i,x}$ and $\varepsilon_{i,y}$,

$$\begin{aligned} k_{i,x} &= \sqrt{\varepsilon_0\mu_0\varepsilon_{i,x}\omega^2 + j\mu_0\sigma_{i,x}\omega} \\ k_{i,x} &= \sqrt{\varepsilon_0\mu_0\varepsilon_{i,y}\omega^2 + j\mu_0\sigma_{i,y}\omega} \end{aligned}$$

where $\sigma_{i,x}$ and $\sigma_{i,y}$ is the conductivity of the ice along x and y. A 2x2 matrix describes the scattering at the boundary of layers i and $i+1$,

$$\mathbf{S}_i = \begin{pmatrix} S_{i,x} & 0 \\ 0 & S_{i,y} \end{pmatrix}. \tag{4.14}$$

The full radar model can then be expressed with the following three relations,

$$\begin{aligned} \mathbf{E}_n &= \frac{\exp(jk_0 z)}{4\pi z} \prod_{i=1}^{n} \left[\mathbf{R}(\theta_i)\mathbf{T}_i\mathbf{R}(-\theta_i)\right] \mathbf{E}_T \\ \mathbf{E}'_i &= \mathbf{R}(\theta_i)\mathbf{S}_i\mathbf{R}(-\theta_i)\mathbf{E}_i \\ \mathbf{E}^R_n &= \frac{\exp(jk_0 z)}{4\pi z} \prod_{i=n}^{1} \left[\mathbf{R}(\theta_i)\mathbf{T}_i\mathbf{R}(-\theta_i)\right] \mathbf{E}'_n \end{aligned} \tag{4.15}$$

[1] Transmission is perhaps a little confusing name in the context of optics as it does not reference the transmission at a reflective interface. It is the evolution of the phase as the wave travels through a layer of a given thickness and electrical properties.

where $R(\theta)$ is the 2D rotation matrix, and it is assumed that the reference frame of the scattering matrix and transmission are the same, i.e., scattering anisotropy happens along the same axis as the birefringence. The three relations above can be summarized as matrix operators acting on electric field vectors. The operators can be defined and combined into a single matrix operator as follows,

$$\left.\begin{aligned} \widetilde{\mathbf{T}}_n &= \prod_{i=1}^{n} \mathbf{R}(\theta_i)\mathbf{T}_i\mathbf{R}(-\theta_i) \\ \widetilde{\mathbf{S}}_n &= \mathbf{R}(\theta_n)\mathbf{S}_n\mathbf{R}(-\theta_n) \\ \widetilde{\mathbf{T}}_n^R &= \prod_{i=n}^{1} \mathbf{R}(\theta_i)\mathbf{T}_i\mathbf{R}(-\theta_i) \end{aligned}\right\} \Rightarrow \mathbf{M}_n = D(z_n)^2\widetilde{\mathbf{T}}_n^R\widetilde{\mathbf{S}}_n\widetilde{\mathbf{T}}_n \tag{4.16}$$

where $D(z_n) = \frac{\exp(jk_0z)}{4\pi z}$. The relation between the transmitted and received signal from layer n is then simply $\mathbf{E}_n^R = \mathbf{M}_n\mathbf{E}_T$. If only one component in $\mathbf{E}_T$ is non-zero, then the elements of $\mathbf{M}_n$ are proportional to the polarimetric signal,

$$\mathbf{M}_n \propto \begin{pmatrix} s_{HH,n} & s_{HV,n} \\ s_{VH,n} & s_{VV,n} \end{pmatrix}. \tag{4.17}$$

A change in antenna orientation can be modeled as a constant shift of $\theta(z)$ by an angle γ, which can be written as $\mathbf{M}_n(\gamma) = \mathbf{R}(-\gamma)\mathbf{M}_n\mathbf{R}(\gamma)$, see appendix C.

Chapter 5

Double Reflections

In the previous chapter, we found that the travel-time difference recorded between the HH and VV echograms can be translated to a depth-averaged horizontal eigenvalue difference for the COF. However, the method relied on the H and V polarizations being closely aligned with the horizontal eigenvectors of the COF. When following layers in the HH and VV echograms throughout the UWB survey (see figure 3.3), we noticed that sometimes single layers in the ice would split into two, or vice versa. Most of these occurrences are connected to a change in the driving direction, i.e., the antenna orientation. Figure 5.1 shows an example of this, where two reflections turn into one reflection after the radar changes driving direction. The double reflections represent a mixed state between the pure COF-aligned HH and VV signals, meaning there is no travel-time difference between the HH and VV echograms. However, if the reflections can be recognized as double reflections, then the separation between the two reflections gives the birefringence-induced travel-time difference. On top of this, the relative amplitude of the two reflections must, in some way, be related to how misaligned the antennas are to the COF orientation. In the paper included below, we use the travel-time separation of the double reflection pairs, together with their relative amplitude, to derive both the depth-averaged eigenvalue difference as well as the absolute orientation of the COF. This is the first time double reflections have been described and used to derive the orientation and eigenvalue difference of the COF. The method is unique because it only relies on the amplitude of the return signal and can be used on radars with a single polarization. If a survey were designed to get double reflections, which the 2022 NEGIS survey was not, it would be possible to get continuous estimates of the COF without the need for the full polarimetric signal. It opens the possibility of going back and looking at older data where only a single polarization is recorded and using the double reflections method to derive information about the COF. In the case of single polarization surveys, it is only possible to get eigenvalue differences and not the orientation.

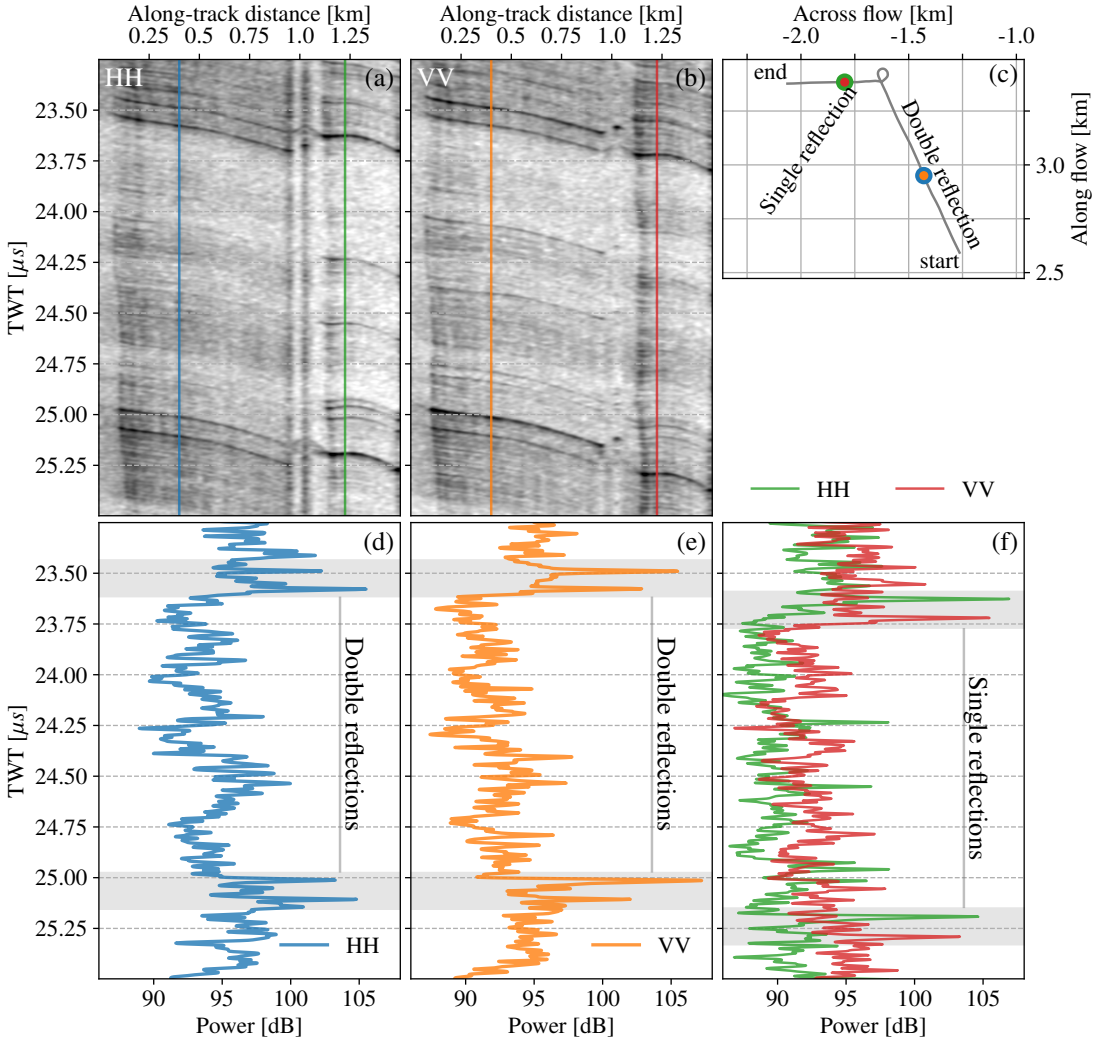

Figure 5.1: An example of double reflections observed inside NEIGS at the survey line labeled 2022/06/27 in figure 3.3. (c) shows the driving line with the two axes being along- and across-flow distance from EastGRIP. (a-b) show the HH and VV echograms collected along the line shown in (c) zoomed in on two layers that produce two pairs of double reflections. The first pair is around 23.5 µs, and the second is around 25.0 µs. Echograms have been convolved along vertical and along-track with a Gaussian with a 4ns and 40 m standard deviation, respectively. (d-e) show individual HH and VV traces at a location with double reflections; see blue and orange lines in (a) and (b). (f) shows individual HH and VV traces a bit further along track at a location without double reflections; see green and red lines on (a) and (b).

Implications for radar surveys

The implications of recording reflections from both the slow and the fast waves in radar surveys have not been discussed before. For typical glacial conditions with relatively weak horizontal anisotropy, the two reflections may overlap and not present themselves as separate reflections but as one broad reflection. However, as radar bandwidth increases, so does the detectability of double reflections. One obvious implication of this is matching isochrones in echograms to layers in an ice core. At EastGRIP, if the radar survey is not aligned with the COF, the echogram may become cluttered by double reflections, making it difficult to unambiguously match a reflection to a layer. Similarly, having double reflections come and go with the changing orientations of the antennas will undoubtedly challenge even the most sophisticated algorithm for automated tracking of internal reflections. Even a manual tracker can struggle to know what to do, which is precisely how we came to notice the double reflections in the first place. An interesting point that Nicholas Holschuh brought up in the review process of the manuscript was the problem of comparing the phase of repeat measurements using ApRES, for example, when calculating basal melt rates. Double reflections represent a mixed state of propagating speeds and, therefore, also wavelengths. If you consider the delta phase of repeat measurements, then the signal's wavelength matters for converting the delta phase to a change in depth. The exact implications need more thought, but double reflections in the data could cause trouble when tracking the delta phase throughout the ice column.

The paper

First submitted to Geophysical Research Letters on 30 May 2024; submitted in revised form on 26 August 2024, and again on 5 December 2024; accepted 6 December 2024. While the manuscript is accepted for publication, it has not yet been published. The included text below is the accepted version. The supporting information is included in Appendix D

Double reflections in polarized radar data reveal ice fabric in the North East Greenland Ice Stream

Niels F. Nymand[1], David A. Lilien[2,3], Tamara A. Gerber[1], Christine S. Hvidberg[1], Daniel Steinhage[4], Prasad Gogineni[5], Drew Taylor[5], Dorthe Dahl-Jensen[1,2]

[1]Niels Bohr Institute, University of Copenhagen
[2]Centre for Earth Observation Science, University of Manitoba
[3]Department of Earth and Atmospheric Sciences, Indiana University
[4]Alfred Wegener Institute, Helmholtz Centre for Polar and Marine Research
[5]Remote Sensing Center, University of Alabama

Key Points:

- We present a novel method for deriving strength and orientation of crystal orientation fabric using double reflections in birefringent ice.
- Method reveals a 12-degree rotation of the crystal orientation fabric relative to flow at the center of the North East Greenland Ice Stream
- An asymmetry of the crystal orientation fabric across center of the ice stream indicates more variable flow than previously assumed

Corresponding author: Niels F. Nymand, `niels.nymand@nbi.ku.dk`

Abstract

The orientation of ice crystals within large ice masses has a strong influence on their mechanical properties, but cannot be directly observed from the surface. The bulk birefringence of anisotropic ice allows us to infer information about the crystal orientation fabric (COF) from polarized radar measurements. Here, we show a new approach for determining the orientation and strength of horizontal COF anisotropy from two radar reflections originating from the same physical layer in birefringent ice. We apply this method to data collected as part of a ground-based radar survey of the North East Greenland Ice Stream. We observe a 12-degree clockwise rotation of the fabric at the center of the ice stream, and a tendency towards a flow-aligned COF further southeast. This asymmetry across the ice-stream centerline adds to growing evidence for a more variable ice stream than previously assumed.

Plain Language Summary

The ice in glaciers and ice sheets is composed of crystals, small pieces of ice which can differ in shape and orientation. How ice crystals are arranged is closely linked to how ice sheets move and behave, which is important for predicting changes in polar ice sheets and their impact on sea level rise. Even though the arrangement of the crystals is not directly observable from the surface of ice sheets, we can use specific types of radar measurements to extract general information about how the crystals are arranged. In this study, we present a new approach for doing this. We test the method on data collected as part of a survey of the North East Greenland Ice Stream, which drains 16% of the area of the Greenland Ice Sheet. Our results show that the crystals are not aligned in the way we expected, suggesting that the flow pattern of the ice stream has changed in the past and is not as stable as previously thought.

1 Introduction

The orientation of grains within polycrystalline ice, or crystal orientation fabric (COF), is a fundamental property that governs ice flow. Ice is mechanically anisotropic (Duval et al., 1983), so good estimates of the COF in dynamically interesting areas, such as ice streams, are crucial for constraining the directional viscosity of ice. If ignored, directional hardening or softening caused by the COF can lead to errors when inferring basal conditions (Rathmann & Lilien, 2022), modeling depth-age relationships at ice divides (Martín et al., 2009), or considering the strength of shear margins (Grinsted et al., 2022; Minchew et al., 2018). Improved understanding of the COF can thus contribute to more accurate modeling of ice stream behavior. Since flow variability causes half of the Greenland ice sheet's annual mass loss (Shepherd et al., 2020), this understanding helps reduce uncertainties in future sea level projections.

COF can be measured or inferred in multiple ways. The most direct is using ice cores to derive the orientation of individual grains in the ice (Durand et al., 2006; Montagnat et al., 2014). However, except with highly resolved layering, cores provide only point measurements and absolute orientation is usually lost (Westhoff et al., 2021). Seismics offer an alternative to ice cores by utilizing the elastic anisotropy of ice (Picotti et al., 2015; Smith et al., 2017) to

estimate the COF. Another commonly used, and logistically simpler, method for estimating the COF is with polarized radar measurements.

Radar sounding has long been used to recover information about the COF (Hargreaves, 1977). In glacial ice, the dielectric anisotropy of individual ice crystals can alter the polarization state of the transmitted radar waves (Jiracek, 1967). Anisotropic COFs inherit this property, which affects both the travel-time and polarization state of radar waves. It is common to approximate the COF using a second-order structure tensor, using its eigenvectors and eigenvalues to describe the orientation and strength of the COF. The propagation of radar waves in ice is only sensitive to the second-order structure tensor (Rathmann et al., 2022). In recent years, fully polarimetric radar sounding, including both the co-polarized (transmitting and receiving at the same polarization) and the cross-polarized (transmitting and receiving at orthogonal polarizations) orientations, has become a powerful tool in deriving the horizontal eigenvectors and eigenvalues (Fujita et al., 2006; Jordan et al., 2019; Dall, 2020; Ershadi et al., 2022) using simple radar models together with radar-derived coherence and power anomalies. A new and simpler approach involves measuring the travel-time difference in reflections from the bed or internal layers (Gerber et al., 2023; Zeising et al., 2023) between multiple co-polarized measurements. In anisotropic ice, radar energy must be polarized along the principal axes of the COF, so if the transmitted wave is misaligned with the COF it is split into two waves. These waves have slightly different propagation speeds (Fujita et al., 2006).

Here, we demonstrate that travel-time and amplitude analysis of double reflections in co-polarized data offers a way of inferring the horizontal anisotropy and orientation of the COF, assuming no rotation with depth. First, we present the observations of double reflections, caused by birefringence, collected as part of a larger ground-based radar survey of the North East Greenland Ice Stream (NEGIS), which form the basis of the analysis. Second, we explain why double reflections arise and present a method to use them to infer information about the COF. Third, we derive orientation and horizontal eigenvalue differences of the COF inside NEGIS by applying the new method to the observed double reflections. Lastly, we compare our results to the ice core from the East Greenland Ice Core Project (EastGRIP) (Westhoff et al., 2021; Zeising et al., 2023) and a fabric evolution model presented in Gerber et al. (2023).

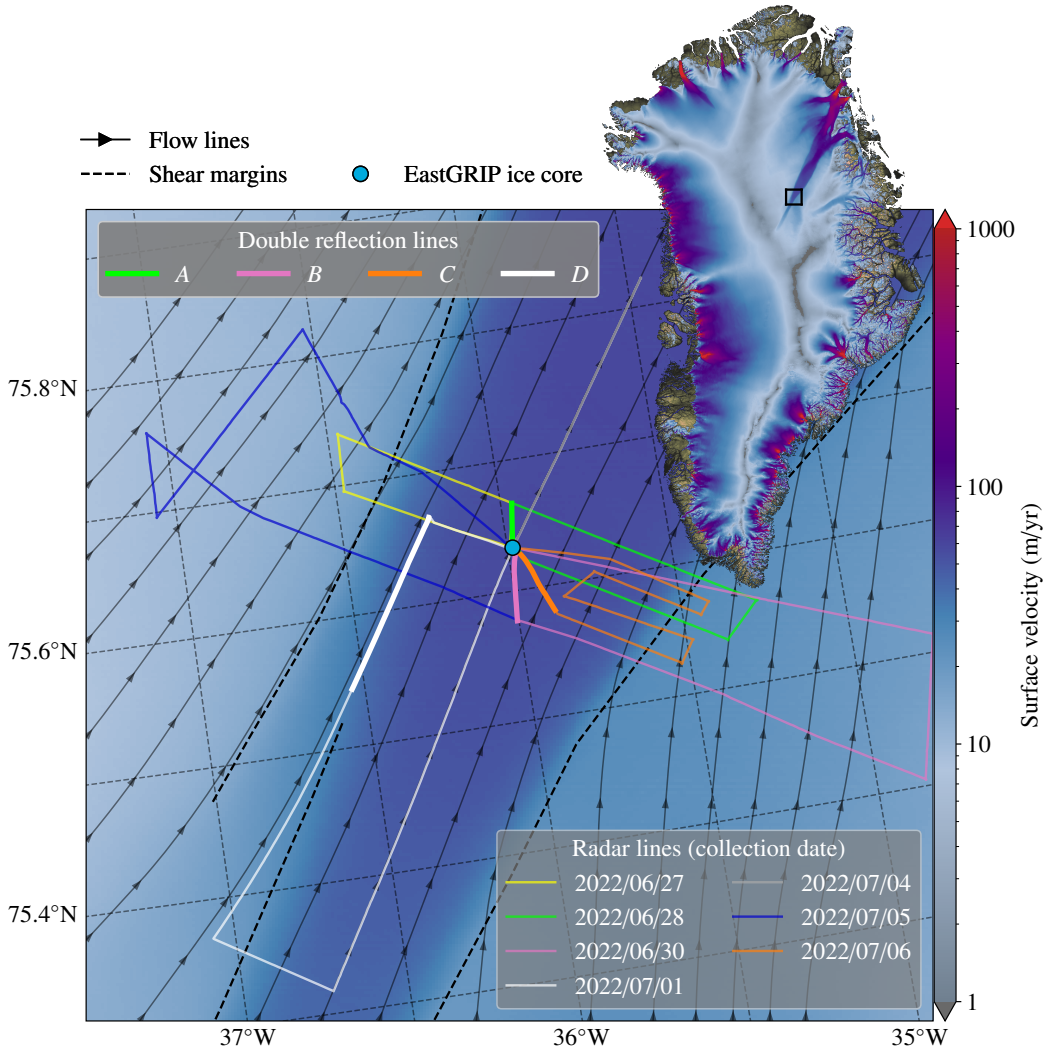

Figure 1: Overview of the 2022 ground-based radar campaign near the EastGRIP drill site, located in the interior, southwestern region of NEGIS. The black rectangle outlines the survey area. Black dashed lines show the estimated location of the NEGIS shear margins. Black lines with arrowheads show the flow lines. Velocity data was obtained from the NASAs MEaSUREs multi-year dataset (Joughin et al., 2016, 2018)

2 Data: Ground-based UWB polarized radar

The data used in this study were recorded with a ground-based, ultra-wideband, quad-polarized radar system developed by the University of Alabama (Li et al., 2020). Over the course of two weeks in June and July 2022, we collected more than 500 line-km of radar at NEGIS (Figure 1). The radar operated at center frequency 330 MHz with bandwidth 300 MHz. In this survey, the entire radar system was dragged behind a Skidoo at a speed of about 10 km/h. The radar electronics and operator were towed inside an enclosed sled (PolyPod, Figure 2). The antenna panels were dragged on an inflatable balloon behind the PolyPod.

The radar switched between four polarization modes (HH, HV, VV, VH), where V and H indicate along-track or across-track polarization of the transmit and receive antennas, at a pulse repetition frequency of 5kHz. Along with the four polarization modes, we also alternated between two chirp lengths, 10µs and 1µs. We only use the 10µs data here as it penetrates deeper and, as we will show below, the separation between double reflections depends on the integrated anisotropy of the ice through which the radar waves travel. The antenna is able to distinguish polarizations with a cross-polarization leakage of -30 dB or better for most of the frequency spectrum (Li, 2021).

Processing of the raw radar data was done using custom scripts and consists of coherent integration, pulse compression, incoherent integration, channel integration and interpolation to a consistent grid.

2.1 Double reflections

In connection with tracking layers, we noticed that layers sometimes split and merge, making the tracking ambiguous. Because we could compare HH and VV, it became apparent that this was most likely an effect of birefringence. This could potentially make the process of automated tracking very difficult, and complicate matching layers between ice core conductivity or dielectric measurements and radar layers.
We interpret these split layers as single physical layers in the ice that reflect two orthogonally polarized waves, split by the birefringence, and returning to the receiver at different times depending on the strength of the birefringence. The partitioning of energy of the two waves, and thereby the recorded amplitudes, is determined by the degree of alignment of the radar antennas and horizontal eigenvectors of the COF. An example of observed double reflections is shown in Figure 2, together with a sketch of the ideas presented here.

Only a very small subset of the data convincingly show these double reflections, most likely due to insufficient misalignment between horizontal eigenvectors of the COF and radar antennas, and most internal reflectors disappear near shear margins where we might expect radar antennas to be misaligned with the COF.

In the following, we provide the theoretical basis for double reflections and demonstrate how it can be used to derive an estimate for the COF.

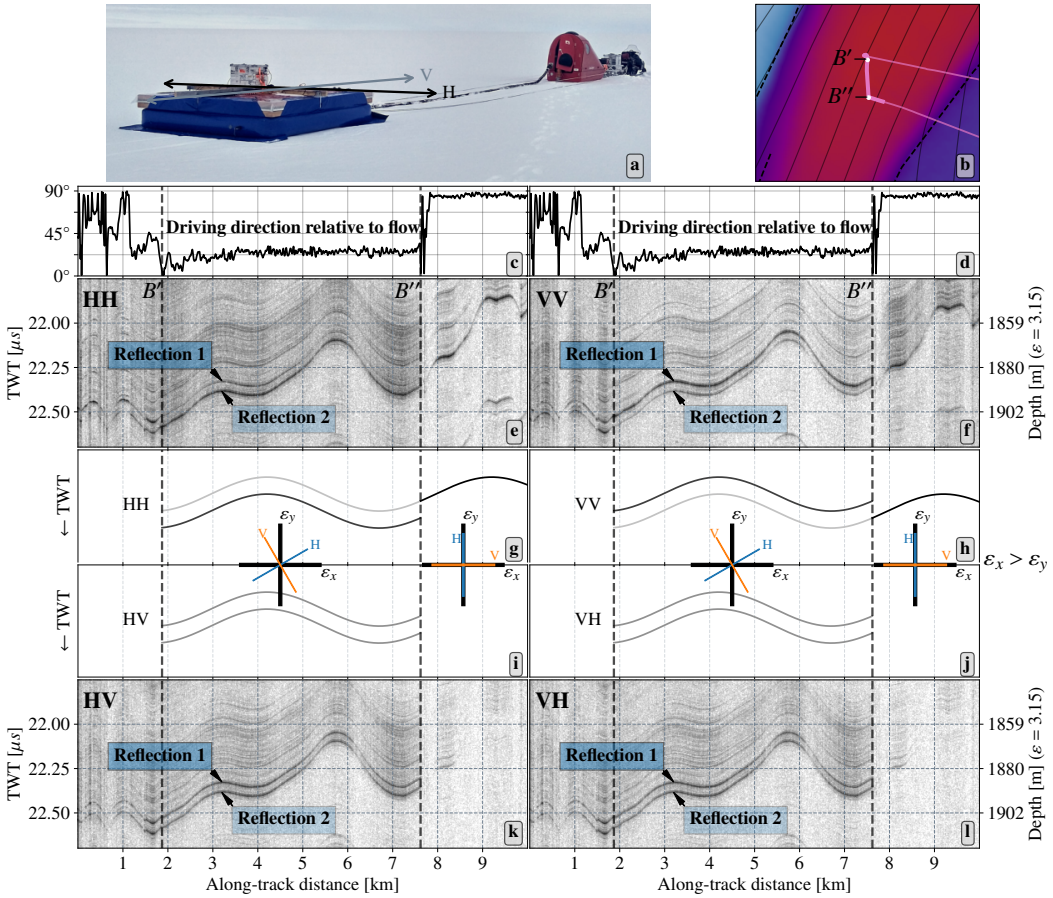

Figure 2: UWB radar and double reflections at NEGIS. (a) shows the radar as it was operated in 2022. (c,d) show the driving direction of the radar relative to the local flow vector. (e,f) is a side by side comparison of HH and VV radargrams collected along the wide pink line on the velocity map in (b), zoomed in on a double reflection ($B' - B''$). (k,l) show the HV and VH radargrams. (g-j) show a sketch of double reflections.

3 Theory

To explain these double reflections, we need to consider the electromagnetic properties of ice in the VHF to UHF frequency range. In this frequency range, ice crystals are birefringent with permittivity $\varepsilon_{\parallel}$ and $\varepsilon_{\perp}$ parallel and perpendicular to their optical axis, respectively. However, the typical size of individual ice crystals is on the order of 0.5 mm to 10 mm (Thorsteinsson et al., 1997; Svensson et al., 2007), which is around two orders of magnitude smaller than the center wavelength of the radar system (∼0.5 m in ice). It is therefore appropriate to describe the ice by its bulk properties. For the following we assume that the COF has a vertical eigenvector, pointing along z, and x and y define the two horizontal eigenvectors. The bulk permittivity of ice can be related to the permittivity

of a single ice crystal through the bulk permittivity tensor (Fujita et al., 2006),

$$\boldsymbol{\varepsilon}_b = \begin{pmatrix} \varepsilon_\perp + \Delta\varepsilon\lambda_x & 0 & 0 \\ 0 & \varepsilon_\perp + \Delta\varepsilon\lambda_y & 0 \\ 0 & 0 & \varepsilon_\perp + \Delta\varepsilon\lambda_z \end{pmatrix}, \tag{1}$$

where $\Delta\varepsilon = \varepsilon_\parallel - \varepsilon_\perp$, λ_x, λ_y and λ_z express the normalized eigenvalues of the COF, within the eigenframe of the COF, (x,y,z). We assume the commonly used values $\Delta\varepsilon = 0.034$ and $\varepsilon_\perp = 3.15$ (Fujita et al., 2000).

In the case that $\lambda_x \neq \lambda_y$ and the radar waves propagate vertically, the electrical fields are polarized according to the horizontal principal axes of the permittivity tensor (Fujita et al., 2006), and differently polarized waves will be split. In other words, when the polarization of a radar wave is not aligned with the horizontal eigenvectors, the bulk birefringence of the ice splits the wave into two waves, polarized along x and y. The two waves have different propagation speeds, due to the difference in permittivity. As a result we see two reflections at different travel times from the same layer in the ice.

3.1 Travel time difference

If the travel-time difference exceeds the range resolution of the radar we can use it to derive the horizontal eigenvalue difference, $\Delta\lambda = \lambda_x - \lambda_y$, where we define $\lambda_x > \lambda_y$. The two way travel-time (TWT) for polarizations along the two horizontal principal axes, x and y, can be expressed as,

$$t_x(d) = \frac{2d}{c}\sqrt{\varepsilon_\perp + \Delta\varepsilon\lambda_x}, \qquad t_y(d) = \frac{2d}{c}\sqrt{\varepsilon_\perp + \Delta\varepsilon\lambda_y}, \tag{2}$$

where d is the depth measured from the surface of the ice and c is the speed of light in vacuum. These relations can be rearranged to derive $\Delta\lambda$ given the observed travel times,

$$\Delta\lambda = \lambda_x - \lambda_y = \left(\frac{c}{2d}\right)^2 \frac{t_x^2 - t_y^2}{\Delta\varepsilon} = \frac{t_x - t_y}{t_x + t_y}\frac{4\bar{\varepsilon}}{\Delta\varepsilon}, \quad \text{for } d = \frac{c}{\sqrt{\bar{\varepsilon}}}\frac{1}{4}(t_y + t_x), \tag{3}$$

where we define $\lambda_x > \lambda_y$ and $\bar{\varepsilon} = \frac{2}{3}\varepsilon_\perp + \frac{1}{3}\varepsilon_\parallel$ (permittivity of isotropic ice). The error in $\Delta\lambda$ from assuming isotropic travel speeds for estimating d is small compared to the uncertainty from estimating t_x and t_y.

3.2 Relative amplitude of double reflections

The initial relative amplitude of the two downward-propagating waves is determined by ϕ. For the H wave the amplitudes of the two waves, H_x and H_y, can be related to the amplitude of the transmitted wave, H_T, as,

$$H_x = H_T \cos\phi, \quad H_y = H_T \sin\phi. \tag{4}$$

The components of the V wave are computed analogously. As these waves travel through the ice column, each encounters reflectors that reflects a fraction of the wave back towards the surface. If the travel-time difference and amplitudes are large enough, they will appear as two separate reflections to an antenna not aligned with the principal axes. At the surface, the waves will have decreased in amplitude, which we parameterize by two pre-factors, L_x and L_y, which might differ due to anisotropic scattering. The returned amplitudes of

the two waves are then $L_x H_x$ and $L_y H_y$. For a co-polarized measurement, the recorded amplitudes are $L_x H_x \cos\phi$ and $L_y H_y \sin\phi$. The ratio of the amplitudes for the co-polarized measurements can be written as

$$R_{HH} = \frac{L_x}{L_y} \cot^2\phi, \quad R_{VV} = \frac{L_x}{L_y} \tan^2\phi. \tag{5}$$

For an illustration of the relative amplitudes at transmit and receive, see Supplementary Figure S1. Amplitudes are usually presented on a logarithmic scale defined by $P_{dB}(a) = 10\log_{10}|a|^2$, where a is the amplitude of the recorded signal and P_{dB} is a measure of the power of the recorded signal expressed in dB. We therefore use a rewritten version of equation 5,

$$\begin{aligned} \Delta P_{HH} &= 20\log_{10}\left(\frac{L_x}{L_y}\right) - 40\log_{10}(\tan\phi) \\ \Delta P_{VV} &= 20\log_{10}\left(\frac{L_x}{L_y}\right) + 40\log_{10}(\tan\phi), \end{aligned} \tag{6}$$

where ΔP_{HH} and ΔP_{VV} is the power difference in dB between the second and first reflection in HH and VV mode, respectively (Figure 2).

Cross-polarized measurements can be used to eliminate the term depending on L_x and L_y. Following the derivation of equation 6, the power differences for cross-polarized measurements are,

$$\Delta P_{HV} = \Delta P_{VH} = 20\log_{10}\left(\frac{L_x}{L_y}\right). \tag{7}$$

If cross-polarized measurements were not available, $\Delta P_{HH} - \Delta P_{VV}$ could be used to derive ϕ independent of L_x and L_y. If only one co-polarized measurement were available, cross points might be used to eliminate the first term in equation 6.

4 Methods

We now apply this theory to the data collected at NEGIS to derive ϕ and $\Delta\lambda$. First, we trace pairs of reflections. The travel-time difference of the reflections allows us to derive the eigenvalue difference using equation 3. For lines without double reflections the eigenvalue differences is derived by comparing travel-times for layers in HH and VV, similar to cross-point analysis (Gerber et al., 2023).

Determining the fabric orientation from the amplitude of the reflections is more complicated. First, the amplitude is calculated as the maximum value in a 5 sample window centered around the picked reflection. We use the mean and standard deviation of the signal amplitude between the two reflections to define the noise level. Locations where the amplitude of either picked reflector does not exceed the noise level by at least 4 dB are discarded. A schematic of the workflow can be found in the supplementary Figure S2.

We use the cross-polarized data to calculate a corrected power difference,

$$\begin{aligned} \overline{\Delta P}_{HH} &= \Delta P_{HH} - \tfrac{1}{2}(\Delta P_{HV} + \Delta P_{VH}) = -40\log_{10}(\tan\phi) \\ \overline{\Delta P}_{VV} &= \Delta P_{VV} - \tfrac{1}{2}(\Delta P_{HV} + \Delta P_{VH}) = 40\log_{10}(\tan\phi). \end{aligned} \tag{8}$$

ϕ can then be estimated independently for HH and VV by rearranging equation 8 to get

$$\begin{aligned} |\phi_{HH}| &= \arctan\left(10^{-\overline{\Delta P}_{HH}/40}\right) \\ |\phi_{VV}| &= \arctan\left(10^{\overline{\Delta P}_{VV}/40}\right), \end{aligned} \tag{9}$$

where ϕ_{HH} and ϕ_{VV} are independent estimates of ϕ derived from the HH and VV radargrams, respectively.

Equation 9 has two solutions; the sign of ϕ is ambiguous without additional information. Minor fluctuations in the driving direction, and consequently in radar orientation during data collection, allow the sign to be determined. If we assume that the orientation of the COF changes over much greater distances than the radar orientation, we can determine the sign of ϕ by cross-correlating the along-track gradient of the power difference with the along-track gradient of $|\phi|$. For the HH case,

$$\begin{aligned} \phi > 0, \text{ if } \quad \text{sign}\left(\frac{d(\Delta P_{HH})}{ds}\right) &= -\text{sign}\left(\frac{\partial|\phi_{HH}|}{\partial s}\right) \\ \phi < 0, \text{ if } \quad \text{sign}\left(\frac{d(\Delta P_{HH})}{ds}\right) &= +\text{sign}\left(\frac{\partial|\phi_{HH}|}{\partial s}\right) \end{aligned} \tag{10}$$

where s represents the along-track coordinate. For VV we just flip the signs of equation 10. To determine the COF orientation, we thus calculate two estimates of ϕ, each following equation 9 to get $|\phi|$ and equation 10 to find sign(ϕ).

Because the energy is split between two waves, we need strong reflectors for the signal to rise above the noise. Across different radar lines, we found three reflectors that were consistently well suited to carry out the analysis. They are approximately 2 km deep at EastGRIP and have been found all over Greenland (Jacobel & Hodge, 1995; Dahl-Jensen et al., 2003, 2013; Gerber et al., 2021). Because they are strong reflectors and lie in an otherwise relatively echo-free zone, they are easily picked and rise well above the noise. They are also deep enough for the travel-time difference to be significant at the COF strength around NEGIS. We thus obtain up to six independent estimates of the fabric strength and orientation (two polarizations times three layers) at every radar trace.

This method relies on these reflections originating from one physical layer, not two closely spaced, orthogonally scattering layers that mimic the relative amplitudes of double reflections. Having multiple layers showing the same pattern can help distinguish between these possibilities. The HV or VH data can also reveal if the layers are subject to strong anisotropic scattering.

5 Results

Across the center of the ice stream, we observe a small increase in the rotation of the COF with respect to flow as we move from B'' towards the center at B' and a constant rotation of $12 \pm 5°$ from the center at A'' to A'. This is followed by a generally increasing eigenvalue difference from $\Delta\lambda = 0.42$ at B'' to $\Delta\lambda = 0.7$ at A'. Unlike most glacier settings, this implies that c-axes are primarily horizontal, associated with flow convergence and lateral compression. Upstream with increasing proximity to the southeastern shear margin (C'' to C'), we find a more flow-aligned COF that tends to counterclockwise rotation of the COF at C'. The signal-to-noise ratio generally decreases from C' to C'', decreasing confidence

in the orientation estimates towards C''. Our uncertainty estimates do not fully capture this variation (see supplementary Text S1 and Figure S8 for details). At the northwestern shear margin (D' to D''), we find a constant clockwise rotation of the COF of about 40° with a small increase in the eigenvalue difference from $\Delta\lambda = 0.65$ to $\Delta\lambda = 0.75$ towards D''. Figure 3b includes flow parallel and perpendicular lines with no observed double reflections. Eigenvalue differences for these lines were derived by comparing travel times between the HH- and VV-radargrams for the same three layers used to analyze double reflections. Comparison of HH and VV travel time indicates nearly constant eigenvalue difference along the ice-stream center. The across flow line is asymmetric about the ice-stream center, with a general increase from the southeast to the northwest. Results derived for radar lines 2022/06/27 and 2022/07/05 in Figure 1, are omitted due to overlap with 2022/06/28 and 2022/06/30, respectively. The overlapping lines agree within their respective uncertainties, and detailed results can be found in Supplementary Figures S4-S8.

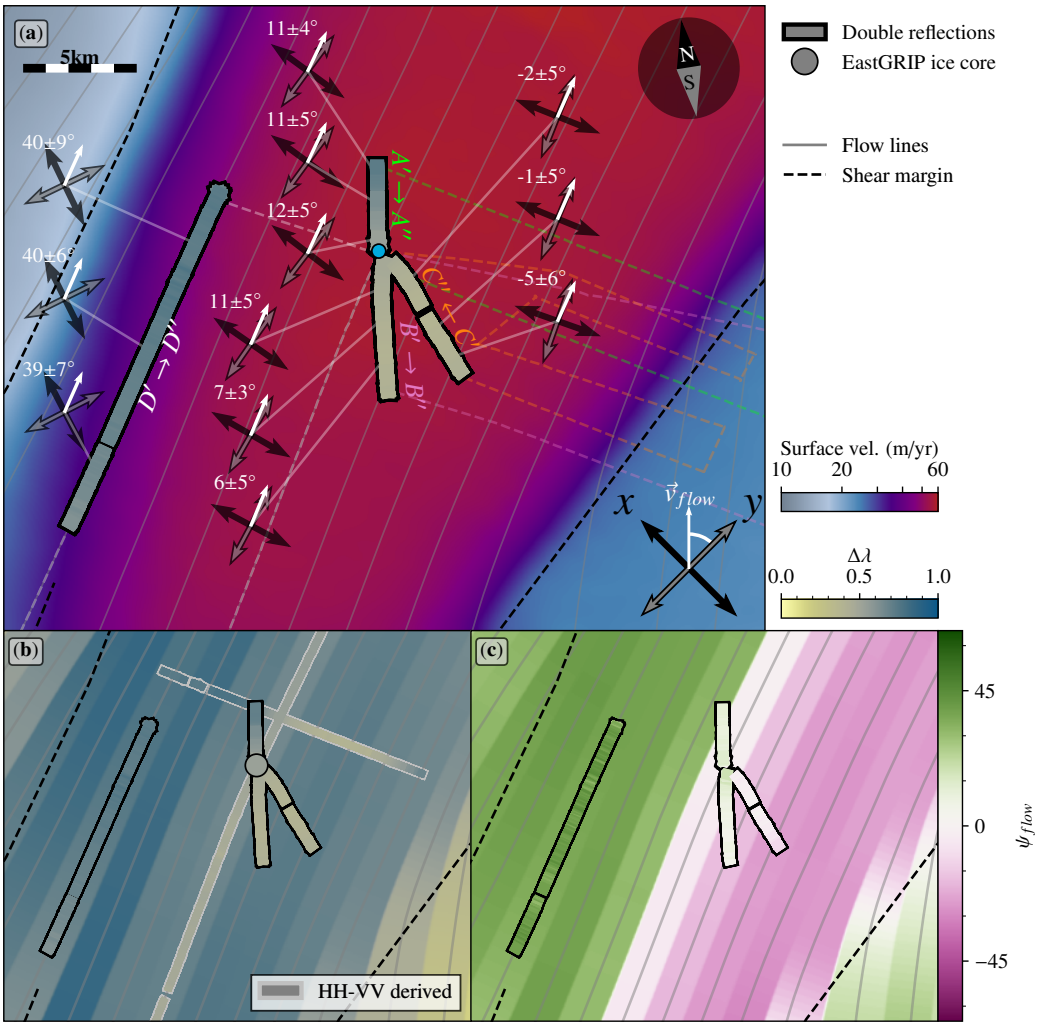

Figure 3: Orientation and strength of COF, derived from double reflections, plotted on top of (a) surface velocity map of NEGIS (Joughin et al., 2016) and (b-c) modeled fabric from (Gerber et al., 2023). (a) The black and gray arrows show the horizontal principal components of the COF, x and y respectively, as derived from the amplitude differences. Arrows show mean values with depth (i.e., across three layers) and distance for sections of each radar line (thirds). The white arrows are the local flow directions, and the white number is the angle between the flow vector and the smallest eigenvalue. Explanation of orientation uncertainty can be found in supplementary text S1. Gray solid lines show flow lines. The yellow-blue colors of the wide lines show the depth-averaged horizontal eigenvalue difference derived from the travel-time difference of the double reflections. (b) Shows eigenvalue differences from double reflections, as well as flow parallel and perpendicular lines with no observed double reflections, plotted on top of the depth averaged modeled horizontal eigenvalue difference. (c) Shows the orientation derived from the double reflections plotted on top of the modeled orientations, where ψ_{flow} is the angle between flow and y. Primed and double primed letters with arrow show the traveling direction from the start to the end of the double reflection lines, respectively.

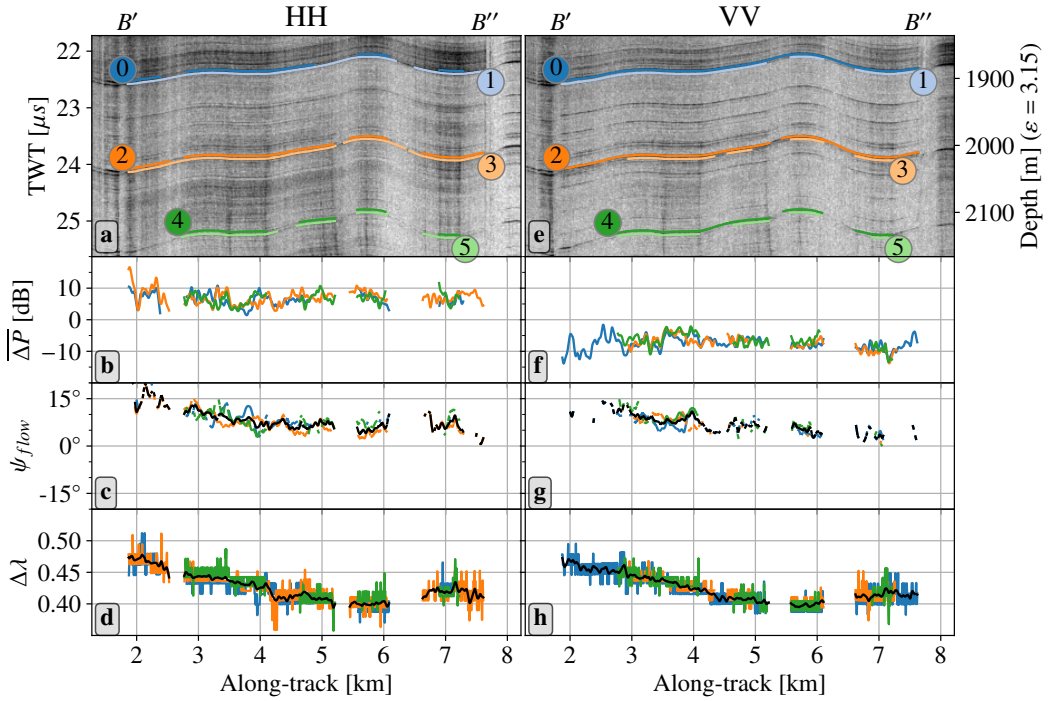

Figure 4: Detailed overview of results from line B in Figure 3. (a) HH-radargram where visible double reflections have been picked in pairs (0,1),(2,3) and (4,5), with the corrected amplitude differences plotted below in (b) for each layer, blue, orange and green. (c) calculated orientations of the smallest eigenvalue relative to flow for each layer with a smoothed mean plotted on top in black. (d) horizontal eigenvalue difference based on the travel-time difference of the reflection pairs picked in (a). (e)-(h) as in (a)-(d), but for VV.

6 Discussion

Our results suggest that the eigenframe of the COF is rotated about 12 degrees relative to flow close to the center of the ice stream. This seemingly contrasts with the reconstruction based on visual stratigraphy of the EastGRIP ice core (Westhoff et al., 2021), which finds that the COF is generally aligned with flow. However, a 12-degree rotation is small compared to the spread of reconstructed c-axis azimuths (Westhoff et al., 2021, Figure 10c_3). The COF above 1375 m, where the ice core orientation has been reconstructed, may be rotated relative to the COF below, though the radar only records a cumulative effect. Only the top 1714 m of the ice-core eigenvalues have been published (Weikusat et al., 2022; Zeising et al., 2023), and assuming a constant COF below 1714 m and isotropic at the surface, the depth-averaged horizontal eigenvalue difference from the ice core is $\Delta\lambda = 0.53 \pm 0.01$ at the depth of the three radar layers. This is in near-perfect agreement with our closest estimate to EastGRIP (A'') which gives $\Delta\lambda = 0.52 \pm 0.01$, which is also in good agreement with the results derived from ApRES (Zeising et al., 2023).

Method limitations

Our new method leverages characteristics of the study site and radar to overcome limitations that may prove problematic when attempting to apply the method in other settings.

The method assumes that the orientation of the eigenvectors remains constant throughout the illuminated ice column. This is partly supported by the ice-core reconstruction, which does not suggest a changing eigenframe in the interval 1375 m-2120 m (Westhoff et al., 2021). The method works best at relatively large misalignment with the eigenvectors, approximately $45° \pm 15°$, to produce sufficient amplitude differences to estimate orientation. A radar with cross-pol leakage comparable to the amplitude difference (∼5-10 dB) may not observe power differences between the two layers, and thus might be confined to estimating $\Delta\lambda$ but not orientation. Radars with low range resolution or low transmit power might struggle to produce strong double reflections at a depth where the travel-time difference exceeds the range resolution. The eigenvalue difference resolvable for a given bandwidth, B, can be expressed as,

$$\Delta\lambda_{min} = \frac{c}{z\ B}\frac{\sqrt{\bar{\varepsilon}}}{\Delta\varepsilon} \approx \begin{cases} 0.26 & \text{for: } B = 30MHz, \quad z = 2km \\ 0.09 & \text{for: } B = 85MHz, \quad z = 2km \\ 0.04 & \text{for: } B = 200MHz, \quad z = 2km \\ 0.026 & \text{for: } B = 300MHz, \quad z = 2km \end{cases} \tag{11}$$

where the range resolution of a radar system with bandwidth B is $\frac{c}{2B\sqrt{\bar{\varepsilon}}}$ (Skolnik, 2001). Supplementary Figure S3 shows a radargram from the MCoRDS radar (Paden et al., 2014), which has been flown for thousands of kilometers over Greenland and Antarctica, with probable double reflections. For radar data with double reflections, every sample is a superposition of scattering events of the two wave components, making interpretation difficult except for bright isolated layers. The layers that we have used (see Figure 4) are found all over Greenland, and are located in an otherwise relatively echo free zone (Jacobel & Hodge, 1995; Dahl-Jensen et al., 2003, 2013; Gerber et al., 2021), suggesting that the method might work in other sections of the ice sheet with strong horizontal anisotropy. We encourage future studies using ice penetrating radar data to consider how double reflections may influence their interpretations.

Comparison with a fabric development model

Comparison between our results and the horizontal anisotropy predicted by a fabric development model offers potential insight into the glaciological conditions at NEGIS (Figure 3(b,c)). We compare our results to a model that simulated COF development under the assumptions that flow has been steady for the past ∼10k years and COF develops solely by lattice rotation. In contrast to the observations, which show symmetry of the orientation and horizontal eigenvalue difference across a plane parallel to but southeast of the current ice-stream centerline, the model predicts symmetry across the ice-stream centerline. That two independently observed parameters, the horizontal eigenvalue difference and orientation, disagree with the model results for the southeastern part of the ice stream suggests that model assumptions do not hold. While there is some uncertainty in the robustness of the modeled eigenvalue difference due to recrystallization (Richards et al., 2023), the lack of rotation of the COF relative to flow is tied to the fundamental physics of COF development and the assumption of steady flow. Since the modern centerline does not cross a shear margin, the ice does not experience shear or rotation, so current understanding of COF development under lattice rotation or recrystallization suggests that if flow has been steady there should be symmetry about the ice-stream centerline. We thus suggest that the

assumption of steady-state flow is mainly responsible for the disagreement between model and observations.

The widening of the shear margins observed in Grinsted et al. (2022) suggests a variable ice stream rather than one in steady state. Franke et al. (2022) observed relic ice streams north of present day NEGIS that were likely active during the Holocene. Jansen et al. (2024) found that the current shear margins of NEGIS were fully formed only 2000 years ago. These three independent lines of evidence all support recent flow changes in or around NEGIS. Conversely, the model results from Gerber et al. (2023) assumed steady flow in the past, so mismatch between model and data could suggest that the COF has not yet adjusted to the new flow configuration. For example, a recent northward migration of the ice stream could explain why the COF is rotated relative to modern flow. Thus, the mismatch between our results and the model could be evidence of an ice stream with a more variable past than commonly assumed.

7 Conclusion

Using double reflections recorded at NEGIS with a new, high-resolution radar system, we have derived information about the COF, namely the orientation of the horizontal eigenframe and the horizontal eigenvalue difference. This new method may enable simpler radar systems with a single, linearly polarized antenna to estimate COF along a radar line, subject to the conditions that $\Delta\lambda$ is large enough and the radar has sufficient power and sensitivity to sound layers deep enough that travel-time differences exceed the range resolution of the radar. We find a strong asymmetry in both the orientation and eigenvalue differences across the modern center of NEGIS. This contrasts with a fabric development model (Gerber et al., 2023), which shows approximate symmetry across the center of the ice stream under the assumption that ice flow has remained steady for the last $\sim$ 10 kyr; the model/data mismatch likely stems from that assumption. Together with recent studies about the age and present-day widening of the NEGIS shear margins (Jansen et al., 2024; Grinsted et al., 2022), as well as the discovery of relic ice streams in northern Greenland (Franke et al., 2022), this work is another piece of evidence for a more variable NEGIS than previously assumed.

Acknowledgments
This research has been supported by the Villum Fond (grant no. 16572), the EGRIP camp and logistical team, the Canada Excellence Research Chairs Program,the Novo Nordisk Foundation (grant no. NNF23OC0081251), and the Danmarks Frie Forskningsfond (grant no. 2032-00364B). EGRIP is directed and organized by the Centre for Ice and Climate at the Niels Bohr Institute, University of Copenhagen. It is supported by funding agencies and institutions in Denmark (A. P. Møller Foundation, University of Copenhagen), USA (US National Science Foundation, Office of Polar Programs), Germany (Alfred Wegener Institute, Helmholtz Centre for Polar and Marine Research), Japan (National Institute of Polar Research and Arctic Challenge for Sustainability), Norway (University of Bergen and Trond Mohn Foundation), Switzerland (Swiss National Science Foundation), France (French Polar Institute Paul-Emile Victor, Institute for Geosciences and Environmental research),

Canada (University of Manitoba) and China (Chinese Academy of Sciences and Beijing Normal University).

Open Research

Data and software availability statement

Radar data, horizontal eigenvalue differences, COF orientations and code are available at (Erda Archive at publication time). Greenland surface velocity data are available at (Joughin et al., 2016). ImpDAR Software used for picking layers in radargrams are available at (Lilien et al., 2020). EastGRIP ice core eigenvalues down to 1714m are available at (Weikusat et al., 2022). Data and code for review can temporarily be found at (`https://sid.erda.dk/sharelink/CNLB42HCab`), and will be permanently archived at publication.

References

Dahl-Jensen, D., Albert, M., Aldahan, A., Azuma, N., Balslev-Clausen, D., Baumgartner, M., ... Zheng, J. (2013, 01). Eemian interglacial reconstructed from a greenland folded ice core. *Nature*, *493*, 489-494. doi: 10.1038/nature11789

Dahl-Jensen, D., Gundestrup, N., Gogineni, S. P., & Miller, H. (2003). Basal melt at north-grip modeled from borehole, ice-core and radio-echo sounder observations. *Annals of Glaciology*, *37*, 207–212. doi: 10.3189/172756403781815492

Dall, J. (2020). Estimation of crystal orientation fabric from airborne polarimetric ice sounding radar data. In *Igarss 2020 - 2020 ieee international geoscience and remote sensing symposium* (p. 2975-2978). doi: 10.1109/IGARSS39084.2020.9323437

Durand, G., Gagliardini, O., Thorsteinsson, T., Svensson, A., Kipfstuhl, S., & Dahl-Jensen, D. (2006). Ice microstructure and fabric: an up-to-date approach for measuring textures. *Journal of Glaciology*, *52*(179), 619–630. doi: 10.3189/172756506781828377

Duval, P., Ashby, M. F., & Anderman, I. (1983). Rate-controlling processes in the creep of polycrystalline ice. *The Journal of Physical Chemistry*, *87*(21), 4066-4074. doi: 10.1021/j100244a014

Ershadi, M. R., Drews, R., Martín, C., Eisen, O., Ritz, C., Corr, H., ... Mulvaney, R. (2022). Polarimetric radar reveals the spatial distribution of ice fabric at domes and divides in east antarctica. *The Cryosphere*, *16*(5), 1719–1739. Retrieved from `https://tc.copernicus.org/articles/16/1719/2022/` doi: 10.5194/tc-16-1719-2022

Franke, S., Bons, P., Westhoff, J., Weikusat, I., Binder, T., Streng, K., ... Jansen, D. (2022, 12). Holocene ice-stream shutdown and drainage basin reconfiguration in northeast greenland. *Nature Geoscience*, *15*, 1-7. doi: 10.1038/s41561-022-01082-2

Fujita, S., Maeno, H., & Matsuoka, K. (2006). Radio-wave depolarization and scattering within ice sheets: a matrix-based model to link radar and ice-core measurements and its application. *Journal of Glaciology*, *52*(178), 407–424. doi: 10.3189/172756506781828548

Fujita, S., Matsuoka, T., Ishida, T., Matsuoka, K., & Mae, S. (2000). A summary of the complex dielectric permittivity of ice in the megahertz range and its applications for radar sounding of polar ice sheets. In *Physics of ice core records* (pp. 185–212).

Gerber, T., Lilien, D., Rathmann, N., Franke, S., Young, T. J., Valero-Delgado, F., ... Eisen, O. (2023). Crystal orientation fabric anisotropy causes directional hardening

of the northeast greenland ice stream. *Nature Communications*, *14*. doi: 10.1038/s41467-023-38139-8

Gerber, T. A., Hvidberg, C. S., Rasmussen, S. O., Franke, S., Sinnl, G., Grinsted, A., ... Dahl-Jensen, D. (2021). Upstream flow effects revealed in the eastgrip ice core using monte carlo inversion of a two-dimensional ice-flow model. *The Cryosphere*, *15*(8), 3655–3679. doi: 10.5194/tc-15-3655-2021

Grinsted, A., Hvidberg, C., Lilien, D., Rathmann, N., Karlsson, N., Gerber, T., ... Dahl-Jensen, D. (2022, 09). Accelerating ice flow at the onset of the northeast greenland ice stream. *Nature Communications*, *13*. doi: 10.1038/s41467-022-32999-2

Hargreaves, N. D. (1977). The polarization of radio signals in the radio echo sounding of ice sheets. *Journal of Physics D: Applied Physics*, *10*(9), 1285. doi: 10.1088/0022-3727/10/9/012

Jacobel, R. W., & Hodge, S. M. (1995). Radar internal layers from the greenland summit. *Geophysical Research Letters*, *22*(5), 587-590. doi: https://doi.org/10.1029/95GL00110

Jansen, D., Franke, S., Bauer, C., Binder, T., Dahl-Jensen, D., Eichler, J., ... Bons, P. (2024, 02). Shear margins in upper half of northeast greenland ice stream were established two millennia ago. *Nature Communications*, *15*. doi: 10.1038/s41467-024-45021-8

Jiracek, G. R. (1967). *Radio sounding of antarctic ice* (Tech. Rep.). Geophysical & Polar Research Center, University of Wisconsin.

Jordan, T. M., Schroeder, D. M., Castelletti, D., Li, J., & Dall, J. (2019). A polarimetric coherence method to determine ice crystal orientation fabric from radar sounding: Application to the neem ice core region. *IEEE Transactions on Geoscience and Remote Sensing*, *57*(11), 8641-8657. doi: 10.1109/TGRS.2019.2921980

Joughin, I., Smith, B., Howat, I., & Scambos, T. (2016). Measures multi-year greenland ice sheet velocity mosaic, version 1. Retrieved from `https://nsidc.org/data/NSIDC-0670/versions/1` doi: 10.5067/QUA5Q9SVMSJG

Joughin, I., Smith, B. E., & Howat, I. M. (2018). A complete map of greenland ice velocity derived from satellite data collected over 20 years. *Journal of Glaciology*, *64*(243), 1–11. doi: 10.1017/jog.2017.73

Li, L. (2021). *Ultrawide-Band Polarimetric Multi-Channel Radar for Measurements of Polar Ice Sheets* (Ph.D. Thesis). The University of Alabama, Electrical engineering.

Li, L., Yan, J.-B., Gogineni, S., O'Neill, C., Dahl-Jensen, D., Simpson, C. D., ... Eisen, O. (2020). Ground-based ultra wideband dual-polarized radar sounding of greenland ice sheets. In *Igarss 2020 - 2020 ieee international geoscience and remote sensing symposium* (p. 1417-1419). doi: 10.1109/IGARSS39084.2020.9323479

Lilien, D., Hills, B., Driscol, J., Jacobel, R., & Christianson, K. (2020, 06). Impdar: an open-source impulse radar processor. *Annals of Glaciology*, *61*, 1-10. doi: 10.1017/aog.2020.44

Martín, C., Gudmundsson, G. H., Pritchard, H. D., & Gagliardini, O. (2009). On the effects of anisotropic rheology on ice flow, internal structure, and the age-depth relationship at ice divides. *Journal of Geophysical Research: Earth Surface*, *114*(F4). doi: https://doi.org/10.1029/2008JF001204

Minchew, B. M., Meyer, C. R., Robel, A. A., Gudmundsson, G. H., & Simons, M. (2018). Processes controlling the downstream evolution of ice rheology in glacier shear margins:

case study on rutford ice stream, west antarctica. *Journal of Glaciology*, *64*(246), 583–594. doi: 10.1017/jog.2018.47

Montagnat, M., Azuma, N., Dahl-Jensen, D., Eichler, J., Fujita, S., Gillet-Chaulet, F., ... Weikusat, I. (2014). Fabric along the neem ice core, greenland, and its comparison with grip and ngrip ice cores. *The Cryosphere*, *8*(4), 1129–1138. doi: 10.5194/tc-8-1129-2014

Paden, J., Li, J., Leuschen, C., Rodriguez-Morales, F., & Hale, R. (2014). *Icebridge mcords l1b geolocated radar echo strength profiles, version 2.* NASA National Snow and Ice Data Center Distributed Active Archive Center. Retrieved from `https://nsidc.org/data/IRMCR1B/versions/2` doi: 10.5067/90S1XZRBAX5N

Picotti, S., Vuan, A., Carcione, J. M., Horgan, H. J., & Anandakrishnan, S. (2015). Anisotropy and crystalline fabric of whillans ice stream (west antarctica) inferred from multicomponent seismic data. *Journal of Geophysical Research: Solid Earth*, *120*(6), 4237-4262. doi: https://doi.org/10.1002/2014JB011591

Rathmann, N. M., & Lilien, D. A. (2022). Inferred basal friction and mass flux affected by crystal-orientation fabrics. *Journal of Glaciology*, *68*(268), 236–252. doi: 10.1017/jog.2021.88

Rathmann, N. M., Lilien, D. A., Grinsted, A., Gerber, T. A., Young, T. J., & Dahl-Jensen, D. (2022). On the limitations of using polarimetric radar sounding to infer the crystal orientation fabric of ice masses. *Geophysical Research Letters*, *49*(1). doi: https://doi.org/10.1029/2021GL096244

Richards, D. H., Pegler, S. S., Piazolo, S., Stoll, N., & Weikusat, I. (2023). Bridging the gap between experimental and natural fabrics: Modeling ice stream fabric evolution and its comparison with ice-core data. *Journal of Geophysical Research: Solid Earth*, *128*(11). doi: https://doi.org/10.1029/2023JB027245

Shepherd, A., Ivins, E., Rignot, E., Smith, B., van den Broeke, M., Velicogna, I., ... Team, I. (2020, MAR). Mass balance of the greenland ice sheet from 1992 to 2018. *NATURE*, *579*(7798), 233+. doi: 10.1038/s41586-019-1855-2

Skolnik, M. (2001). *Introduction to radar systems* (3rd ed.). McGraw-Hill.

Smith, E. C., Baird, A. F., Kendall, J. M., Martín, C., White, R. S., Brisbourne, A. M., & Smith, A. M. (2017). Ice fabric in an antarctic ice stream interpreted from seismic anisotropy. *Geophysical Research Letters*, *44*(8), 3710-3718. doi: https://doi.org/10.1002/2016GL072093

Svensson, A., Durand, G., Mathiesen, J., Persson, A., & Dahl-Jensen, D. (2007, 01). Texture of the upper 1000 m in the grip and northgrip ice cores. In (Vol. 68).

Thorsteinsson, T., Kipfstuhl, J., & Miller, H. (1997). Textures and fabrics in the grip ice core. *Journal of Geophysical Research: Oceans*, *102*(C12), 26583-26599. doi: https://doi.org/10.1029/97JC00161

Weikusat, I., Stoll, N., Kerch, J., Eichler, J., Jansen, D., & Kipfstuhl, S. (2022). *Crystal c-axes (fabric analyser G50) of ice core samples (vertical thin sections) collected from the polar ice core EGRIP, 111-1714 m depth* [data set]. PANGAEA. doi: 10.1594/PANGAEA.949248

Westhoff, J., Stoll, N., Franke, S., Weikusat, I., Bons, P., Kerch, J., ... Dahl-Jensen, D. (2021). A stratigraphy-based method for reconstructing ice core orientation. *Annals of Glaciology*, *62*(85-86), 191–202. doi: 10.1017/aog.2020.76

Zeising, O., Gerber, T., Eisen, O., Ershadi, M., Stoll, N., Weikusat, I., & Humbert, A. (2023,

03). Improved estimation of the bulk ice crystal fabric asymmetry from polarimetric phase co-registration. *The Cryosphere*, *17*, 1097–1105. doi: 10.5194/tc-17-1097-2023

Chapter 6

Polarimetric inversion

In this chapter, I present some unpublished work on formulating the estimation of COF anisotropy as an inverse problem. The chapter should be viewed as a natural continuation of the previous chapters rather than as a self-contained manuscript. The methods presented here have been developed by Niels F. Nymand in collaboration with David A. Lilien (University of Indiana) and Dorthe Dahl-Jensen (University of Copenhagen and University of Manitoba). Data used here was collected by Niels F. Nymand, David A. Lilien, Tamara A. Gerber (University of Copenhagen, now University of Lausanne), Daniel Steinhage (Alfred Wegener Institute) and Dorthe Dahl-Jensen, with technical assistance and input from Drew Taylor and Prasad Gogineni (University of Alabama). This chapter has been written by Niels F. Nymand.

Double reflections and travel-time analysis, as described above, are useful methods because relatively simple radar systems can derive information about the depth-averaged eigenvalue difference and potentially the orientation of the COF. Modern phase-sensitive polarimetric radar systems have been used to develop methods capable of directly tracking the phase difference of co-polarized signals throughout the ice column (Jordan et al., 2019). A different approach to deriving COF information came from Ershadi et al. (2022), where the problem was formulated as an inverse problem, solving for the orientation, eigenvalue difference, and anisotropic scattering coefficient. However, this method relied on the coherence method described in Jordan et al. (2019). For areas like NEGIS, the horizontal anisotropy is so strong that coherence is lost within the first few hundred meters, depending on the frequency and bandwidth (Zeising et al., 2024). In this chapter, I present a different approach to the inverse problem aimed at solving for the anisotropic scattering, orientation, and eigenvalue difference.

The inverse problem

The goal of formulating the task as an inverse problem is to find a set of model parameters, $\mathbf{m}$, that can explain a set of observations, $\mathbf{d}^{obs}$, given a model that can relate the two. This model is called the forward model because it takes a set of model parameters as input and produces a set of observables, $\mathbf{d}$, as output. In general, the forward problem can be expressed as,

$$\mathbf{d} = \mathbf{g}(\mathbf{m}) \tag{6.1}$$

where $\mathbf{g}$ represents the forward model. Most models do not have an inverse, especially when the forward model is a numerical solution to a set of differential equations, but even for simple linear problems, the inverse is often not defined. Even if an inverse exists, real data is subject to random perturbations of the observations due to noise. In most cases, it is more useful to find a set of model parameters that in some way minimize the difference between the real observables, $\mathbf{d}^{obs}$, and the modeled observables. A mathematically convenient way of defining a so-called loss function is with the squared norm of the residual together with a regularization term (Menke, 2018),

$$\mathscr{L}(\mathbf{m}) = \|\mathbf{d}^{obs} - \mathbf{g}(\mathbf{m})\|^2 + \eta^2\|\mathbf{\Gamma m}\|^2. \tag{6.2}$$

where $\mathbf{\Gamma}$ is a regularization matrix and η is a regularization parameter. The idea of the regularization term $\eta^2\|\mathbf{\Gamma m}\|^2$ is to impose on the solution some desired property by penalizing solutions that do not. The property being penalized is described by the product $\mathbf{\Gamma m}$, and η dictates how much this property should be penalized. The choice of η is somewhat subjective, as is the design of $\mathbf{\Gamma}$, and can significantly influence the solution and should therefore be carefully justified.

Radar observables

Following Ershadi et al. (2022), this work uses the co- and cross-polarized azimuthal power anomalies as the observables. The power anomaly at the n$^{\text{th}}$ layer is defined as,

$$\delta^l P_{ij,n}(\gamma) = 20 \log_{10} \left(\frac{|s_{ij,n}(\gamma)|^l}{\frac{1}{\pi} \int_0^\pi |s_{ij,n}(\gamma')|^l d\gamma'} \right), \tag{6.3}$$

where $i, j = \{H, V\}$ and $l = 1$ corresponds to the definition in (Ershadi et al., 2022); however, $l = 2$ will allow an analytical expression of the integral to be easily evaluated for constant $\theta(z)$. $s_{ij,n} = s_{ij}(t_n)$ for $t_n = n\Delta t$ is the discretized return signal. The coherence phase can be expressed as the argument of the coherence,

$$\phi_{HHVV,n}(\gamma) = \arg\big(C_{HHVV,n}(\gamma)\big). \tag{6.4}$$

We will see later that the coherence phase has no real value for inverting the UWB data at NEGIS, but it is included here because it could be useful for other radar surveys.

The power anomalies, $\delta P_{HH,n}(\gamma)$ and $\delta P_{HV,n}(\gamma)$, and phase coherence, $\phi_{HHVV}(\gamma)$, can be calculated directly from the observed radar signals and from the radar model. Because none of these observables depend on the magnitude of the signals, the model operator described in Chapter 4 can be used as the signal matrix,

$$\mathbf{M}_n(\gamma) = \begin{pmatrix} s_{HH,n}(\gamma) & s_{HV,n}(\gamma) \\ s_{VH,n}(\gamma) & s_{VV,n}(\gamma) \end{pmatrix}. \tag{6.5}$$

Radar observables for $\theta(z) = \theta_0$

The Fujita et al. (2006) radar model can be significantly simplified for a constant orientation with depth, which allows for analytical expressions for the HH and HV power anomalies, as well as the coherence phase, to be derived. Whether or not $\theta(z) = \theta_0$ is actually a valid assumption is up for debate, but at least for the part of the EGRIP ice core where the orientation has been reconstructed, there seems to be no evidence of a rotating eigenframe (Westhoff et al., 2021). However, as demonstrated by the synthetic model shown in Ershadi et al. (2022) (Fig. 3), even a small rotation can have a large and somewhat unexpected impact on the return signal.

Assuming $\theta(z) = \theta_0$ the equations in 4.16 can be reduced to (see appendix E),

$$\mathbf{M}_n(\gamma) = D(z_n)^2 \mathbf{R}(\theta_0 - \gamma) \begin{pmatrix} \exp[j\psi_{n,x}] S_{n,x} & 0 \\ 0 & \exp[j\psi_{n,y}] S_{n,y} \end{pmatrix} \mathbf{R}(-\theta_0 + \gamma) \tag{6.6}$$

where $\psi_{n,x} = 2\sum_{i=1}^{n} \Delta z_i (k_{i,x} - k_0)$ and $\psi_{n,y} = 2\sum_{i=1}^{n} \Delta z_i (k_{i,y} - k_0)$, are the phases of $s_{HH,n}(\gamma = \theta_0)$ and $s_{VV,n}(\gamma = \theta_0)$, respectively. The full polarimetric signal can then be

written as,

$$\begin{aligned} s_{HH,n}(\gamma) &= \cos^2(\theta_0-\gamma)s_{HH,n}(\theta_0) + \sin^2(\theta_0-\gamma)s_{VV,n}(\theta_0) \\ s_{VV,n}(\gamma) &= \cos^2(\theta_0-\gamma)s_{VV,n}(\theta_0) + \sin^2(\theta_0-\gamma)s_{HH,n}(\theta_0) \\ s_{HV,n}(\gamma) &= s_{VH,n}(\gamma) = \left[s_{HH,n}(\theta_0) - s_{VV,n}(\theta_0)\right]\cos(\theta_0-\gamma)\sin(\theta_0-\gamma) \end{aligned} \tag{6.7}$$

where $s_{HH,n}(\theta_0) = D(z_n)^2\exp[j\psi_{n,x}]S_{n,x}$ and $s_{VV,n}(\theta_0) = D(z_n)^2\exp[j\psi_{n,y}]S_{n,y}$, are the COF aligned HH and VV signals. From these equations analytical expressions for $\delta P^2_{HH}(\gamma), \delta P^2_{HV}(\gamma)$ and $\phi_{HHVV,n}$, can be derived. In the following, the scattering ratio, $r_n = S_{n,y}/S_{n,x}$, adopted from Ershadi et al. (2022), is used, and $\psi_{n,x}$ and $\psi_{n,y}$ are assumed real, which is equivalent to assuming zero conductivity, $\sigma_{n,x} = \sigma_{n,y} = 0$. The analytical expressions are as follows,

$$\delta P^2_{HH,n}(\gamma) = 20\log_{10}\left[\frac{\cos^4(\theta_0-\gamma)+r_n^2\sin^4(\theta_0-\gamma)+\frac{1}{2}r_n\sin^2(2[\theta_0-\gamma])\cos(\psi_{n,x}-\psi_{n,y})}{\frac{1}{8}[3+3r_n^2+2r_n\cos(\psi_{n,x}-\psi_{n,y})]}\right], \tag{6.8}$$

$$\delta P^2_{HV,n}(\gamma) = 20\log_{10}\left[8\cos^2(\theta_0-\gamma)\sin^2(\theta_0-\gamma)\right], \tag{6.9}$$

$$\phi_{HHVV,n}(\gamma) = \arctan\left[\frac{r_n\sin(\psi_{n,x}-\psi_{n,y})\left(1-\tan^4(\theta_0-\gamma)\right)}{r_n\cos(\psi_{n,x}-\psi_{n,y})\left(1+\tan^4(\theta_0-\gamma)\right)+\tan^2(\theta_0-\gamma)\left(1+r_n^2\right)}\right] \tag{6.10}$$

The full derivations of these expressions can be found in appendix E. One obvious takeaway from the expressions in equations 6.8-6.10 is a high degree of non-linearity with respect to the eigenvalues, which are embedded in $\psi_{n,x}$ and $\psi_{n,y}$. One of the biggest issues is that $\psi_{n,x}$ and $\psi_{n,y}$ depend on the eigenvalues for all layers $i \leq n$.

The observables also have a non-linear relationship with the scattering ratio, but unlike the eigenvalues, $\delta P^2_{HH,n}(\gamma)$ and $\phi_{HHVV,n}(\gamma)$ do not depend on r_i for $i \neq n$. The impact of r_n on $\delta P^2_{HH,n}(\gamma)$ is quite significant because it controls the periodicity of the signal. For $r_n = 1$, the azimuthal periodicity of co-polarized power anomaly is $\frac{\pi}{2}$, as $\delta P^2_{HH,n}(\theta_0) = \delta P^2_{HH,n}(\theta_0 \pm m\frac{\pi}{2})$, where $m \in \mathbb{Z}$. For any $r_n \neq 1$ the periodicity changes to π, as $\delta P^2_{HH,n}(\theta_0) = \delta P^2_{HH,n}(\theta_0 \pm m\pi)$. In Gerber et al. (2024), they use this to derive the scattering and orientation by fitting the amplitude and phase of a sine wave to the HH power anomaly at different depths.

The orientation θ_0 represents a translation in the azimuth of the observables, suggesting it is a well-behaved parameter and the only parameter that the HV power anomaly depends on. In total, the equations 6.8-6.10 constitute the forward model and have $2N+1$ parameters, where N is the number of layers in the model.

Iterative linearisation

We have already established that the inverse problem in non-linear, however, it might be valid to assume that some model parameters are weakly non-linear, in which case a first-order Taylor expansion of the forward model around some initial guess, $\mathbf{m}_0$, might prove a reasonable approximation. The first-order Taylor expansion of the general forward

problem is,

$$\mathbf{g}(\mathbf{m}) \approx \mathbf{g}(\mathbf{m}_0) + \boldsymbol{\nabla}\mathbf{g}(\mathbf{m}_0)\Delta\mathbf{m} \quad \text{for: } \big(\boldsymbol{\nabla}\mathbf{g}(\mathbf{m}_0)\big)_{ij} = \frac{\partial \mathbf{g}_i(\mathbf{m}_0)}{\partial m_j} \tag{6.11}$$

where $\Delta\mathbf{m} = \mathbf{m} - \mathbf{m}_0$. Because the problem is now linear the loss function defined in equation 6.2 can be written as a matrix equation, and the least squares formulation has a closed-form solution, which can be written as,

$$\boldsymbol{\Delta}\mathbf{m} = \big[\mathbf{G}^T\mathbf{G} + \eta^2\boldsymbol{\Gamma}^T\boldsymbol{\Gamma}\big]^{-1}\mathbf{G}^T\big[\mathbf{d}^{obs} - \mathbf{g}(\mathbf{m}_0)\big], \tag{6.12}$$

where $\mathbf{G}_{ij} = \big(\boldsymbol{\nabla}\mathbf{g}(\mathbf{m}_0)\big)_{ij}$ is the Jacobian matrix of $\mathbf{g}$ evaluated at $\mathbf{m}_0$. The advantage of formulating the problem like this is that we have analytical expressions for the forward model, and the Jacobians can, therefore, also be derived analytically. The Jacobians are included in appendix E. Depending on the non-linearity and initial guess, it might take multiple iterations to converge to a solution to the original forward problem. The strategy is called iterative linearisation (Fichtner, 2021) and is sketched in algorithm 1.

Algorithm 1 Iterative linearisation

1: $\mathbf{m}_0 = [\Delta\lambda_1^{(0)}, \Delta\lambda_2^{(0)}, \ldots, \Delta\lambda_N^{(0)}, r_1^{(0)}, r_2^{(1)}, \ldots, r_N^{(1)}, \theta_0^{(0)}]$ ▷ initial guess
2: $(\mathbf{G}_0)_{ij} = \frac{\partial \mathbf{g}_i(\mathbf{m}_0)}{\partial m_j}$ ▷ Generate Jacobian
3: **for** $k = 1$ to k_{max} **do**
4: $\quad\Delta\mathbf{m}_k = \big[\mathbf{G}_{k-1}^T\mathbf{G}_{k-1} + \eta^2\boldsymbol{\Gamma}^T\boldsymbol{\Gamma}\big]^{-1}\mathbf{G}_{k-1}^T\big[\mathbf{d}^{obs} - \mathbf{g}(\mathbf{m}_{k-1})\big]$
5: $\quad\mathbf{m}_k = \mathbf{m}_{k-1} + \alpha\Delta\mathbf{m}_k$ ▷ Update model
6: $\quad a = 1$
7: $\quad$**while** $\mathcal{L}(\mathbf{m}_{k-1}) \leq \mathcal{L}(\mathbf{m}_k)$ **do** ▷ Unsuccessful update
8: $\quad\quad\mathbf{m}_k = \mathbf{m}_{k-1} + \big(\frac{1}{2}\big)^a \alpha\Delta\mathbf{m}_k$ ▷ Reduce step size
9: $\quad\quad a = a + 1$
10: $\quad\quad$**if** $\big(\frac{1}{2}\big)^a \alpha > 10^{-5}$ **then** ▷ 1. Termination condition
11: $\quad\quad\quad$**return** $\mathbf{m}_{k-1}$ ▷ Solution found
12: $\quad\quad$**end if**
13: $\quad$**end while**
14: $\quad$**if** $\frac{\mathcal{L}(\mathbf{m}_{k-1}) - \mathcal{L}(\mathbf{m}_k)}{\mathcal{L}(\mathbf{m}_k)} < 10^{-4}$ **then** ▷ 2. Termination condition
15: $\quad\quad$**return** $\mathbf{m}_{k-1}$ ▷ Solution found
16: $\quad$**end if**
17: **end for**

The step size, or how far along the direction $\Delta\mathbf{m}_k$ to go, is controlled by the parameter α. The while loop on lines 7-13 is there to adjust the step size in case $\alpha\Delta\mathbf{m}_k$ actually increases the loss function. It will continue to half the step size until the loss function yields a smaller value than the previous iteration or the step size reaches a threshold, in which case we assume that the previous iteration had converged. The algorithm will also terminate if the change in the loss function is below a predetermined threshold. The termination thresholds on lines 10 and 14 are free to be picked differently, but these

were used for the inversions presented below.

Depending on the level of non-linearity, the initial guess, $\mathbf{m}_0$, can prove to be very important for the success of the method. To explore this further, a synthetic model based on ice core eigenvalues from EastGRIP is designed to test the method under ideal conditions.

Inversion of synthetic EastGRIP model

A simple model, based on ice core data from EastGRIP (Weikusat et al., 2022), is designed to test the inversion algorithm described above. The model presented here is more or less identical to the synthetic model presented in Gerber et al. (2024), and the details are therefore left out here. δP^2_{HH}, panel (a) in Figure 6.1, is greatly influenced by the scattering ratio, but the birefringence is clearly visible from the co-polarization nodes (Fujita et al., 2006). δP^2_{HV} is of course only influenced by θ_0 with a azimuthal periodicity of 90°. ϕ_{HHVV}, panel (b), is strongly influenced by $\Delta\lambda$, but the angular width of the nodes is influenced by the scattering ratio and decreases for any $r \neq 1$ (Ershadi et al., 2022). In principle, the model parameters could be determined, perhaps ambiguously, from either ϕ_{HHVV} or δP^2_{HH}. In reality, it may prove difficult to let the two observables influence every parameter right away as the non-linearity of the observables could pull the model parameters in opposite directions. It might, therefore, be advantageous if

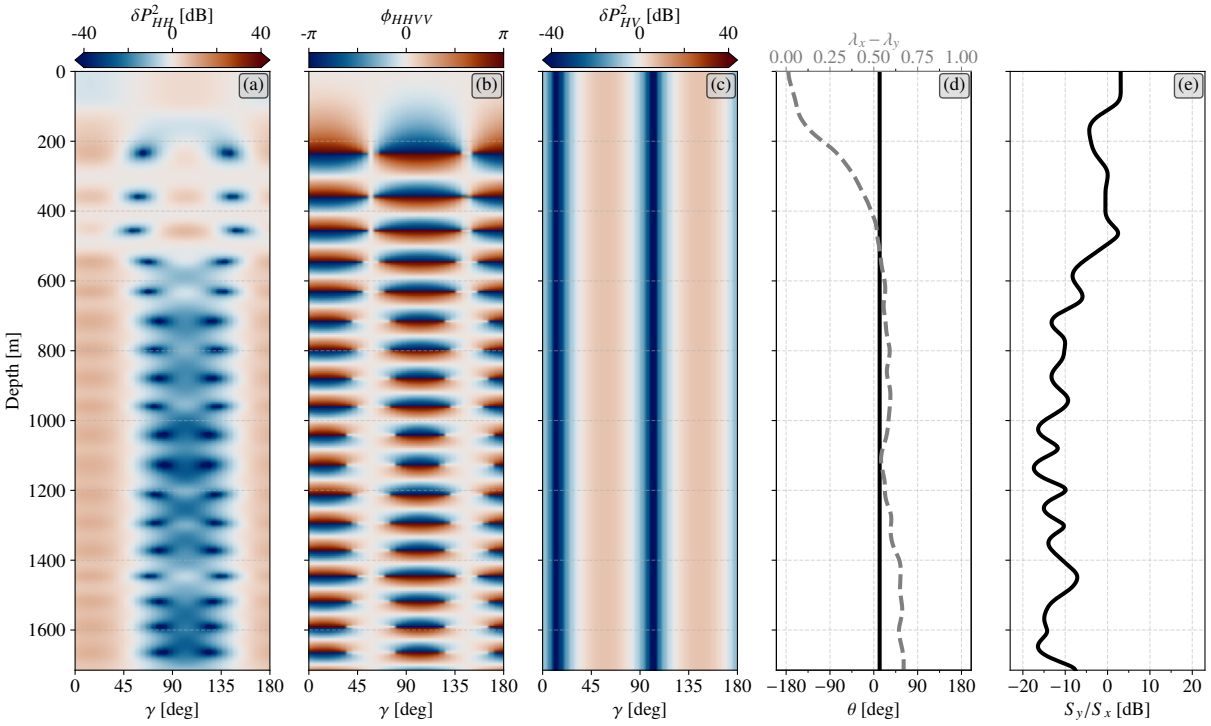

Figure 6.1: Synthetic model based on ice core data from EGRIP (Weikusat et al., 2022). θ_0 is set to 12°. See (Gerber et al., 2024) for more details on how the scattering ratio was derived. Vertical spacing is 5 m, and azimuthal spacing is 5 degrees.

the scattering ratio and orientation can be inverted for without having any information about the eigenvalue difference. Figure 6.2 is an attempt at doing exactly this. The eigenvalue difference is kept constant at $\Delta\lambda(z) = 0.0$ throughout the inversion, and as initial guesses the scattering ratio is $r^{(0)}(z) = 1$, and the initial guess for the orientation is $\theta_0^{(0)} = -20°$. The observables used in the inversion are $\delta P^2_{HH}(\gamma)$ and $\delta P^2_{HV}(\gamma)$ with equal weight. $\delta P^2_{HH}(\gamma)$ influences both the scattering ratio and orientation, and $\delta P^2_{HV}(\gamma)$ only influences the orientation. It is evident from figure 6.2 that the method does quite well at inverting for θ_0, and does a reasonable job at inverting $r(z)$. The inverted $r(z)$, black solid line in figure 6.2, suffers a bit from overfitting as it attempts to fit the co-polarization nodes as seen in figure 6.1a.

A potential limitation is that if the initial guess for θ_0 is too far from the true value, the inversion will search in the wrong direction and land at a solution that is $\pi/2$ away from the true value, which just corresponds to flipping the eigenvectors. This can, for example, be solved by allowing for $\Delta\lambda$ to be negative or by following Ershadi et al. (2022) and using the sign of the phase gradient at the estimated orientation. In reality, any prior information we may have about the orientation of the two eigenvectors can help inform the initial guess of θ_0.

Note on eigenvalue inversion and loss of coherence

Attempting to use the same method of linearized iterations with $\phi_{HHVV,n}(\gamma)$ to invert for $\Delta\lambda$ yields poor results compared to the scattering ratio and orientation. The forward problem is most likely too non-linear for the linearization to be valid for any realistic initial guess. If the radar signals retain coherence, then the vertical gradient of the coherence phase can be used to derive the eigenvalue difference (Jordan et al., 2019; Ershadi et al., 2022). It might also be advantageous to formulate this as an inverse problem to better incorporate noisy data. For eigenvalue differences at NEGIS, the coherence of HH and VV is lost at relatively shallow depths for the bandwidth and center frequency of the UWB radar. If the coherence is lost, the coherence phase cannot be used to derive the eigenvalue difference. No coherence means that the phases of the HH and VV signals are not interacting. For the UWB data, we can incorporate the loss of coherence into the model when inverting for the scattering ratio and orientation by setting $\Delta\lambda(z) = 0.0$.

Cross-correlation method

Due to the loss of coherence, a different method for deriving the eigenvalue difference is needed, and a method that has been shown to work for the strong anisotropy present at EastGRIP is a cross-correlation method introduced by Zeising et al. (2023). It is a continuation of the simple travel-time difference presented in chapter 4, allowing for the eigenvalue difference as a function of depth to be derived and not just the depth-

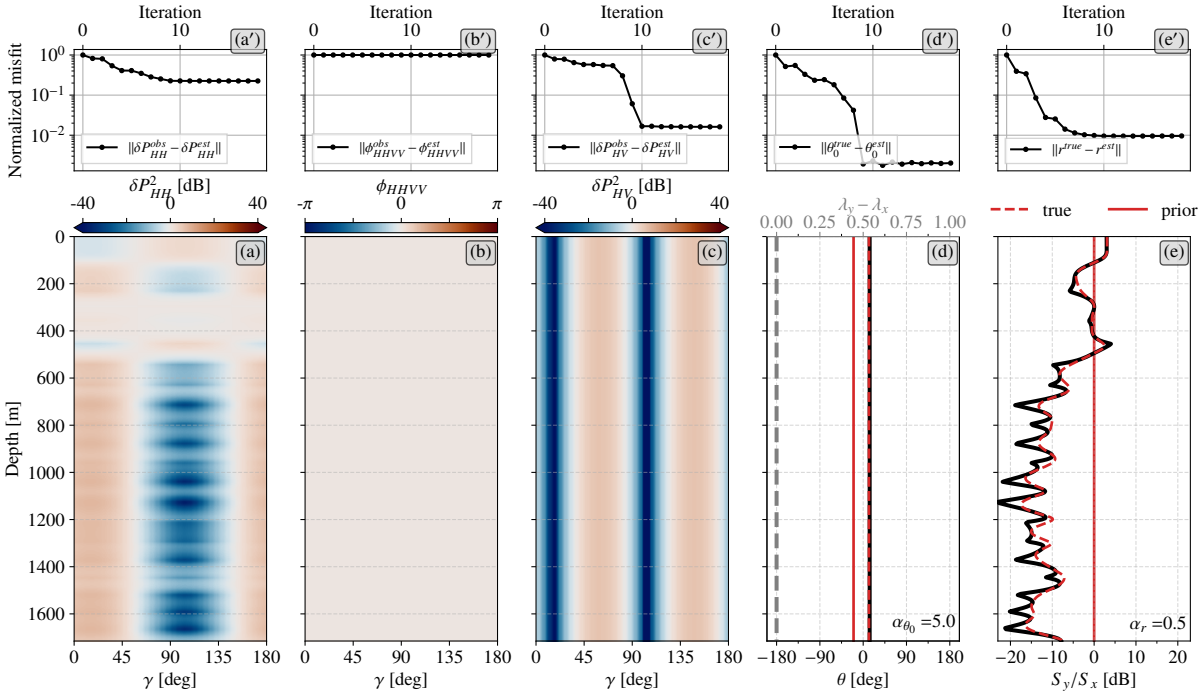

Figure 6.2: Synthetic EGRIP model inverted for scattering ratio and orientation with $\Delta\lambda$ held constant. Top row (a′)-(e′) of figures show misfits as a function of iteration normalized by misfit of initial guess. (a′)-(c′) are the misfits of the observables and (d′)-(e′) are misfits of the inverted model parameters. (a)-(c) show the estimated observables based on the inverted parameters. (d)-(e) show the inverted parameters in black solid lines together with the true and initial guess plotted as dashed red lines and solid red lines, respectively. The regularization term was set to zero. The step lengths are indicated in the bottom right corners of panels (d) and (e).

averaged eigenvalue difference. The basic idea is to cross-correlate segments of a sample length N of the two orthogonal co-polarized signals. The lag between the HH and VV signals that causes the maximum correlation magnitude (normalized like the coherence magnitude) is related to the travel-time difference between the two signals. Doing this over the entire signal range for subsequent segments having a sample overlap of $N_{overlap}$ will give a travel-time difference as a function of depth. The method works very well for stationary systems like the ApRES and could potentially also work for the UWB radar. In the following, I will present a slightly different approach adapted to the UWB data but the same basic idea as presented in (Zeising et al., 2023). The cross-correlation method returns travel-time differences as a function of depth, which can be converted to a depth-averaged eigenvalue difference as a function of depth, $\overline{\Delta\lambda}(z)$. This can be related to the depth-resolved eigenvalue difference, $\Delta\lambda(z)$, as,

$$\overline{\Delta\lambda}(z) = \frac{1}{z_n}\sum_{i=1}^{n}\Delta\lambda(z_i)\Delta z_i, \quad \text{where} \begin{array}{l}\Delta z_i = z_i - z_{i-1}\\ z_0 = 0m\end{array} \tag{6.13}$$

which in turn can be related to the travel-time difference through equation 4.5,

$$\Delta t(z_n) = \frac{\Delta\varepsilon}{c_0\sqrt{\varepsilon_\perp}} \sum_{i=1}^{n} \Delta\lambda(z_i)\Delta z_i \ . \tag{6.14}$$

This can be formulated as a matrix equation and solved as a linear inverse problem. The forward problem can be expressed as,

$$\mathbf{d}^{obs} = \mathbf{G}\mathbf{m} \tag{6.15}$$

$$\mathbf{d}^{obs} = \Big[\Delta t(z_1), \Delta t(z_2), \ldots, \Delta t(z_n), \ldots, \Delta t(z_N)\Big]^T, \tag{6.16}$$

$$\mathbf{m} = \Big[\Delta\lambda(z_1), \Delta\lambda(z_2), \ldots, \Delta\lambda(z_n), \ldots, \Delta\lambda(z_N)\Big]^T, \tag{6.17}$$

$$\mathbf{G} = \frac{\Delta\varepsilon}{c_0\sqrt{\varepsilon_\perp}} \begin{pmatrix} \Delta z_1 & & & & & & \\ \Delta z_1 & \Delta z_2 & & & & & \\ \vdots & & \ddots & & & 0 & \\ \vdots & & & \ddots & & & \\ \Delta z_1 & \Delta z_2 & \Delta z_3 & \cdots & \Delta z_n & & \\ \vdots & & & & & \ddots & \\ \Delta z_1 & \Delta z_2 & \Delta z_3 & \cdots & \Delta z_n & \cdots & \Delta z_N \end{pmatrix}. \tag{6.18}$$

$$\tag{6.19}$$

To solve the inverse problem, the following loss function is used,

$$\mathscr{L}(\mathbf{m}) = \Big[\mathbf{d}^{obs} - \mathbf{G}\mathbf{m}\Big]^T \mathbf{C}_d^{-1} \Big[\mathbf{d}^{obs} - \mathbf{G}\mathbf{m}\Big] + \eta^2 \|\mathbf{\Gamma}\mathbf{m}\|^2 \tag{6.20}$$

where $\mathbf{C}_d$ is a data covariance matrix whose function is to describe the uncertainties in $\mathbf{d}^{obs}$. $\mathbf{C}_d$ is chosen to be a diagonal matrix, where the elements are the squared inverse correlation magnitudes. The idea is that a large correlation magnitude gives high confidence in the estimated Δt. A least squares solution for the loss function in equation 6.20 can be written as (Menke, 2018),

$$\mathbf{m} = \Big[\mathbf{G}^T\mathbf{C}_d^{-1}\mathbf{G} + \eta^2\mathbf{\Gamma}^T\mathbf{\Gamma}\Big]^{-1}\mathbf{G}^T\mathbf{C}_d^{-1}\mathbf{d}^{obs}. \tag{6.21}$$

Unlike the linearized inversions of the scattering ratio and θ_0, the regularization matrix and parameter can not be set to zero. The issue is that a relatively small error in the estimated Δt can lead to a nonphysical $\Delta\lambda$. The way the problem has been framed, the estimated eigenvalue difference, $\Delta\lambda(z_n)$, is actually the mean eigenvalue differences in the depth interval determined by Δz_n. For this reason, the solution is expected to have a certain level of smoothness, which can be expressed as the solution having a small

gradient magnitude. To achieve this, the regularization matrix is written as,

$$\mathbf{\Gamma} = \begin{pmatrix} \frac{-1}{\Delta z_2} & \frac{1}{\Delta z_2} & & \\ & \frac{-1}{\Delta z_3} & \frac{1}{\Delta z_3} & 0 \\ & & \ddots & \ddots \\ & 0 & & \frac{-1}{\Delta z_N} \quad \frac{1}{\Delta z_N} \end{pmatrix} \Rightarrow \mathbf{\Gamma m} = \begin{pmatrix} \frac{\Delta\lambda(z_2)-\Delta\lambda(z_1)}{\Delta z_2} \\ \frac{\Delta\lambda(z_3)-\Delta\lambda(z_2)}{\Delta z_3} \\ \vdots \\ \frac{\Delta\lambda(z_N)-\Delta\lambda(z_{N-1})}{\Delta z_N} \end{pmatrix}. \tag{6.22}$$

The regularization parameter, η, has to be large enough to enforce a "reasonable" solution without dominating the result. If we think of the observable as a sum of a pure signal and a noisy component, i.e., $\mathbf{d}^{obs} = \mathbf{d}^{pure} + \mathbf{n}$, then the goal of the inversion should be to let the noise influence the solution as little as possible. In other words, the objective is to find the η that satisfies $\|\mathbf{d}^{obs} - \mathbf{Gm}\|^2 \approx \|\mathbf{n}\|^2$. While it is impossible to determine $\mathbf{n}$, it might be possible to estimate $\|\mathbf{n}\|$. The accuracy of the travel-time difference is limited by the range resolution of the radar, and any travel-time estimate must therefore have a minimum uncertainty of $\pm\frac{1}{2B}$, where B is the bandwidth of the radar and $\frac{1}{2B}$ is half the range resolution converted to two-way travel time. A simple line search over a wide range of η is performed to find the η that satisfies,

$$\|\mathbf{d}^{obs} - \mathbf{Gm}\|^2 \approx N\left(\frac{1}{2B}\right)^2. \tag{6.23}$$

The advantage of describing the cross-correlation as an inverse problem is the robustness towards noisy data. Specifically, the phase information might not be well preserved after coherent and incoherent integration due to sloping layers and rough surface conditions. The method in Zeising et al. (2023) uses the minimum coherence phase to accurately track the correlation lag as a function of depth, which was not found feasible for the UWB data in their current state. The ApRES systems have the advantage of being able to record while transmitting, making it possible to get layers all the way to the surface where the lag must be zero, giving a tracking algorithm a fixed starting point independent of fabric.

Results

The azimuthal response for the data is synthesized from the HH, VV, HV and VH data by a rotation of the signal matrix. Any azimuth γ of the observed signal is calculated as,

$$\begin{pmatrix} s^{obs}_{HH,n}(\gamma) & s^{obs}_{HV,n}(\gamma) \\ s^{obs}_{VH,n}(\gamma) & s^{obs}_{VV,n}(\gamma) \end{pmatrix} = \mathbf{R}(\gamma) \begin{pmatrix} s^{obs}_{HH,n} & \frac{1}{2}(s^{obs}_{HV,n} + s^{obs}_{VH,n}) \\ \frac{1}{2}(s^{obs}_{HV,n} + s^{obs}_{VH,n}) & s^{obs}_{VV,n} \end{pmatrix} \mathbf{R}(-\gamma), \tag{6.24}$$

where $s^{obs}_{HH,n}$, $s^{obs}_{VV,n}$, $s^{obs}_{HV,n}$ and $s^{obs}_{VH,n}$ are the observed HH, VV, HV and VH data. It is assumed that HV and VH are identical. This has been shown to accurately reconstruct

any azimuth from only these four signals; see Ershadi et al. (2022) and Gerber et al. (2024) for the UWB data.

A slight modification to the forward calculation of δP^2_{HV} has been made to include the effect of noise. The model predicts zero return when aligned with either eigenvector, creating a singularity in the current definition (see equation 6.9). This will undoubtedly cause issues for the inversion. The real minimum of δP^2_{HV} is determined by the noise which has been parameterized as,

$$\delta P^2_{HV,n}(\gamma) = 20 \log_{10} \left[8 \cos^2(\theta_0 - \gamma) \sin^2(\theta_0 - \gamma) + n_{HV} \right], \tag{6.25}$$

where n_{HV} is the cross-polarized noise magnitude. n_{HV} is defined as the minimum of the observed δP^2_{HV}. This will also affect the Jacobian, but as n_{HV} does not depend on θ_0 it is a trivial modification and not shown here.

The inversion results are carried out in two rounds: first, the linearized iterations to invert for the scattering ratios and orientation, r and θ_0, and second, the cross-correlation method to invert for the eigenvalue difference $\Delta\lambda$. Figure 6.3 shows the inversion of r and θ_0 at a location about 10 km upstream from EastGRIP. At this location, the radar was stationary, resulting in a relatively high mean coherence[1]. Iterations are terminated once the second termination condition is met, see Algorithm 1. The inverted scattering ratio shows a high degree of anisotropic scattering throughout most of the ice column. Large fluctuations in the scattering ratio is found at most depths, and most prominently at the basal reflection at around 2.8 km. These local maxima are not necessarily related to anisotropic scattering but rather to bright layers affected by a travel-time difference, which will be discussed further later. The orientation is estimated to be $\theta_0 = -4.2°$. This orientation is in the reference system of the antennas, i.e., the rotation you would have to apply to the antennas to be aligned with the COF eigenvectors.

Figure 6.4 shows the cross-correlation method applied to the same location as the results in figure 6.3. Because the UWB radar records 8 channels, the method is applied to all individual channels, as well as a combined channel, to obtain some additional statistics. The length of the segments used for the cross-correlation is $N = 151$, and subsequent segments overlap by $N_{overlap} = 145$. Any channel, where the regularization parameter η, determined from equation 6.23, lies outside the predetermined search range, or where the inverted eigenvalue differences are not within [0,1], is discarded. Figure 6.4 shows only the results from one channel. Figure 6.5 shows the full inversion result with the eigenvalue differences calculated as a channel mean and compared to the published EastGRIP ice core data (Weikusat et al., 2022). The observation point is located 10 km upstream from the ice core. The inverted eigenvalue differences show a steady increase up to a depth of approximately 2 km with a maximum difference of 0.64 ± 0.03, followed

[1] The COF aligned coherence of HH and VV is still zero, but at orientations not aligned with the COF they are similar due to double reflections. If the coherence is close to zero for all azimuth, it indicates that the radar is only recording noise

by a decrease until the base of the ice at approximately 2.8 km with a minimum difference of around 0.05 ± 0.05.

Figure 6.6 shows inversion results for four different locations: 1) 1.6 km, 2) 10 km, 3) 20 km, and 4) 30 km upstream from EastGRIP. Side by side are the eigenvalue differences, scattering ratio, and mean coherence. The radar was more or less stationary in the locations, which significantly improved the mean coherence. The location closest to EastGRIP was a short stop and, therefore, fewer traces to integrate, which partly explains the relatively low coherence. Locations 1 and 2 in Figure 6.6 both show a steep decline in the eigenvalue difference from 2000-2250 m and down to the base, with location 2 almost reaching zero at the base. Both also show a transition from a reflection ratio of around -7.5 dB to -15 dB at a depth of around 1250 m, and in both cases, this is accompanied by an increase in coherence. Locations 3 and 4 both show an eigenvalue difference characterized by a smaller variation and a minimum eigenvalue difference above 0.25 close to the base. At the four locations, the orientation is calculated relative to the local surface flow vector, θ_0^{flow}. A positive θ_0^{flow} means that the COF eigenvector located at θ_0 (as seen by the antennas H pol), is rotated counter-clockwise by an angle θ_0^{flow} relative to the surface flow vector given by (Joughin & University Of Washington, 2016). The θ_0^{flow} presented is the orientation of the slow axis, i.e., the horizontal axis with the highest concentration of c-axes. A θ_0^{flow} that is a multiple of $\pm\pi/2$ indicates a flow-aligned eigenframe of the COF.

Discussion

Orientation and scattering ratio

A first-order Taylor expansion of the forward models for the co- and cross-polarized power anomalies provides an efficient method for estimating the orientation, θ_0, and scattering ratio, r. The forward model assumes that there is no change in orientation with depth, which is partially supported by a fairly constant cross-polarized power anomaly with depth. However, close to EastGRIP the cross-polarized power anomaly exhibits a sudden rotation at around 1200 m depth, see Figure 6.7. It is unclear what causes this sudden rotation, as it seems unlikely to be an abrupt rotation in the COF eigenframe of more than 30°. Such a rotation would imply a decoupling of the two ice masses above and below this transition, suggesting that the younger ice would be less aligned with the present-day flow. The coherence suggests that the signal above 1200 m is not necessarily informed by the fabric. The co-polarized power anomaly also does not suggest a changing orientation. Additionally, around 8.5 km further upstream, this rotation of the cross-polarized power anomaly is not observed. Figure 6.6 shows an increasing misalignment with the flow as the distance to EastGRIP decreases. The orientation of the antennas are calculated from two GPS receivers located on the port and starboard side of the antenna panels, see figure 3.1. At location 4, approximately

30 km upstream from EastGRIP, the COF is almost aligned with the flow, with only a difference of about 2°. At location 1 the COF is rotated more than 10° relative to flow, which aligns very well with the findings of the double reflections that predicts an eigenframe rotation of approximately $12 \pm 5°$ near EastGRIP, as well as the scattering orientations (Gerber et al., 2024). The uncertainties stated in Figure 6.6 are based only on the uncertainty in surface velocity (Joughin & University Of Washington, 2016) and do not reflect method uncertainty or GPS uncertainty.

The inverted scattering ratio, for the eigenvalue difference set to zero, is able to almost perfectly explain the recorded co-polarized power anomaly (see Figure 6.3), suggesting that birefringence nodes are not contributing, or at least not significantly, to the data. As was also shown by Gerber et al. (2024), the anisotropic scattering is by far the dominant signal in the co-polarized power anomaly. However, the model predicts some clearly visible birefringence nodes (see Figure 6.5), which we do not see in the data. This is due to the loss of coherence, which justifies inverting for the scattering ratio with zero eigenvalue difference. In areas of weaker anisotropy where coherence is preserved, the inversion of the scattering ratio should be run again after estimating the eigenvalue difference, to avoid to issue of overfitting as seen in Figure 6.2.

In Zeising et al. (2024), they discuss how it might be possible to recover coherence by reducing the bandwidth, thereby increasing the width of the pulse-compressed pulses in the processing stage, which also effectively lowers the center frequency. Following Zeising et al. (2024), a bandwidth of around 12 MHz would enable the coherence method to be used for 2.5 km of ice assuming an average eigenvalue difference of 0.5. While it is worth experimenting with, a 12 MHz bandwidth would only utilize 4% of the received pulse, potentially reducing signal-to-noise below a usable level.

At locations with strong reflectors, for example, the bed (around 2.8 km depth in Figure 6.3 and 6.5), the scattering ratio increases significantly. This is not because the bed exhibits anisotropic scattering, but rather an artifact of the bed reflector arriving at different travel times for HH and VV in the COF aligned case. The results are plotted on a depth scale, but it is not a true depth scale, because in order to get a true depth scale the traces would have to be migrated based on the eigenvalue differences. So, at a location with a strong reflector, its apparent position in depth will not be the same at $\gamma = \theta_0$, as for $\gamma = \theta_0 + \pi/2$ due to the travel-time difference. Because the radar model is in depth, and not travel time, this effect is not accounted for. However, the general backscatter, not originating from bright reflectors, do convincingly show anisotropy. The magnitudes align very well with Gerber et al. (2024).

Eigenvalue differences

The cross-correlation method, adapted from Zeising et al. (2023), does a seemingly good job at reconstructing the eigenvalue difference as a function of depth. At all four locations in Figure 6.6, the eigenvalue differences show a similar pattern: Steadily

increasing from 1000 m towards a maximum between 1500 m - 2000 m, followed by a decrease towards the bed. The locations closest to EastGRIP both have estimated eigenvalue differences below 0.2 near the base, with the second location, Figure 6.6a$_2$, reaching values as low as 0.05. This matches well with the eigenvalues derived from the ice core (Stoll et al., 2024), where the fabric changes from a vertical girdle with a horizontal maximum to a fabric with a higher degree of randomness at around 2500 m due to migrational recrystallization. Further upstream (locations 3 and 4), the eigenvalue differences never get below 0.3, suggesting slightly different conditions near the base, perhaps lower temperatures reducing the degree of recrystallization.

The two locations closest to EastGRIP are compared to the published ice core eigenvalues (Weikusat et al., 2022), see Figures 6.5 and 6.7. While neither of the two locations are directly over the EastGRIP ice core, they do lie on the same flow line, with the closest being only 1.6 km away, or about 30 years, assuming annual flow at around 55 m/yr (Hvidberg et al., 2020). The estimated eigenvalue differences presented here are consistently underestimated compared to the ice-core-derived ones. This could be explained by too aggressive regularization, which flattens the curve more than necessary. They do, however, match the ice core better where the curves start to flatten, which might suggest that the gradient is not the optimal attribute to minimize when inverting for the eigenvalue differences.

The eigenvalue differences estimated from the cross-correlation derived travel-time differences enforce smooth solutions through regularization. The travel-time differences depend on the average eigenvalue differences, which means the depth-resolved eigenvalue differences are poorly constrained. This makes regularization necessary to find well-behaved solutions. The ice core has a relatively large variation in the horizontal eigenvalue difference and is believed to be the cause of the anisotropic scattering (Gerber et al., 2024). The inverted scattering ratio might, therefore, provide a means of reconstructing the non-smooth component of the eigenvalue differences. In Ershadi et al. (2022), they were able to reconstruct all three eigenvalues from the scattering ratio and eigenvalue difference; however, this was only possible because they had data starting at the surface where, where they assumed isotropic ice. Careful consideration of applicable assumptions would be needed to attempt such a reconstruction here, and it is not attempted here.

Method limitations

In order to derive analytical expressions for the co-polarized and cross-polarized power anomalies, the orientation cannot change with depth, making it an inherent assumption for the inverted scattering ratio as well. Previous radar surveys have sometimes used the minimum of the cross-polarized power anomaly to get the orientation of the two horizontal eigenvectors as a function of depth (J. Li et al., 2018; T. J. Young et al., 2021; Ershadi et al., 2022), or assumed a constant orientation and used the coherence

phase gradient transition zones between positive and negative (Jordan et al., 2019, 2020). Following the Fujita radar model (Fujita et al., 2006), using the cross-polarized power minima as eigenvector orientations is only valid if the orientation is constant with depth, also demonstrated by (Ershadi et al., 2022). The somewhat chaotic behavior of the return signal for changing orientations with depth in the radar model might not be the case when coherence is lost, as the phase of the two waves no longer interact. However, it is not immediately obvious how one should go about reliably estimating a changing eigenframe with depth. The inverted orientation presented here is the constant orientation with depth that best represents the co- and cross-polarized power anomalies. In the same way the orientations derived from the double reflections are the orientations that best explain the relative amplitudes of the two reflections. For stationary data collection, the cross-correlation method, as implemented here, gives consistent estimates of the travel-time lags between all eight radar channels. However, the method is more hit-and-miss at locations where the radar is moving. To achieve a better correlation, allowing for subsample travel-time lags when computing the cross-correlation could improve this.

Conclusion

We have presented a method for efficiently estimating the anisotropic scattering, parameterized as a scattering ratio, and orientation of the COF eigenvectors by formulating it as a non-linear inverse problem and solving it with linearized iterations. Analytical expressions of the observables, co- and cross-polarized power anomalies, and coherence phase, for a layered medium were derived from the Fujita radar model (Fujita et al., 2006), by assuming a constant orientation with depth. This allows for fast evaluation of the forward model and estimation of the Jacobians needed for the linearization of the forward model. The inversion of the scattering ratio and orientation was first tested on a synthetic model based on published EastGRIP ice core data, where it was demonstrated that information about the eigenvalue differences was not needed to reconstruct reasonable estimates of the scattering ratio and orientation. The eigenvalue differences are not well constrained by the observables, even in the synthetic case, and a different method based on the cross-correlation method from Zeising et al. (2023), was instead employed. The cross-correlation method was formulated as a linear inverse problem subjected to regularization to incorporate uncertainty related to the range resolution of the radar. Applied to real data collected at NEGIS in 2022, it showed that the scattering ratio and orientation estimates are able to accurately reproduce the power anomaly data, suggesting little to no influence of birefringence-induced interference of the co-polarized data, as also shown by Gerber et al. (2024). In fact, this is because the co-polarized coherence is lost at shallow depths due to the exceptionally strong anisotropy at NEGIS.

At four different locations upstream of NEGIS, where the radar was stationary, the cross-correlation method was able to reconstruct the eigenvalue difference as a function of depth with a high degree of confidence, based on the 8 different receiver channels

of the radar showing the same pattern. The method is able to reconstruct the eigenvalue differences from around 1000 m and down to the base of the ice at more than 2500 m. The four locations show similar depth evolutions with a steady increase from 1000 m and down to 1500 m - 2000 m, followed by a decrease towards the base. Compared to the published ice core eigenvalue data from EastGRIP (Weikusat et al., 2022) and previous implementation of the method (Zeising et al., 2023), the cross-correlation method presented here tends to underestimate the eigenvalue differences, especially in regions of non-zero gradients, most likely due to an insufficient regularization condition. The orientation becomes increasingly aligned with the flow as the upstream distance from EastGRIP increases. The orientation of the slow axis changes from 79.6° to 87.8° relative to flow at upstream distances of 1.6 km and 30 km, respectively.

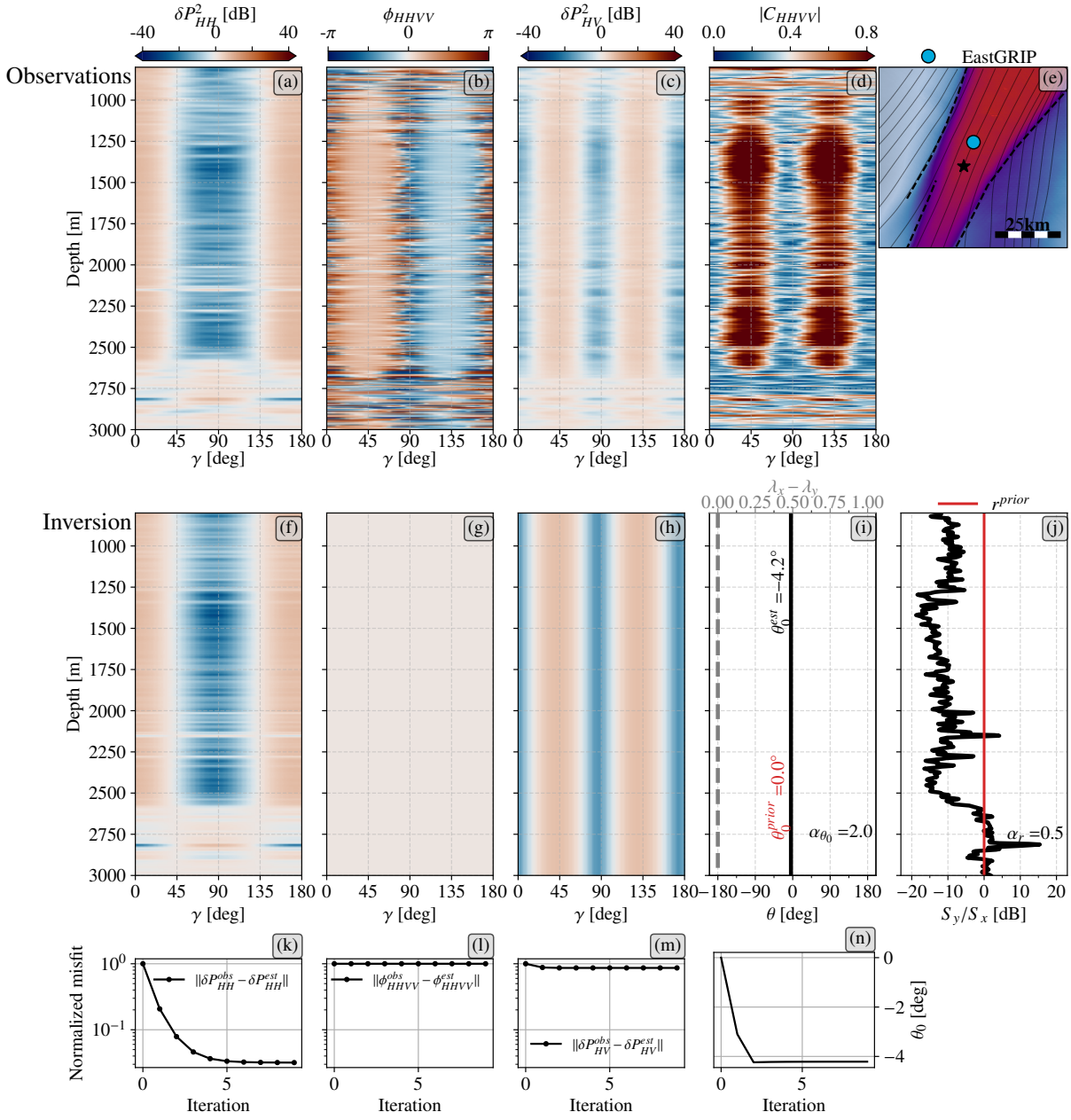

Figure 6.3: Inversion results for scattering ratio r and orientation θ_0 for a fixed $\Delta\lambda$. The top row of panels shows observations (a-d) and (e) show the location of observation, black star, and EastGRIP, blue dot, on a surface velocity map (Joughin & University Of Washington, 2016). Panel (d) is the coherence magnitude, $|C_{HHVV}|$. The observations are located around 10 km upstream from EastGRIP. (f-h) display the estimated observables calculated from the inverted model parameters. (i) show the inverted orientation θ_0^{est} plotted as a solid black line, and the fixed eigenvalue difference is plotted as a dashed gray line. (j) shows the inverted scattering ratio plotted as a solid black line and the prior scattering ratio as a solid red line.

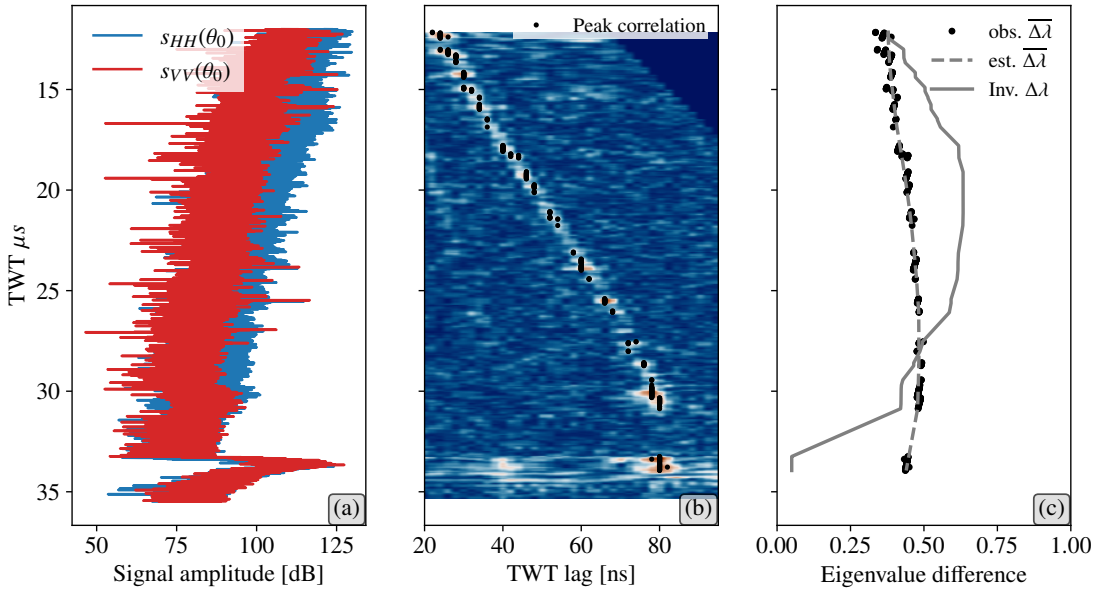

Figure 6.4: Cross-correlation method for channel 1 of the UWB at the same location as indicated in figure 6.3e. Panel (a) show the two traces synthesized to be at the estimated orientation $\theta_0 = -4.2°$. Panel (b) is the cross-correlation of HH and VV trace from panel (a) plotted as a function of depth and TWT lag. The peak correlations are marked with black dots. Panel (c) shows the mean eigenvalue difference estimated from the TWT lag of the peak correlations as black dots and the inverted eigenvalue differences, $\Delta\lambda$, as a solid gray line. The dashed gray line shows the mean eigenvalue differences estimated from the inverted $\Delta\lambda$.

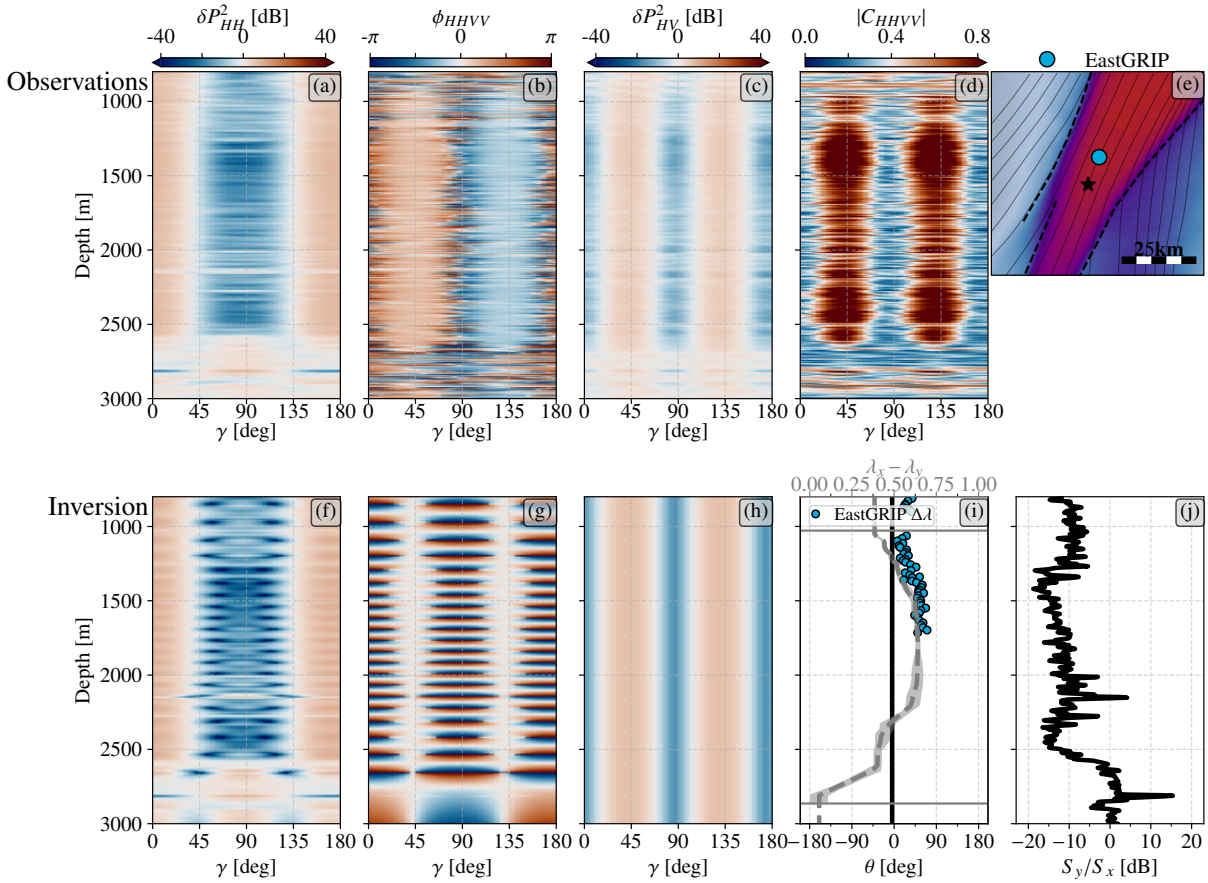

Figure 6.5: Inversion results for scattering ratio r, orientation θ_0 and eigenvalue difference $\Delta\lambda$. The first row of panels is identical to figure 6.3. The second row of panels shows the updated model results with the channel averaged eigenvalue differences estimated using the cross-correlation method, dashed gray line in panel (i). The entire range of inverted eigenvalue differences is shown as solid gray around the mean eigenvalue difference. Gray dots in panel (i) are ice core-derived eigenvalue differences for comparison (Weikusat et al., 2022).

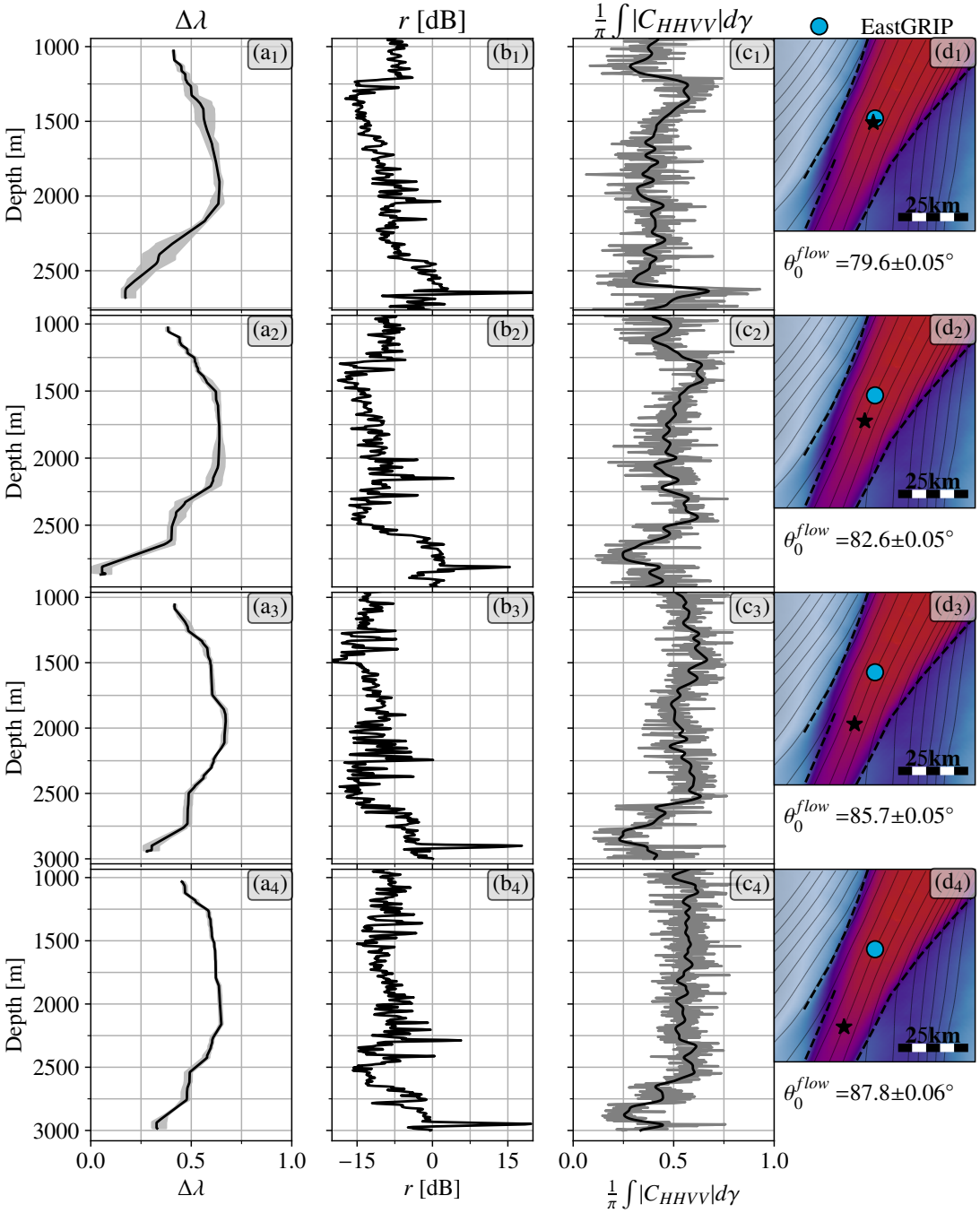

Figure 6.6: Inversion results at four different locations at increasing upstream distance to EGRIP (1.6 km, 10 km, 20 km, 30 km), where the radar was stationary or near stationary for optimal conditions. (a) panels show the channel mean eigenvalue difference in black and channel minimum and maximum in gray. (b) panels show the inverted scattering ratio. (c) panels show the azimuthally averaged coherence. (d) panels show the trace location as a black star, and EastGRIP location as a blue dot, and under is the inverted orientation converted to be relative to the local surface flow vector, θ_0^{flow}, using the surface velocity data from (Joughin & University Of Washington, 2016). The stated uncertainties are derived from the uncertainty in surface velocity.

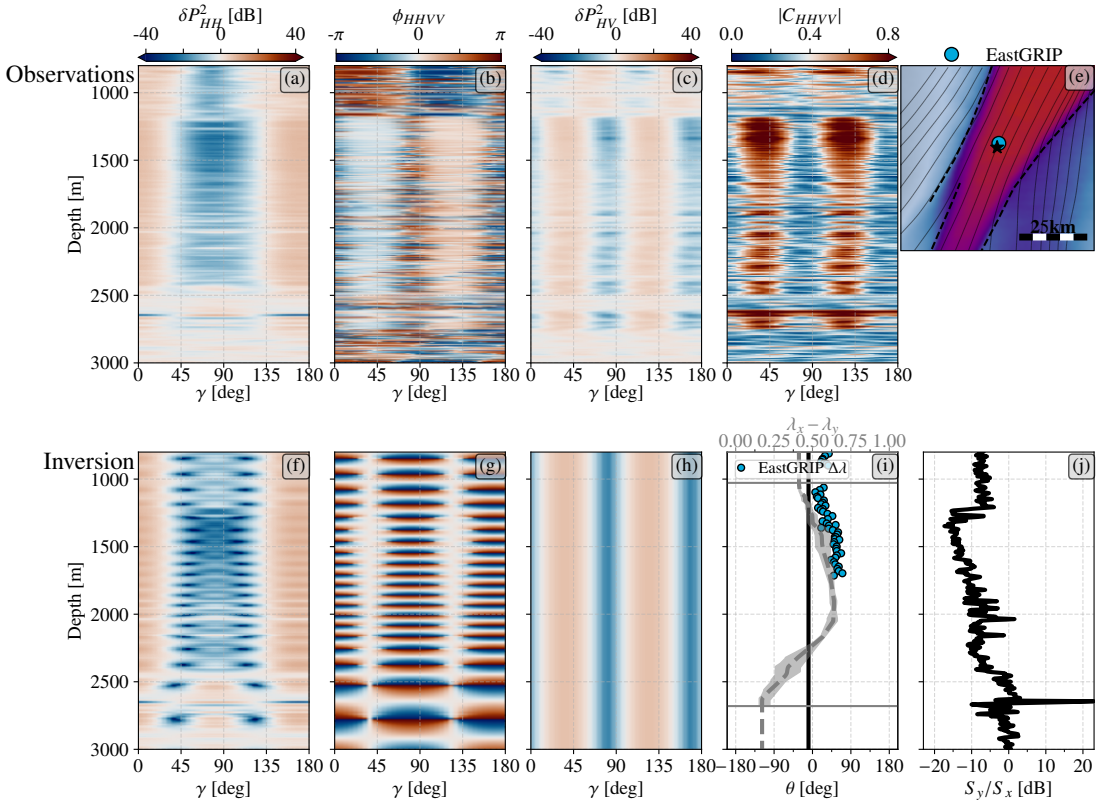

Figure 6.7: The inversion results at the location nearest EastGRIP, where the cross-polarized power anomaly shows a sudden rotation at ≈1200 m depth. The two horizontal gray lines in panel (i) show the extent of the cross-correlation method.

Chapter 7

Co-author publications

Potential to recover a record of Holocene climate and sea ice from Müller Ice Cap, Canada

David Armond Lilien[1], **Niels Fabrin Nymand**[2], Tamara Annina Gerber[2], Daniel Steinhage[3], Daniela Jansen[3], Laura Thomson[4] , Madeline Myers[4], Steven Franke[5], Drew Taylor[6], Prasad Gogineni[6], Marcos Lemes[1], Bo Møllesøe Vinther[2] and Dorthe Dahl-Jensen[1,2]

[1]Centre for Earth Observation Science, University of Manitoba, Winnipeg, MB, Canada

[2]Physics of Ice, Climate, and Earth, University of Copenhagen, Copenhagen, Denmark

[3]Alfred Wegener Institute, Helmholtz Centre for Polar and Marine Research, Bremerhaven, Germany

[4]Department of Geography and Planning, Queen's University, Kingston, ON, Canada

[5]Department of Geosciences, Tübingen University, Tübingen, Germany

[6]Remote Sensing Center, University of Alabama, Tuscaloosa, AL, USA

Abstract

Müller Ice Cap sits on Umingmat Nunaat (Axel Heiberg Island), Nunavut, Canada, ∼80°N. Its high latitude and elevation suggest it experiences relatively little melt and preserves an undisturbed paleoclimate record. Here, we present a suite of field measurements, complemented by remote sensing, that constrain the ice thickness, accumulation rate, temperature, ice-flow velocity, and surface-elevation change of Müller Ice Cap. These measurements show that some areas near the top of the ice cap are more than 600 m thick, have nearly stable surface elevation, and flow slowly, making them good candidates for an ice core. The current mean annual surface temperature is -19.6°C, which combined with modeling of the temperature profile indicates that the ice is frozen to the bed. Modeling of the depth-age scale indicates that Pleistocene ice is likely to exist with measurable resolution (300-1000 yr m^{-1}) 20-90 m from the bed, assuming that Müller Ice Cap survived the Holocene Climatic Optimum with substantial ice thickness (∼400 m or more). These conditions suggest that an undisturbed Holocene climate record could likely be recovered from Müller Ice Cap. We suggest 91.795°W, 79.874°N as the most promising drill site.

Author contribution

I contributed to Lilien et al. (2024) by participating in the planning and execution of the fieldwork at the Müller Ice Cap in Nunavut, Canada. At the ice cap, we conducted a survey with the UWB radar to locate a potential drill site. I processed the radar data in the field and contributed to picking the most promising drill site. At the chosen site, I assisted in drilling a shallow core used to measure δ^{18}O to estimate accumulation at the site. After the fieldwork, I helped trace the bedrock reflections from the AWI airborne radar data and worked on implementing a simple range-Doppler algorithm to better focus the basal reflector in the UWB data, ultimately providing a more accurate measurement of the depth at the chosen drill site. I read and commented on the final manuscript.

Anisotropic Scattering in Radio-Echo Sounding: Insights from Northeast Greenland

Tamara Annina Gerber[1], David A. Lilien[2,3], **Niels F. Nymand**[1], Daniel Steinhage[4], Olaf Eisen[4,5], and Dorthe Dahl-Jensen[1,2]

[1]Section for the Physics of Ice, Climate and Earth, University of Copenhagen, Copenhagen, Denmark.

[2]Centre for Earth Observation Science, University of Manitoba, Winnipeg, MB, Canada.

[3]Department of Earth and Atmospheric Sciences, Indiana University, Bloomington, IN, USA

[4]Alfred Wegener Institute Helmholtz Centre for Polar and Marine Research, Bremerhaven, Germany

[5]Department of Geosciences, University of Bremen, Bremen, Germany

Abstract

Anisotropic scattering and birefringence-induced power extinction are two distinct mechanisms affecting the azimuthal power response in Radio Echo Sounding (RES) of ice sheets. While birefringence is directly related to the crystal orientation fabric (COF), anisotropic scattering can, in principle, have various origins. Although both mechanisms can appear separately, they often act jointly, complicating efforts to deduce the COF strength and orientation from RES signals. In this study, we assess the relative importance of anisotropic scattering and birefringence using quad-polarized ground-based RES measurements collected in the Northeast Greenland Ice Stream (NEGIS). We employ curve-fitting techniques to analyze the synthesized full azimuthal response, revealing insights into the dominance and orientation of the two different mechanisms at various depths between 630 m and 2500 m. We find that anisotropic scattering clearly dominates the radar signal in most depths larger than 1000 m, while birefringence effects are only important at shallower depths and in the vicinity of the ice-stream shear margins. We further find that the co-polarized power difference follows the ice-sheet stratigraphy with a notable transition in strength and/or direction at the Wisconsin-Holocene transition and in folded ice outside the ice stream, possibly indicating inverted stratigraphy in these folded units. We conclude that small-scale fluctuations in the horizontal COF eigenvalues is the most likely mechanism responsible for the anisotropic scattering observed in our survey area. Mapping the strength and orientation of scattering in quad-polarized measurements thus have the potential to provide independent estimates of the COF orientation and distinguish ice units with different scattering properties, e.g. from different climatic periods.

Author contribution

I contributed to Gerber et al. (2024) by participating in the fieldwork and data collection in Greenland in 2022. I processed most of the raw data used for the study and assisted with parts of the analysis. I provided comments and feedback on all sections of the current preprint version of the manuscript.

Chapter 8

Conclusion and outlook

The work presented in this thesis demonstrates how polarized radar data can be used to derive valuable information about the crystal orientation fabric (COF). This work has helped provide new insights into the flow dynamics of the Northeast Greenland Ice Stream (NEGIS).

Because the orientation of ice crystals has the potential to soften and stiffen ice to an applied stress by around two orders of magnitude, it plays an important role in our ability to accurately model the flow of ice. This is especially true for fast-flowing regions, like ice steams, where highly anisotropic COFs are developed by large strains. NEGIS plays an important role in the dynamic mass loss of the Greenland ice sheet, but it is notoriously difficult to model for large-scale ice flow models. This is because NEGIS, unlike other ice streams in Greenland, is not topographically confined by the bedrock. What initiated the ice steam is still debated, and with every new finding, more questions seem to emerge. From the widening and relatively young age of the shear margins (Grinsted et al., 2022; Jansen et al., 2024) to the discovery of an extinct NEGIS type ice stream hundreds of kilometers north of the current ice stream (Franke, Bons, et al., 2022). The work presented in this thesis adds to this growing evidence of an ice stream with a more complicated recent flow history than previously assumed.

In the summer of 2022, we conducted a comprehensive survey of NEGIS with an ultra-wideband polarimetric radar system, the UWB system. Utilizing the data collected here, two studies are presented in this thesis to obtain valuable estimates of the COF.

The first study presents a novel method for deriving the depth-averaged eigenvalue difference and the orientation of the COF by utilizing double reflections. It has long been known that anisotropic COFs will split any incoming polarized wave into two orthogonally polarized components propagating at different phase speeds, a slow and a fast wave. In this study, we show that under certain conditions, these two waves may get separated to a degree where the radar system can resolve two distinct reflections originating from the same physical reflector/layer in the ice. The relative amplitude of the two recorded reflections can be related to the relative angle between the antenna panels of the radar and the horizontal eigenvectors of the COF. This method provides a

way to estimate the eigenvalue differences without needing multiple polarizations. This opens the possibility to go back and look for double reflections in radar data that was not originally intended for estimating COF. For estimating the orientation it is not quite enough with single co-polarized data, as anisotropic scattering and attenuation can affect the relative amplitude, and orthogonally co-polarized or cross-polarized data is needed to account for this. The method applied to the radar data from NEGIS showed evidence that the COF was not completely flow-aligned at the center of the ice stream near EastGRIP and a general asymmetry across the ice stream. It also showed an almost 45-degree rotation of the COF relative to flow near the northwestern shear margin. The results were compared to a fabric development model (Gerber et al., 2023), which was able to reproduce our results of the northwestern part of the ice stream but failed for the center and southeastern part. The model predicts that the COF of the ice stream is more or less symmetric about the center flow line, with a flow-aligned COF at the center. The model assumes that ice flow has remained steady for the last $\sim$ 10 kyr, and we believe that the mismatch between the model and our findings stems from this assumption. This study is another piece of evidence that the flow and shape of NEGIS are more variable than previously assumed.

In the second study, we formulate the problem of deriving the COF from the full polarimetric signal as an inverse problem. Based on the radar model developed by Fujita et al. (2006) we derive analytical expressions for the co-polarized and cross-polarized power anomalies as well as the coherence phase for an arbitrary number of layers, by assuming a constant orientation with depth. With these expressions, a simple inversion algorithm, based on an iterative linearization of the forward model, is set up to inverte for the orientation and anisotropic scattering ratio. Without information about the eigenvalue differences, the inverted scattering ratio and orientation can accurately reproduce co- and cross-polarized power anomalies. Due to the unusually high horizontal anisotropy at NEGIS relative to the bandwidth and center frequency of the radar, the coherence between orthogonal co-polarized signals disappears at polarizations closely aligned with the COF. This means that the coherence phase is not usable for deriving eigenvalue difference as a function of depth, as done by other studies in other glaciological conditions (Jordan et al., 2019; T. J. Young et al., 2021; Ershadi et al., 2022), except for perhaps the very top 100 m of the ice sheet (Zeising et al., 2023). For the eigenvalue difference, the problem was formulated as a linear inverse problem to find the eigenvalue differences that best explain the travel-time differences as a function of depth, derived from the cross-correlation method described in Zeising et al. (2023). The inversion was applied at four different locations upstream of the EastGRIP ice core. Near the ice core, the orientation matches the double reflections' findings, suggesting a COF rotation of more than 10° relative to flow. However, at increasing upstream distance, the COF tends towards being flow aligned, with only a few degrees offset 30 km upstream from EastGRIP. The eigenvalue differences generally showed a gradual increase from around 1000 m to a maximum located between 1500 m - 2000 m, followed by a decrease to-

wards the base. While the estimated eigenvalue differences are generally underestimated compared to the ice-core-derived ones, they show a similar trend, and our estimates are generally consistent with the depth evolution of the eigenvalue differences derived from the ice core (Stoll et al., 2024).

Outlook

Double reflections have the potential to be used for already collected data in Greenland and Antarctica, where thousands of kilometers of flight lines have been collected. Some of these flights cross over areas of high horizontal anisotropy, like ice streams, where the method might be able to give depth-averaged eigenvalue differences, depending on the bandwidth of the radar system.

If the cross-correlation method can be improved to better handle nonstationary data, perhaps through a different processing of the data and/or an improved method of correlation, the polarimetric inversion can be extended to all parts of our 2022 NEGIS survey, providing the most detailed map of COF data ever compiled for NEGIS. Combined with fabric development models, this dataset has the potential to greatly improve our understanding of the flow history of NEGIS. The UWB data contain many more stationary points to provide valuable information, even without using non-stationary locations. If the method is to incorporate a potential change of eigenframe with depth, a modified radar model that can incorporate the loss of coherence is needed.

The UWB data have great potential for further exploration beyond COF analysis. One special area of interest for NEGIS is the basal conditions, and previously, radar surveys have been used to estimate the presence of meltwater at the base (Jacobel et al., 2009; K. Matsuoka et al., 2012; D. A. Young et al., 2016). In the summer of 2023, the base of the ice at EastGRIP was reached, and logging of the borehole again in 2024 suggests no gradient in the horizontal velocity with depth. If the ice is not shearing at EastGRIP, it must be supported by some form of lubrication at the base of the ice. Perhaps the radar reflectivity can help map the extent of block flow at NEGIS.

In the summer of 2025, the UWB radar will be brought back to EastGRIP to get a complete flow line coverage from EastGRIP to the GRIP borehole located at the summit of the Greenland Ice Sheet. A full flow line profile will potentially help better constrain the upstream flow effects of the EastGRIP ice core (Gerber et al., 2021). It can hopefully also shed some light on the exceptionally high basal melt rates that were first suggested by Fahnestock et al. (2001).

Chapter 9

Bibliography

References

Advani, S. G., & Tucker, C. L. (1987, November). The Use of Tensors to Describe and Predict Fiber Orientation in Short Fiber Composites. *Journal of Rheology*, *31*(8), 751–784. Retrieved 2024-10-08, from https://pubs.aip.org/sor/jor/article/31/8/751-784/235499 doi: 10.1122/1.549945

Alley, R. B. (1992). Flow-law hypotheses for ice-sheet modeling. *Journal of Glaciology*, *38*(129), 245–256. Retrieved 2024-10-04, from https://www.cambridge.org/core/product/identifier/S0022143000003658/type/journal_article doi: 10.3189/S0022143000003658

Azuma, N., & Higashi, A. (1985). Formation Processes of Ice Fabric Pattern in Ice Sheets. *Annals of Glaciology*, *6*, 130–134. Retrieved 2024-09-17, from https://www.cambridge.org/core/product/identifier/S0260305500010168/type/journal_article (Publisher: International Glaciological Society) doi: 10.3189/1985aog6-1-130-134

Bamler, R. (1992, July). A comparison of range-Doppler and wavenumber domain SAR focusing algorithms. *IEEE Transactions on Geoscience and Remote Sensing*, *30*(4), 706–713. Retrieved 2024-12-16, from http://ieeexplore.ieee.org/document/158864/ doi: 10.1109/36.158864

Bons, P. D., De Riese, T., Franke, S., Llorens, M.-G., Sachau, T., Stoll, N., ... Zhang, Y. (2021, May). Comment on "Exceptionally high heat flux needed to sustain the Northeast Greenland Ice Stream" by Smith-Johnsen et al. (2020). *The Cryosphere*, *15*(5), 2251–2254. Retrieved 2024-10-14, from https://tc.copernicus.org/articles/15/2251/2021/ doi: 10.5194/tc-15-2251-2021

Brennan, P. V., Lok, L. B., Nicholls, K., & Corr, H. (2014, August). Phase-sensitive FMCW radar system for high-precision Antarctic ice shelf profile monitoring. *IET Radar, Sonar & Navigation*, *8*(7), 776–786. Retrieved 2024-09-12, from https://onlinelibrary.wiley.com/doi/10.1049/iet-rsn.2013.0053 doi: 10.1049/iet-rsn.2013.0053

Buchardt, S. L., & Dahl-Jensen, D. (2008). At what depth is the Eemian layer expected to be found at NEEM? *Annals of Glaciology*, *48*, 100–102. Retrieved 2024-10-17, from https://www.cambridge.org/core/product/identifier/S0260305500251252/type/journal_article doi: 10.3189/172756408784700617

Cuffey, K., & Paterson, W. S. B. (2010). *The physics of glaciers* (4th ed ed.). Burlington, MA: Butterworth-Heinemann/Elsevier. (OCLC: ocn488732494)

Dahl-Jensen, D., Gundestrup, N., Keller, K., Johnsen, S., Gogineni, S., Allen, C., ... Waddington, E. (1997). A search in north Greenland for a new ice-core drill site. *Journal of Glaciology*, *43*(144), 300–306. Retrieved 2024-10-17, from https://www.cambridge.org/core/product/identifier/S0022143000003245/type/journal_article doi: 10.3189/S0022143000003245

Dall, J. (2010, July). Ice sheet anisotropy measured with polarimetric ice sounding radar. In *2010 IEEE International Geoscience and Remote Sensing Symposium* (pp. 2507–2510). Honolulu, HI, USA: IEEE. Retrieved 2024-11-08, from http://ieeexplore.ieee.org/document/5653528/ doi: 10.1109/IGARSS.2010.5653528

Dansgaard, W., Johnsen, S. J., Møller, J., & Langway, C. C. (1969, October). One Thousand Centuries of Climatic Record from Camp Century on the Greenland Ice Sheet. *Science*, *166*(3903), 377–381. Retrieved 2024-10-03, from https://www.science.org/doi/10.1126/science.166.3903.377 doi: 10.1126/science.166.3903.377

Diez, A., Eisen, O., Hofstede, C., Lambrecht, A., Mayer, C., Miller, H., ... Weikusat, I. (2015, February). Seismic wave propagation in anisotropic ice – Part 2: Effects of crystal anisotropy in geophysical data. *The Cryosphere*, *9*(1), 385–398. Retrieved 2024-10-11, from https://tc.copernicus.org/articles/9/385/2015/ doi: 10.5194/tc-9-385-2015

Duval, P., Ashby, M. F., & Anderman, I. (1983, October). Rate-controlling processes in the creep of polycrystalline ice. *The Journal of Physical Chemistry*, *87*(21), 4066–4074. Retrieved 2024-09-17, from https://pubs.acs.org/doi/abs/10.1021/j100244a014 (Publisher: American Chemical Society (ACS)) doi: 10.1021/j100244a014

Ehlers, J., & Gibbard, P. (2011). Quaternary Glaciation. In V. P. Singh, P. Singh, & U. K. Haritashya (Eds.), *Encyclopedia of Snow, Ice and Glaciers* (pp. 873–882). Dordrecht: Springer Netherlands. Retrieved 2024-09-26, from http://link.springer.com/10.1007/978-90-481-2642-2_423 (Series Title: Encyclopedia of Earth Sciences Series) doi: 10.1007/978-90-481-2642-2_423

Ershadi, M. R., Drews, R., Martín, C., Eisen, O., Ritz, C., Corr, H., ... Mulvaney, R. (2022, May). Polarimetric radar reveals the spatial distribution of ice fabric at domes and divides in East Antarctica. *The Cryosphere*, *16*(5), 1719–

1739. Retrieved 2024-09-17, from https://tc.copernicus.org/articles/16/1719/2022/ (Publisher: Copernicus GmbH) doi: 10.5194/tc-16-1719-2022

Fahnestock, M., Abdalati, W., Joughin, I., Brozena, J., & Gogineni, P. (2001, December). High Geothermal Heat Flow, Basal Melt, and the Origin of Rapid Ice Flow in Central Greenland. *Science*, *294*(5550), 2338–2342. Retrieved 2024-10-14, from https://www.science.org/doi/10.1126/science.1065370 doi: 10.1126/science.1065370

Fahnestock, M., Bindschadler, R., Kwok, R., & Jezek, K. (1993, December). Greenland Ice Sheet Surface Properties and Ice Dynamics from ERS-1 SAR Imagery. *Science*, *262*(5139), 1530–1534. Retrieved 2024-10-14, from https://www.science.org/doi/10.1126/science.262.5139.1530 doi: 10.1126/science.262.5139.1530

Fichtner, A. (2021, July). *Lecture Notes on Inverse Theory.* Retrieved 2024-11-12, from https://www.cambridge.org/engage/coe/article-details/60e6a70d609d0d7fa3d893a7 doi: 10.33774/coe-2021-qpq2j

Fichtner, A., Hofstede, C., Gebraad, L., Zunino, A., Zigone, D., & Eisen, O. (2023, September). Borehole fibre-optic seismology inside the Northeast Greenland Ice Stream. *Geophysical Journal International*, *235*(3), 2430–2441. Retrieved 2024-10-14, from https://academic.oup.com/gji/article/235/3/2430/7303284 doi: 10.1093/gji/ggad344

Fichtner, A., Hofstede, C., N. Kennett, B. L., Nymand, N. F., Lauritzen, M. L., Zigone, D., & Eisen, O. (2023, April). Fiber-Optic Airplane Seismology on the Northeast Greenland Ice Stream. *The Seismic Record*, *3*(2), 125–133. Retrieved 2024-10-14, from https://pubs.geoscienceworld.org/tsr/article/3/2/125/623383/Fiber-Optic-Airplane-Seismology-on-the-Northeast doi: 10.1785/0320230004

Franke, S., Bons, P. D., Westhoff, J., Weikusat, I., Binder, T., Streng, K., ... Jansen, D. (2022, December). Holocene ice-stream shutdown and drainage basin reconfiguration in northeast Greenland. *Nature Geoscience*, *15*(12), 995–1001. Retrieved 2024-09-17, from https://www.nature.com/articles/s41561-022-01082-2 (Publisher: Springer Science and Business Media LLC) doi: 10.1038/s41561-022-01082-2

Franke, S., Jansen, D., Binder, T., Dörr, N., Helm, V., Paden, J., ... Eisen, O. (2020, April). Bed topography and subglacial landforms in the onset region of the Northeast Greenland Ice Stream. *Annals of Glaciology*, *61*(81), 143–153. Retrieved 2024-09-06, from https://www.cambridge.org/core/product/identifier/S0260305520000129/type/journal_article doi: 10.1017/aog.2020.12

Franke, S., Jansen, D., Binder, T., Paden, J. D., Dörr, N., Gerber, T. A., ... Eisen, O. (2022, February). Airborne ultra-wideband radar sounding over the shear margins and along flow lines at the onset region of the Northeast Greenland Ice Stream. *Earth System Science Data*, *14*(2), 763–779. Retrieved 2024-10-31, from https://

essd.copernicus.org/articles/14/763/2022/ doi: 10.5194/essd-14-763-2022

Fujita, S., & Mae, S. (1994). Causes and nature of ice-sheet radio-echo internal reflections estimated from the dielectric properties of ice. *Annals of Glaciology*, *20*, 80–86. Retrieved 2024-10-14, from https://www.cambridge.org/core/product/identifier/S026030550001627X/type/journal_article doi: 10.3189/1994AoG20-1-80-86

Fujita, S., Maeno, H., & Matsuoka, K. (2006). Radio-wave depolarization and scattering within ice sheets: a matrix-based model to link radar and ice-core measurements and its application. *Journal of Glaciology*, *52*(178), 407–424. Retrieved 2024-09-17, from https://www.cambridge.org/core/product/identifier/S0022143000211702/type/journal_article (Publisher: International Glaciological Society) doi: 10.3189/172756506781828548

Fujita, S., Maeno, H., Uratsuka, S., Furukawa, T., Mae, S., Fujii, Y., & Watanabe, O. (1999, June). Nature of radio echo layering in the Antarctic Ice Sheet detected by a two-frequency experiment. *Journal of Geophysical Research: Solid Earth*, *104*(B6), 13013–13024. Retrieved 2024-10-14, from https://agupubs.onlinelibrary.wiley.com/doi/10.1029/1999JB900034 doi: 10.1029/1999JB900034

Fujita, S., Matsuoka, T., Ishida, T., Matsuoka, K., & Mae, S. (2000). A summary of the complex dielectric permittivity of ice in the megahertz range and its applications for radar sounding of polar ice sheets. In *Physics of ice core records* (pp. 185–212). Shikotsukohan, Hokkaido, Japan: Hokkaido University Press.

Garboe, A. (1954, December). Nicolaus Steno (Niels Stensen) and Erasmus Bartholinus. Two 17 th Century Danish Scientists and the Foundation of exact Geology and Crystallography. *Danmarks Geologiske Undersøgelse IV. Række*, *3*(9), 1–48. Retrieved 2024-10-23, from https://geusjournals.org/index.php/raekke4/article/view/6991 doi: 10.34194/raekke4.v3.6991

George R. Jiracek. (1967). *Radio sounding of Antarctic ice* (Tech. Rep.). Geophysical & Polar Research Center, University of Wisconsin.

Gerber, T. A., Hvidberg, C. S., Rasmussen, S. O., Franke, S., Sinnl, G., Grinsted, A., ... Dahl-Jensen, D. (2021, August). Upstream flow effects revealed in the EastGRIP ice core using Monte Carlo inversion of a two-dimensional ice-flow model. *The Cryosphere*, *15*(8), 3655–3679. Retrieved 2024-09-17, from https://tc.copernicus.org/articles/15/3655/2021/ (Publisher: Copernicus GmbH) doi: 10.5194/tc-15-3655-2021

Gerber, T. A., Lilien, D. A., Nymand, N. F., Steinhage, D., Eisen, O., & Dahl-Jensen, D. (2024, September). *Anisotropic Scattering in Radio-Echo Sounding: Insights from Northeast Greenland.* Retrieved 2024-11-15, from https://egusphere.copernicus.org/preprints/2024/egusphere-2024-2276/ doi: 10.5194/egusphere-2024-2276

Gerber, T. A., Lilien, D. A., Rathmann, N. M., Franke, S., Young, T. J., Valero-Delgado,

F., ... Eisen, O. (2023, May). Crystal orientation fabric anisotropy causes directional hardening of the Northeast Greenland Ice Stream. *Nature Communications*, *14*(1). Retrieved 2024-09-17, from https://www.nature.com/articles/s41467-023-38139-8 (Publisher: Springer Science and Business Media LLC) doi: 10.1038/s41467-023-38139-8

Glen, J. W. (1952). Experiments on the Deformation of Ice. *Journal of Glaciology*, *2*(12), 111–114. Retrieved 2024-12-18, from https://www.cambridge.org/core/product/identifier/S0022143000034067/type/journal_article doi: 10.3189/S0022143000034067

Glen, J. W. (1955, March). The creep of polycrystalline ice. *Proceedings of the Royal Society of London. Series A. Mathematical and Physical Sciences*, *228*(1175), 519–538. Retrieved 2024-10-04, from https://royalsocietypublishing.org/doi/10.1098/rspa.1955.0066 doi: 10.1098/rspa.1955.0066

Glen, J. W. (1975). *The Mechanics of Ice.* [Department of Defense], Department of the Army, Corps of Engineers, Army Cold Regions Research and Engineering Laboratory. Retrieved from https://books.google.dk/books?id=IF9dirO9Ee4C

Gogineni, S., Tammana, D., Braaten, D., Leuschen, C., Akins, T., Legarsky, J., ... Jezek, K. (2001, December). Coherent radar ice thickness measurements over the Greenland ice sheet. *Journal of Geophysical Research: Atmospheres*, *106*(D24), 33761–33772. Retrieved 2024-10-29, from https://agupubs.onlinelibrary.wiley.com/doi/10.1029/2001JD900183 doi: 10.1029/2001JD900183

Griffiths, D. J. (2013). *Introduction to electrodynamics* (4. ed., intern. ed ed.). Boston Munich: Pearson.

Grinsted, A., Hvidberg, C. S., Lilien, D. A., Rathmann, N. M., Karlsson, N. B., Gerber, T., ... Dahl-Jensen, D. (2022, September). Accelerating ice flow at the onset of the Northeast Greenland Ice Stream. *Nature Communications*, *13*(1). Retrieved 2024-09-17, from https://www.nature.com/articles/s41467-022-32999-2 (Publisher: Springer Science and Business Media LLC) doi: 10.1038/s41467-022-32999-2

Gudmandsen, P. (1969, December). Airborne Radio Echo Sounding of the Greenland Ice Sheet. *The Geographical Journal*, *135*(4), 548. Retrieved 2024-10-28, from https://www.jstor.org/stable/1795099?origin=crossref doi: 10.2307/1795099

Gudmandsen, P. (1975). Layer echoes in polar ice sheets. *Journal of Glaciology*, *15*(73), 95–101. Retrieved 2024-10-17, from https://www.cambridge.org/core/product/identifier/S0022143000034304/type/journal_article doi: 10.3189/S0022143000034304

Hargreaves, N. D. (1977, June). The polarization of radio signals in the radio echo sounding of ice sheets. *Journal of Physics D: Applied Physics*, *10*(9), 1285–1304. Retrieved 2024-09-17, from https://iopscience.iop.org/article/10.1088/0022-3727/10/9/012 (Publisher: IOP Publishing) doi: 10.1088/0022-3727/10/9/012

Hargreaves, N. D. (1978). The Radio-Frequency Birefringence of Polar Ice. *Journal of Glaciology*, *21*(85), 301–313. Retrieved 2024-09-24, from https://www.cambridge.org/core/product/identifier/S0022143000033499/type/journal_article doi: 10.3189/S0022143000033499

Hecht, E. (2017). *Optics* (5edition. Global edition ed.). Boston: Pearson Education, Inc.

Hvidberg, C. S., Grinsted, A., Dahl-Jensen, D., Khan, S. A., Kusk, A., Andersen, J. K., ... Vallelonga, P. (2020, October). Surface velocity of the Northeast Greenland Ice Stream (NEGIS): assessment of interior velocities derived from satellite data by GPS. *The Cryosphere*, *14*(10), 3487–3502. Retrieved 2024-09-17, from https://tc.copernicus.org/articles/14/3487/2020/ (Publisher: Copernicus GmbH) doi: 10.5194/tc-14-3487-2020

IPCC. (2022). *The Ocean and Cryosphere in a Changing Climate: Special Report of the Intergovernmental Panel on Climate Change* (1st ed.). Cambridge University Press. Retrieved 2024-09-26, from https://www.cambridge.org/core/product/identifier/9781009157964/type/book doi: 10.1017/9781009157964

IPCC. (2023). *Climate Change 2021 – The Physical Science Basis: Working Group I Contribution to the Sixth Assessment Report of the Intergovernmental Panel on Climate Change* (1st ed.). Cambridge University Press. Retrieved 2024-10-01, from https://www.cambridge.org/core/product/identifier/9781009157896/type/book doi: 10.1017/9781009157896

Jacobel, R. W., Welch, B. C., Osterhouse, D., Pettersson, R., & MacGregor, J. A. (2009). Spatial variation of radar-derived basal conditions on Kamb Ice Stream, West Antarctica. *Annals of Glaciology*, *50*(51), 10–16. Retrieved 2024-12-11, from https://www.cambridge.org/core/product/identifier/S0260305500250507/type/journal_article doi: 10.3189/172756409789097504

Jansen, D., Franke, S., Bauer, C. C., Binder, T., Dahl-Jensen, D., Eichler, J., ... Bons, P. D. (2024, February). Shear margins in upper half of Northeast Greenland Ice Stream were established two millennia ago. *Nature Communications*, *15*(1). Retrieved 2024-09-17, from https://www.nature.com/articles/s41467-024-45021-8 (Publisher: Springer Science and Business Media LLC) doi: 10.1038/s41467-024-45021-8

Jordan, T. M., Schroeder, D. M., Castelletti, D., Li, J., & Dall, J. (2019, November). A Polarimetric Coherence Method to Determine Ice Crystal Orientation Fabric From Radar Sounding: Application to the NEEM Ice Core Region. *IEEE Transactions on Geoscience and Remote Sensing*, *57*(11), 8641–8657. Retrieved 2024-09-17, from https://ieeexplore.ieee.org/document/8755860/ (Publisher: Institute of Electrical and Electronics Engineers (IEEE)) doi: 10.1109/tgrs.2019.2921980

Jordan, T. M., Schroeder, D. M., Elsworth, C. W., & Siegfried, M. R. (2020, April). Estimation of ice fabric within Whillans Ice Stream using polari-

metric phase-sensitive radar sounding. *Annals of Glaciology*, *61*(81), 74–83. Retrieved 2024-11-08, from https://www.cambridge.org/core/product/identifier/S0260305520000063/type/journal_article doi: 10.1017/aog.2020.6

Joughin, I., Smith, B. E., & Howat, I. M. (2018, February). A complete map of Greenland ice velocity derived from satellite data collected over 20 years. *Journal of Glaciology*, *64*(243), 1–11. Retrieved 2024-09-17, from https://www.cambridge.org/core/product/identifier/S0022143017000739/type/journal_article (Publisher: Cambridge University Press (CUP)) doi: 10.1017/jog.2017.73

Joughin, I., & University Of Washington. (2016). *MEaSUREs Multi-year Greenland Ice Sheet Velocity Mosaic, Version 1.* NASA National Snow and Ice Data Center Distributed Active Archive Center. Retrieved 2024-09-17, from https://nsidc.org/data/NSIDC-0670/versions/1 doi: 10.5067/QUA5Q9SVMSJG

Karlsson, N. B., Schroeder, D. M., Sørensen, L. S., Chu, W., Dall, J., Andersen, N. H., ... Skou, N. (2024, July). A newly digitized ice-penetrating radar data set acquired over the Greenland ice sheet in 1971–1979. *Earth System Science Data*, *16*(7), 3333–3344. Retrieved 2024-10-28, from https://essd.copernicus.org/articles/16/3333/2024/ doi: 10.5194/essd-16-3333-2024

Keisling, B. A., Christianson, K., Alley, R. B., Peters, L. E., Christian, J. E., Anandakrishnan, S., ... Jacobel, R. W. (2014). Basal conditions and ice dynamics inferred from radar-derived internal stratigraphy of the northeast Greenland ice stream. *Annals of Glaciology*, *55*(67), 127–137. Retrieved 2024-10-16, from https://www.cambridge.org/core/product/identifier/S0260305500256486/type/journal_article doi: 10.3189/2014AoG67A090

Khan, S. A., Kjær, K. H., Bevis, M., Bamber, J. L., Wahr, J., Kjeldsen, K. K., ... Muresan, I. S. (2014, April). Sustained mass loss of the northeast Greenland ice sheet triggered by regional warming. *Nature Climate Change*, *4*(4), 292–299. Retrieved 2024-10-14, from https://www.nature.com/articles/nclimate2161 doi: 10.1038/nclimate2161

Lauritzen, M. L., Solgaard, A. M., Rathmann, N. M., Vinther, B. M., Grindsted, A., Noël, B., ... Hvidberg, C. S. (2024, July). *Modeled Greenland Ice Sheet evolution constrained by ice-core-derived Holocene elevation histories.* Retrieved 2024-10-09, from https://egusphere.copernicus.org/preprints/2024/egusphere-2024-2223/ doi: 10.5194/egusphere-2024-2223

Lautrup, B. (2019). *Physics of continuous matter: exotic and everyday phenomena in the macroscopic world* (2nd edition ed.). Boca Raton, Fla.: CRC Press.

Li, J., Vélez González, J. A., Leuschen, C., Harish, A., Gogineni, P., Montagnat, M., ... Paden, J. (2018, August). Multi-channel and multi-polarization radar measurements around the NEEM site. *The Cryosphere*, *12*(8), 2689–2705. Retrieved

2024-12-11, from https://tc.copernicus.org/articles/12/2689/2018/ doi: 10.5194/tc-12-2689-2018

Li, L. (2021). *Ultrawide-Band Polarimetric Multi-Channel Radar for Measurements of Polar Ice Sheets* (Ph.D. Thesis). The University of Alabama, Electrical engineering.

Li, L., Yan, J.-B., Gogineni, S., O'Neill, C., Dahl-Jensen, D., Simpson, C. D., ... Eisen, O. (2020, September). Ground-Based Ultra Wideband Dual-Polarized Radar Sounding of Greenland Ice Sheets. In *IGARSS 2020 - 2020 IEEE International Geoscience and Remote Sensing Symposium* (pp. 1417–1419). Waikoloa, HI, USA: IEEE. Retrieved 2024-09-17, from https://ieeexplore.ieee.org/document/9323479/ doi: 10.1109/igarss39084.2020.9323479

Lilien, D. A., Hills, B. H., Driscol, J., Jacobel, R., & Christianson, K. (2020, April). ImpDAR: an open-source impulse radar processor. *Annals of Glaciology*, *61*(81), 114–123. Retrieved 2024-09-17, from https://www.cambridge.org/core/product/identifier/S0260305520000440/type/journal_article (Publisher: Cambridge University Press (CUP)) doi: 10.1017/aog.2020.44

Lilien, D. A., Nymand, N. F., Gerber, T. A., Steinhage, D., Jansen, D., Thomson, L., ... Dahl-Jensen, D. (2024, October). Potential to recover a record of Holocene climate and sea ice from Müller Ice Cap, Canada. *Journal of Glaciology*, 1–16. Retrieved 2024-11-04, from https://www.cambridge.org/core/product/identifier/S0022143024000753/type/journal_article doi: 10.1017/jog.2024.75

Lilien, D. A., Rathmann, N. M., Hvidberg, C. S., Grinsted, A., Ershadi, M. R., Drews, R., & Dahl-Jensen, D. (2023, November). Simulating higher-order fabric structure in a coupled, anisotropic ice-flow model: application to Dome C. *Journal of Glaciology*, 1–20. Retrieved 2024-09-17, from https://www.cambridge.org/core/product/identifier/S0022143023000783/type/journal_article (Publisher: Cambridge University Press (CUP)) doi: 10.1017/jog.2023.78

Lilien, D. A., Steinhage, D., Taylor, D., Parrenin, F., Ritz, C., Mulvaney, R., ... Eisen, O. (2021, April). Brief communication: New radar constraints support presence of ice older than 1.5 Myr at Little Dome C. *The Cryosphere*, *15*(4), 1881–1888. Retrieved 2024-10-14, from https://tc.copernicus.org/articles/15/1881/2021/ doi: 10.5194/tc-15-1881-2021

MacGregor, J. A., Fahnestock, M. A., Catania, G. A., Paden, J. D., Prasad Gogineni, S., Young, S. K., ... Morlighem, M. (2015, February). Radiostratigraphy and age structure of the Greenland Ice Sheet. *Journal of Geophysical Research: Earth Surface*, *120*(2), 212–241. Retrieved 2024-10-14, from https://agupubs.onlinelibrary.wiley.com/doi/10.1002/2014JF003215 doi: 10.1002/2014JF003215

Marzeion, B., Jarosch, A. H., & Hofer, M. (2012, November). Past and future sea-level change from the surface mass balance of glaciers. *The Cryosphere*, *6*(6),

1295–1322. Retrieved 2024-10-02, from https://tc.copernicus.org/articles/6/1295/2012/ doi: 10.5194/tc-6-1295-2012

Matsuoka, K., Pattyn, F., Callens, D., & Conway, H. (2012). Radar characterization of the basal interface across the grounding zone of an ice-rise promontory in East Antarctica. *Annals of Glaciology*, *53*(60), 29–34. Retrieved 2024-12-11, from https://www.cambridge.org/core/product/identifier/S0260305500251707/type/journal_article doi: 10.3189/2012AoG60A106

Matsuoka, T., Fujita, S., & Mae, S. (1996, November). Effect of temperature on dielectric properties of ice in the range 5–39 GHz. *Journal of Applied Physics*, *80*(10), 5884–5890. Retrieved 2024-10-21, from https://pubs.aip.org/jap/article/80/10/5884/495326/Effect-of-temperature-on-dielectric-properties-of doi: 10.1063/1.363582

Matsuoka, T., Fujita, S., Morishima, S., & Mae, S. (1997, March). Precise measurement of dielectric anisotropy in ice Ih at 39 GHz. *Journal of Applied Physics*, *81*(5), 2344–2348. Retrieved 2024-10-21, from https://pubs.aip.org/jap/article/81/5/2344/178441/Precise-measurement-of-dielectric-anisotropy-in doi: 10.1063/1.364238

McConnel, J. C. (1891, March). On the plasticity of an ice crystal. *Proceedings of the Royal Society of London*, *49*, 323–343. (Publisher: The Royal Society London)

Menke, W. (2018). *Geophysical data analysis: discrete inverse theory* (4th ed ed.). London: Academic press an imprint of Elsevier.

Morlighem, M. (2022). *IceBridge BedMachine Greenland, Version 5.* NASA National Snow and Ice Data Center Distributed Active Archive Center. Retrieved 2024-10-03, from https://nsidc.org/data/IDBMG4/versions/5 doi: 10.5067/GMEVBWFLWA7X

Morlighem, M., Williams, C. N., Rignot, E., An, L., Arndt, J. E., Bamber, J. L., ... Zinglersen, K. B. (2017, November). BedMachine v3: Complete Bed Topography and Ocean Bathymetry Mapping of Greenland From Multibeam Echo Sounding Combined With Mass Conservation. *Geophysical Research Letters*, *44*(21). Retrieved 2024-12-11, from https://agupubs.onlinelibrary.wiley.com/doi/10.1002/2017GL074954 doi: 10.1002/2017GL074954

NEEM community members. (2013, January). Eemian interglacial reconstructed from a Greenland folded ice core. *Nature*, *493*(7433), 489–494. Retrieved 2024-09-17, from https://www.nature.com/articles/nature11789 (Publisher: Springer Science and Business Media LLC) doi: 10.1038/nature11789

Nicholls, K. W., Corr, H. F., Stewart, C. L., Lok, L. B., Brennan, P. V., & Vaughan, D. G. (2015). A ground-based radar for measuring vertical strain rates and time-varying basal melt rates in ice sheets and shelves. *Journal of Glaciology*, *61*(230), 1079–1087. Retrieved 2024-11-08, from https://www.cambridge.org/core/product/identifier/S0022143000200269/type/journal_article doi:

10.3189/2015JoG15J073

Nye, J. (1957, February). The distribution of stress and velocity in glaciers and ice-sheets. *Proceedings of the Royal Society of London. Series A. Mathematical and Physical Sciences*, *239*(1216), 113–133. Retrieved 2024-10-07, from https://royalsocietypublishing.org/doi/10.1098/rspa.1957.0026 doi: 10.1098/rspa.1957.0026

Owen, C. C., & Hendrikse, H. (2023, February). An initial study of interference coloration for quantifying the texture and fabric of ice. *Cold Regions Science and Technology*, *206*, 103735. Retrieved 2024-10-23, from https://linkinghub.elsevier.com/retrieve/pii/S0165232X22002543 doi: 10.1016/j.coldregions.2022.103735

Plewes, L. A., & Hubbard, B. (2001, June). A review of the use of radio-echo sounding in glaciology. *Progress in Physical Geography: Earth and Environment*, *25*(2), 203–236. Retrieved 2024-10-14, from https://journals.sagepub.com/doi/10.1177/030913330102500203 doi: 10.1177/030913330102500203

Rapp, D. (2011). Ice Age Cycles: Data, Models, and Uncertainties. In V. P. Singh, P. Singh, & U. K. Haritashya (Eds.), *Encyclopedia of Snow, Ice and Glaciers* (pp. 565–576). Dordrecht: Springer Netherlands. Retrieved 2024-09-26, from https://link.springer.com/10.1007/978-90-481-2642-2_565 (Series Title: Encyclopedia of Earth Sciences Series) doi: 10.1007/978-90-481-2642-2_565

Rathmann, N. M., & Lilien, D. A. (2022, April). Inferred basal friction and mass flux affected by crystal-orientation fabrics. *Journal of Glaciology*, *68*(268), 236–252. Retrieved 2024-09-17, from https://www.cambridge.org/core/product/identifier/S0022143021000885/type/journal_article (Publisher: Cambridge University Press (CUP)) doi: 10.1017/jog.2021.88

Rathmann, N. M., Lilien, D. A., Grinsted, A., Gerber, T. A., Young, T. J., & Dahl-Jensen, D. (2022, January). On the Limitations of Using Polarimetric Radar Sounding to Infer the Crystal Orientation Fabric of Ice Masses. *Geophysical Research Letters*, *49*(1). Retrieved 2024-09-17, from https://agupubs.onlinelibrary.wiley.com/doi/10.1029/2021GL096244 (Publisher: American Geophysical Union (AGU)) doi: 10.1029/2021gl096244

Richards, D. H., Pegler, S. S., Piazolo, S., & Harlen, O. G. (2021, February). The evolution of ice fabrics: A continuum modelling approach validated against laboratory experiments. *Earth and Planetary Science Letters*, *556*, 116718. Retrieved 2024-09-17, from https://linkinghub.elsevier.com/retrieve/pii/S0012821X20306622 (Publisher: Elsevier BV) doi: 10.1016/j.epsl.2020.116718

Richards, D. H., Pegler, S. S., Piazolo, S., Stoll, N., & Weikusat, I. (2023, November). Bridging the Gap Between Experimental and Natural Fabrics: Modeling Ice Stream Fabric Evolution and its Comparison With Ice-Core Data. *Journal of Geophysical Research: Solid Earth*, *128*(11). Retrieved 2024-09-17, from https://agupubs.onlinelibrary.wiley.com/doi/10.1029/2023JB027245 (Publisher:

American Geophysical Union (AGU)) doi: 10.1029/2023jb027245

Rodriguez-Morales, F., Byers, K., Crowe, R., Player, K., Hale, R. D., Arnold, E. J., ... Patel, A. (2014, May). Advanced Multifrequency Radar Instrumentation for Polar Research. *IEEE Transactions on Geoscience and Remote Sensing*, *52*(5), 2824–2842. Retrieved 2024-10-29, from https://ieeexplore.ieee.org/document/6557071/ doi: 10.1109/TGRS.2013.2266415

Schroeder, D. M., Bingham, R. G., Blankenship, D. D., Christianson, K., Eisen, O., Flowers, G. E., ... Siegert, M. J. (2020, April). Five decades of radioglaciology. *Annals of Glaciology*, *61*(81), 1–13. Retrieved 2024-09-17, from https://www.cambridge.org/core/product/identifier/S0260305520000117/type/journal_article (Publisher: Cambridge University Press (CUP)) doi: 10.1017/aog.2020.11

Shoji, H., & Langway, C. (1988). Flow-Law Parameters of the Dye 3, Greenland, Deep Ice Core. *Annals of Glaciology*, *10*, 146–150. Retrieved 2024-10-07, from https://www.cambridge.org/core/product/identifier/S026030550000433X/type/journal_article doi: 10.3189/S026030550000433X

Skolnik, M. I. (2007). *Introduction to radar systems* (3. ed., internat. ed., [Nachdr.] ed.). Boston: McGraw-Hill.

Smith, A. M. (1997, January). Basal conditions on Rutford Ice Stream, West Antarctica, from seismic observations. *Journal of Geophysical Research: Solid Earth*, *102*(B1), 543–552. Retrieved 2024-10-14, from https://agupubs.onlinelibrary.wiley.com/doi/10.1029/96JB02933 doi: 10.1029/96JB02933

Smith, E. C., Baird, A. F., Kendall, J. M., Martín, C., White, R. S., Brisbourne, A. M., & Smith, A. M. (2017, April). Ice fabric in an Antarctic ice stream interpreted from seismic anisotropy. *Geophysical Research Letters*, *44*(8), 3710–3718. Retrieved 2024-09-17, from https://agupubs.onlinelibrary.wiley.com/doi/10.1002/2016GL072093 (Publisher: American Geophysical Union (AGU)) doi: 10.1002/2016gl072093

Smith-Johnsen, S., De Fleurian, B., Schlegel, N., Seroussi, H., & Nisancioglu, K. (2020, March). Exceptionally high heat flux needed to sustain the Northeast Greenland Ice Stream. *The Cryosphere*, *14*(3), 841–854. Retrieved 2024-10-14, from https://tc.copernicus.org/articles/14/841/2020/ doi: 10.5194/tc-14-841-2020

Stoll, N., Weikusat, I., Jansen, D., Bons, P., Darányi, K., Westhoff, J., ... Kerch, J. (2024, October). *EastGRIP ice core reveals the exceptional evolution of crystallographic preferred orientation throughout the Northeast Greenland Ice Stream.* Retrieved 2024-11-26, from https://egusphere.copernicus.org/preprints/2024/egusphere-2024-2653/ doi: 10.5194/egusphere-2024-2653

Svensson, A., Durand, G., Mathiesen, J., Persson, A., & Dahl-Jensen, D. (2009). Texture of the upper 1000 m in the GRIP and NorthGRIP ice cores. In *Low Temperature Science Supplement Issue : Physics of Ice Core Records II* (Vol. 68, pp. 107–113). Sapporo, Japan: Institute of Low Temperature Science, Hokkaido University,

Sapporo Japan.

Tabone, I., Robinson, A., Montoya, M., & Alvarez-Solas, J. (2024, July). Holocene thinning in central Greenland controlled by the Northeast Greenland Ice Stream. *Nature Communications*, *15*(1), 6434. Retrieved 2024-12-18, from https://www.nature.com/articles/s41467-024-50772-5 doi: 10.1038/s41467-024-50772-5

Thorsteinsson, T., Kipfstuhl, J., & Miller, H. (1997, November). Textures and fabrics in the GRIP ice core. *Journal of Geophysical Research: Oceans*, *102*(C12), 26583–26599. Retrieved 2024-09-17, from https://agupubs.onlinelibrary.wiley.com/doi/10.1029/97JC00161 (Publisher: American Geophysical Union (AGU)) doi: 10.1029/97jc00161

Vallelonga, P., Christianson, K., Alley, R. B., Anandakrishnan, S., Christian, J. E. M., Dahl-Jensen, D., ... Winstrup, M. (2014, July). Initial results from geophysical surveys and shallow coring of the Northeast Greenland Ice Stream (NEGIS). *The Cryosphere*, *8*(4), 1275–1287. Retrieved 2024-10-16, from https://tc.copernicus.org/articles/8/1275/2014/ doi: 10.5194/tc-8-1275-2014

Vinther, B. M., Buchardt, S. L., Clausen, H. B., Dahl-Jensen, D., Johnsen, S. J., Fisher, D. A., ... Svensson, A. M. (2009, September). Holocene thinning of the Greenland ice sheet. *Nature*, *461*(7262), 385–388. Retrieved 2024-10-09, from https://www.nature.com/articles/nature08355 doi: 10.1038/nature08355

Weikusat, I., Stoll, N., Kerch, J., Eichler, J., Jansen, D., & Kipfstuhl, S. (2022). *Crystal c-axes (fabric analyser G50) of ice core samples (vertical thin sections) collected from the polar ice core EGRIP, 111-1714 m depth.* PANGAEA. Retrieved 2024-09-17, from https://doi.pangaea.de/10.1594/PANGAEA.949248 (Artwork Size: 16367 data points Pages: 16367 data points) doi: 10.1594/PANGAEA.949248

Westhoff, J., Stoll, N., Franke, S., Weikusat, I., Bons, P., Kerch, J., ... Dahl-Jensen, D. (2021, September). A stratigraphy-based method for reconstructing ice core orientation. *Annals of Glaciology*, *62*(85-86), 191–202. Retrieved 2024-09-17, from https://www.cambridge.org/core/product/identifier/S0260305520000762/type/journal_article (Publisher: Cambridge University Press (CUP)) doi: 10.1017/aog.2020.76

Woodcock, N. H. (1977). Specification of fabric shapes using an eigenvalue method. *Geological Society of America Bulletin*, *88*(9), 1231. Retrieved 2024-10-11, from https://pubs.geoscienceworld.org/gsabulletin/article/88/9/1231-1236/202166 doi: 10.1130/0016-7606(1977)88⟨1231:SOFSUA⟩2.0.CO;2

Wuestefeld, A., Al-Harrasi, O., Verdon, J. P., Wookey, J., & Kendall, J. M. (2010, September). A strategy for automated analysis of passive microseismic data to image seismic anisotropy and fracture characteristics. *Geophysical Prospecting*, *58*(5), 755–773. Retrieved 2024-10-14, from https://onlinelibrary.wiley.com/doi/10.1111/j.1365-2478.2010.00891.x doi: 10.1111/j.1365-2478.2010.00891.x

Yan, J.-B., Li, L., Nunn, J. A., Dahl-Jensen, D., O'Neill, C., Taylor, R. A., ... Eisen, O. (2020). Multiangle, Frequency, and Polarization Radar Measurement of Ice Sheets. *IEEE Journal of Selected Topics in Applied Earth Observations and Remote Sensing*, *13*, 2070–2080. Retrieved 2024-10-29, from https://ieeexplore.ieee.org/document/9086068/ doi: 10.1109/JSTARS.2020.2991682

Yokoyama, Y., Esat, T. M., Thompson, W. G., Thomas, A. L., Webster, J. M., Miyairi, Y., ... Kan, H. (2018, July). Rapid glaciation and a two-step sea level plunge into the Last Glacial Maximum. *Nature*, *559*(7715), 603–607. Retrieved 2024-10-01, from https://www.nature.com/articles/s41586-018-0335-4 doi: 10.1038/s41586-018-0335-4

Young, D. A., Schroeder, D. M., Blankenship, D. D., Kempf, S. D., & Quartini, E. (2016, January). The distribution of basal water between Antarctic subglacial lakes from radar sounding. *Philosophical Transactions of the Royal Society A: Mathematical, Physical and Engineering Sciences*, *374*(2059), 20140297. Retrieved 2024-12-11, from https://royalsocietypublishing.org/doi/10.1098/rsta.2014.0297 doi: 10.1098/rsta.2014.0297

Young, T. J., Martín, C., Christoffersen, P., Schroeder, D. M., Tulaczyk, S. M., & Dawson, E. J. (2021, August). Rapid and accurate polarimetric radar measurements of ice crystal fabric orientation at the Western Antarctic Ice Sheet (WAIS) Divide ice core site. *The Cryosphere*, *15*(8), 4117–4133. Retrieved 2024-09-16, from https://tc.copernicus.org/articles/15/4117/2021/ doi: 10.5194/tc-15-4117-2021

Zeising, O., Arenas-Pingarrón, A., Brisbourne, A. M., & Martín, C. (2024, September). *Brief communication: Reduced bandwidth improves the depth limit of the radar coherence method for detecting ice crystal fabric asymmetry.* Retrieved 2024-11-13, from https://egusphere.copernicus.org/preprints/2024/egusphere-2024-2519/ doi: 10.5194/egusphere-2024-2519

Zeising, O., Gerber, T. A., Eisen, O., Ershadi, M. R., Stoll, N., Weikusat, I., & Humbert, A. (2023, March). Improved estimation of the bulk ice crystal fabric asymmetry from polarimetric phase co-registration. *The Cryosphere*, *17*(3), 1097–1105. Retrieved 2024-09-12, from https://tc.copernicus.org/articles/17/1097/2023/ doi: 10.5194/tc-17-1097-2023

Appendix A

Wave propagation in ice

The determinant shown in equation 2.10 can be expanded as follows,

$$\begin{vmatrix} -(k_y^2+k_z^2)+\frac{\omega^2}{c_0^2}\varepsilon_\perp & k_yk_x & k_zk_x \\ k_yk_x & -(k_x^2+k_z^2)+\frac{\omega^2}{c_0^2}\varepsilon_\perp & k_zk_y \\ k_zk_x & k_zk_y & -(k_x^2+k_y^2)+\frac{\omega^2}{c_0^2}\varepsilon_\parallel \end{vmatrix} =$$

$$\frac{\omega^2}{c_0^2}\left(\frac{\omega^2}{c_0^2}\varepsilon_\perp - k_x^2-k_y^2-k_z^2\right)\left(\varepsilon_\perp\left(\frac{\omega^2}{c_0^2}\varepsilon_\parallel - k_x^2-k_y^2\right)-\varepsilon_\parallel k_z^2\right)=0$$

$$\Rightarrow \left(\frac{\omega^2}{c_0^2}\varepsilon_\perp - k_x^2-k_y^2-k_z^2\right)\left(\frac{\omega^2}{c_0^2}\varepsilon_\parallel - k_x^2-k_y^2-\frac{\varepsilon_\parallel}{\varepsilon_\perp}k_z^2\right)=0$$

$$\Rightarrow \left(\frac{k_x^2}{\varepsilon_\perp}+\frac{k_y^2}{\varepsilon_\perp}+\frac{k_z^2}{\varepsilon_\perp}-\frac{\omega^2}{c_0^2}\right)\left(\frac{k_x^2}{\varepsilon_\parallel}+\frac{k_y^2}{\varepsilon_\parallel}+\frac{k_z^2}{\varepsilon_\perp}-\frac{\omega^2}{c_0^2}\right)=0$$

For the simple case where $\mathbf{k}=(k_x,0,0)^T$ the electric field polarization can be found by inserting the two wave solutions, $k_x=\frac{\omega}{c_0}\sqrt{\varepsilon_\perp}$ and $k_x=\frac{\omega}{c_0}\sqrt{\varepsilon_\parallel}$,

$$\text{Ordinary: } \begin{pmatrix} \frac{\omega^2}{c_0^2}\varepsilon_\perp & 0 & 0 \\ 0 & 0 & 0 \\ 0 & 0 & \frac{\omega^2}{c_0^2}\Delta\varepsilon \end{pmatrix}\begin{pmatrix} E_x \\ E_y \\ E_z \end{pmatrix} = \begin{pmatrix} 0 \\ 0 \\ 0 \end{pmatrix} \Rightarrow \mathbf{P} = \begin{pmatrix} 0 \\ 1 \\ 0 \end{pmatrix}$$

$$\text{Extraordinary: } \begin{pmatrix} \frac{\omega^2}{c_0^2}\varepsilon_\perp & 0 & 0 \\ 0 & -\frac{\omega^2}{c_0^2}\Delta\varepsilon & 0 \\ 0 & 0 & 0 \end{pmatrix}\begin{pmatrix} E_x \\ E_y \\ E_z \end{pmatrix} = \begin{pmatrix} 0 \\ 0 \\ 0 \end{pmatrix} \Rightarrow \mathbf{P} = \begin{pmatrix} 0 \\ 0 \\ 1 \end{pmatrix}$$

A more general case with $\mathbf{k} = k_0(\sin\alpha, 0, \cos\alpha)^T$. The ordinary wave is then,

Ordinary:

$$\frac{k_0}{\varepsilon_\perp}(\sin^2\alpha + \cos^2\alpha) = \frac{\omega^2}{c_0^2} \Rightarrow k_0 = \frac{\omega}{c_0}\sqrt{\varepsilon_\perp}$$

$$\begin{pmatrix} k_0^2(1-\cos^2\alpha) & 0 & k_0^2\cos\alpha\sin\alpha \\ 0 & 0 & 0 \\ k_0^2\cos\alpha\sin\alpha & 0 & \frac{\omega^2}{c_0^2}\varepsilon_\parallel - k_0^2\sin^2\alpha \end{pmatrix} \begin{pmatrix} E_x \\ E_y \\ E_z \end{pmatrix} = \begin{pmatrix} 0 \\ 0 \\ 0 \end{pmatrix} \Rightarrow \mathbf{P} = \begin{pmatrix} 0 \\ 1 \\ 0 \end{pmatrix}$$

E_x and E_z have to satisfy the following two equations, and the only solution is $E_x = 0$ and $E_z = 0$,

$$E_x = -E_z\frac{k_0^2\cos\alpha\sin\alpha}{k_0^2\sin^2\alpha} = -E_z\frac{\cos\alpha}{\sin\alpha}$$

$$E_x = -E_z\frac{\frac{\omega^2}{c_0^2}\varepsilon_\parallel - k_0^2\sin^2\alpha}{k_0^2\sin\alpha\cos\alpha} = -E_z\left(\frac{\varepsilon_\parallel}{\varepsilon_\perp\sin\alpha\cos\alpha} - \frac{\sin\alpha}{\cos\alpha}\right)$$

For the extraordinary wave,

Extraordinary:

$$k_0^2\left(\frac{1}{\varepsilon_\parallel}\sin^2\alpha + \frac{1}{\varepsilon_\perp}\cos^2\alpha\right) \Rightarrow k_0^2 = \frac{\omega^2/c_0^2}{\frac{1}{\varepsilon_\parallel}\sin^2\alpha + \frac{1}{\varepsilon_\perp}\cos^2\alpha} = \frac{\omega^2/c_0^2\varepsilon_\perp\varepsilon_\parallel}{\varepsilon_\perp\sin^2\alpha + \varepsilon_\parallel\cos^2\alpha}$$

$$\begin{pmatrix} \frac{\omega^2}{c_0^2}\varepsilon_\perp - k_0^2\cos^2\alpha & 0 & k_0^2\cos\alpha\sin\alpha \\ 0 & \frac{\omega^2}{c_0^2}\varepsilon_\perp - k_0^2 & 0 \\ k_0^2\cos\alpha\sin\alpha & 0 & \frac{\omega^2}{c_0^2}\varepsilon_\parallel - k_0^2\sin^2\alpha \end{pmatrix} \begin{pmatrix} E_x \\ E_y \\ E_z \end{pmatrix} = \begin{pmatrix} 0 \\ 0 \\ 0 \end{pmatrix}$$

(i): $E_x\left(\frac{\omega^2}{c_0^2}\varepsilon_\perp - k_0^2\cos^2\alpha\right) = -E_z k_0^2\sin\alpha\cos\alpha \Rightarrow E_z = -E_x\left(\frac{\omega^2/c_0^2\varepsilon_\perp}{k_0^2\sin\alpha\cos\alpha} - \frac{\cos\alpha}{\sin\alpha}\right)$

$$\Rightarrow E_z = -E_x\left(\frac{\varepsilon_\perp\sin^2\alpha + \varepsilon_\parallel\cos^2\alpha}{\varepsilon_\parallel\sin\alpha\cos\alpha} - \frac{\cos\alpha}{\sin\alpha}\right) = -E_x\left(\frac{\varepsilon_\perp\sin^2\alpha}{\varepsilon_\parallel\sin\alpha\cos\alpha}\right)$$

$$\Rightarrow \boxed{E_x = -E_z\frac{\varepsilon_\parallel\cos\alpha}{\varepsilon_\perp\sin\alpha}}$$

(ii): $E_x = -E_z\left(\frac{\omega^2/c_0^2\varepsilon_\parallel}{k_0^2\sin\alpha\cos\alpha} - \frac{\sin\alpha}{\cos\alpha}\right) = -E_z\left(\frac{\varepsilon_\perp\sin^2\alpha + \varepsilon_\parallel\cos^2\alpha}{\varepsilon_\perp\sin\alpha\cos\alpha} - \frac{\sin\alpha}{\cos\alpha}\right)$

$$\Rightarrow \boxed{E_x = -E_z\frac{\varepsilon_\parallel\cos\alpha}{\varepsilon_\perp\sin\alpha}}$$

Assuming $\sin\alpha \neq 0$. Now there is a non-trivial solution to E_x and E_z. The normalization condition, $|\mathbf{P}| = 1$, and of course $E_i = P_i E_0 \exp j(\mathbf{k}\cdot\mathbf{r} - \omega t)$, yield the following,

$$\mathbf{P} = P_0 \begin{pmatrix} -\frac{\varepsilon_{\parallel} \cos\alpha}{\varepsilon_{\perp} \sin\alpha} \\ 0 \\ 1 \end{pmatrix} \tag{A.1}$$

$$|\mathbf{P}|^2 = P_0^2 + P_0^2 \frac{\varepsilon_{\parallel}^2 \cos^2\alpha}{\varepsilon_{\perp}^2 \sin^2\alpha} = 1 \tag{A.2}$$

$$P_0^2 = \frac{1}{1 + \frac{\varepsilon_{\parallel}^2 \cos^2\alpha}{\varepsilon_{\perp}^2 \sin^2\alpha}} = \frac{\varepsilon_{\perp}^2 \sin^2\alpha}{\varepsilon_{\perp}^2 \sin^2\alpha + \varepsilon_{\parallel}^2 \cos^2\alpha} \tag{A.3}$$

$$P_0 = \frac{\varepsilon_{\perp} \sin\alpha}{\varepsilon_{\text{eff}}} \tag{A.4}$$

and the electric field polarization becomes,

$$\mathbf{P} = \frac{1}{\varepsilon_{\text{eff}}} \begin{pmatrix} -\varepsilon_{\parallel} \cos\alpha \\ 0 \\ \varepsilon_{\perp} \sin\alpha \end{pmatrix}$$

where $\varepsilon_{\text{eff}} = \sqrt{\varepsilon_{\perp} \sin^2\alpha + \varepsilon_{\parallel} \cos^2\alpha}$ for $\alpha \neq 0$. For $\alpha = \pi/2$, which corresponds to a propagation vector along x, the electric field for the extraordinary wave is $\mathbf{E} = (0, 0, E_z)^T$. In case $\alpha = 0$ there will be no extraordinary wave, as it will be the same as the ordinary wave.

Wave propagation in polycrystalline ice

The single crystal permittivity at an abitrary orientation can be written as follows,

$$\boldsymbol{\varepsilon}_c(\theta, \phi) = \mathbf{R}_z^T(\phi) \mathbf{R}_y(\theta)^T \boldsymbol{\varepsilon}_c \mathbf{R}_y(\theta) \mathbf{R}_z(\phi) \Rightarrow$$

$$= \begin{pmatrix} \varepsilon_{\perp} + \Delta\varepsilon \cos^2\phi \sin^2\theta & \frac{1}{2}\Delta\varepsilon \sin 2\phi \sin^2\theta & \frac{1}{2}\Delta\varepsilon \cos\phi \sin 2\theta \\ \frac{1}{2}\Delta\varepsilon \sin 2\phi \sin^2\theta & \varepsilon_{\perp} + \Delta\varepsilon \sin^2\phi \sin^2\theta & \frac{1}{2}\Delta\varepsilon \sin\phi \sin 2\theta \\ \frac{1}{2}\Delta\varepsilon \cos\phi \sin 2\theta & \frac{1}{2}\Delta\varepsilon \sin\phi \sin 2\theta & \varepsilon_{\perp} + \Delta\varepsilon \cos^2\theta \end{pmatrix}$$

where the rotation matricies are defined as follows,

$$\mathbf{R}_y = \begin{pmatrix} \cos\theta & 0 & -\sin\theta \\ 0 & 1 & 0 \\ \sin\theta & 0 & \cos\theta \end{pmatrix} \quad \mathbf{R}_z = \begin{pmatrix} \cos\phi & \sin\phi & 0 \\ -\sin\phi & \cos\phi & 0 \\ 0 & 0 & 1 \end{pmatrix} \tag{A.5}$$

Appendix B

Data acquisition and processing

Subsample time delay

Let $\tilde{s}(\omega)$ be the Fourier transform of $s(t)$, and δt be an arbitrary time delay, then the Fourier transform of $s(t-\delta t)$ can be written as,

$$\int_{-\infty}^{\infty} s(t-\delta t)\exp(-j\omega t)dt = \int_{-\infty}^{\infty} s(u)\exp(-j\omega(u+\delta t))du, \tag{B.1}$$

where $u \equiv t-\delta t$. This can then be rewritten as,

$$\exp(-j\omega\delta t)\int_{-\infty}^{\infty} s(u)\exp(-j\omega t)du = \exp(-j\omega\delta t)\tilde{s}(\omega), \tag{B.2}$$

which shows that an arbitrary time delay can be applied to a signal, $s(t)$, by applying a phase shift to its Fourier transform.

Appendix C

Radar model

The orientation of the principal axes of $\mathbf{T}$ and $\mathbf{S}$ are described by $\theta = \theta(z)$. If we want to synthesize the rotation of the antennas at the surface, it is equivalent to doing a constant shift of θ with depth, i.e., $\theta(z) \rightarrow \theta(z) + \gamma$. In the following, we use the relation,

$$\mathbf{R}(\theta)\mathbf{R}(\gamma) = \mathbf{R}(\theta + \gamma) = \mathbf{R}(\gamma)\mathbf{R}(\theta) \tag{C.1}$$

Applying a constant shift in orientation the $\widetilde{\mathbf{T}}_n$, yield the following,

$$\begin{aligned}
\widetilde{\mathbf{T}}_n(\gamma) &= \prod_{i=1}^{n} \mathbf{R}(\theta_i + \gamma)\mathbf{T}_i\mathbf{R}(-(\theta_i + \gamma)) = \prod_{i=1}^{n} \mathbf{R}(\theta_i)\mathbf{R}(\gamma)\mathbf{T}_i\mathbf{R}(-\theta_i)\mathbf{R}(-\gamma) \\
&= \mathbf{R}(\gamma)\mathbf{R}(\theta_1)\mathbf{T}_1\mathbf{R}(-\theta_1)\mathbf{R}(-\gamma)\mathbf{R}(\gamma)\mathbf{R}(\theta_2)\mathbf{T}_2\mathbf{R}(-\theta_2)\mathbf{R}(-\gamma)\cdots \\
&= \mathbf{R}(\gamma)\prod_{i=1}^{n}\Big[\mathbf{R}(\theta_i)\mathbf{T}_i\mathbf{R}(-\theta_i)\Big]\mathbf{R}(-\gamma) = \underline{\underline{\mathbf{R}(\gamma)\widetilde{\mathbf{T}}_n\mathbf{R}(-\gamma)}}
\end{aligned} \tag{C.2}$$

We can, therefore, just rotate the operators, $\widetilde{\mathbf{T}}_n$, $\widetilde{\mathbf{T}}_n^R$ and $\widetilde{\mathbf{S}}_n$, to get a constant shift in the orientation, which is equivalent to rotating the antennas. From the model operator, $\mathbf{M}_n(\gamma)$, we can synthesize any antenna orientation by simply applying a rotation to $\mathbf{M}_n$,

$$\begin{aligned}
\mathbf{M}_n(\gamma) &= \mathbf{R}(\gamma)\widetilde{\mathbf{T}}_n^R\mathbf{R}(-\gamma)\mathbf{R}(\gamma)\widetilde{\mathbf{S}}_n\mathbf{R}(-\gamma)\mathbf{R}(\gamma)\widetilde{\mathbf{T}}_n\mathbf{R}(-\gamma) \\
&= \mathbf{R}(\gamma)\widetilde{\mathbf{T}}_n^R\widetilde{\mathbf{S}}_n\widetilde{\mathbf{T}}_n\mathbf{R}(-\gamma) = \underline{\underline{\mathbf{R}(\gamma)\mathbf{M}_n\mathbf{R}(-\gamma)}}
\end{aligned} \tag{C.3}$$

Appendix D

Double reflections

Supporting Information for "Double reflections in polarized radar data reveal ice fabric in the North East Greenland Ice Stream"

Niels F. Nymand[1], David A. Lilien[2,3], Tamara A. Gerber[1], Christine S. Hvidberg[1], Daniel Steinhage[4], Prasad Gogineni[5], Drew Taylor[5], Dorthe Dahl-Jensen[1,2]

[1]Niels Bohr Institute, University of Copenhagen

[2]Centre for Earth Observation Science, University of Manitoba

[3]Department of Earth and Atmospheric Sciences, Indiana University

[4]Alfred Wegener Institute, Helmholtz Centre for Polar and Marine Research

[5]Remote Sensing Center, University of Alabama

Contents of this file

Introduction This supporting information includes text, eight figures and one GIF.

- Text S1 explains how uncertainty estimates are calculated for the orientation results.
- Figure S1 gives a more detailed view of the double reflections at transmit and receive for HH and HV.
- Figure S2 illustrates the workflow for deriving the amplitudes and noise estimates from the radargrams needed for deriving the orientation.
- Figure S3 is a radargram from the MCoRDS radar showing double reflections near EastGRIP
- Figure S4-S8 are detailed overviews of the results derived from double reflections.
- Movie S1 is a GIF that rapidly flips the between HH and VV radargrams from Figure 1 of the main text.

Text S1: Uncertainty estimates for orientation

The HH- and VV-radargrams have up to three double reflections, each used to derive an orientation estimate. We therefore have a maximum of six independent orientation estimates. These estimates are combined into a single along-track orientation estimate for each of the four lines (A, B, C, and D). Each line is divided into three along-track sections. The mean orientation for each section is presented with the crosses and white numbers in Figure 3. The uncertainty for each section is calculated as the standard deviation multiplied by $\sqrt{6/\text{avg. \# of layers used}}$. The avg. # of layers used refer to how many double reflection layers (out of a maximum of six) are on average contributing to the orientation estimates within the section. This is done to more fairly compare between double reflection lines and give less confidence to lines with less evidence.

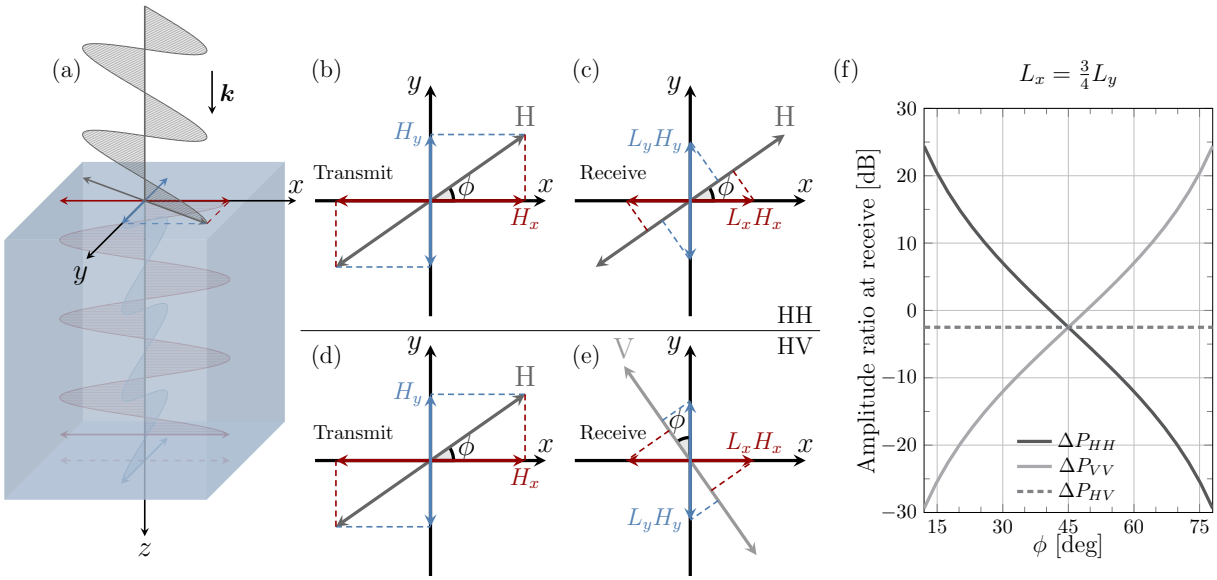

Figure S1: (a) shows an incoming linearly polarized wave in dark gray that is split into two waves, red and blue, polarized along the horizontal principal components of the COF (x, y). (b)-(e) illustrate four different polarization scenarios. (b) is transmit at the H polarization where the two waves are excited with amplitude H_x and H_y, and then later received (c) after experiencing a loss due to attenuation and scattering, L_x and L_y, while traveling through the ice. We call this HH. (d) and (e) shows the same but for the HV polarization, transmit at H and receive at V. (f) shows the ratio of the received amplitudes for the HH and HV scenarios (see equations 6 and 7 of the main text), where $L_x = \frac{3}{4}L_y$ represent anisotropic scattering or attenuation.

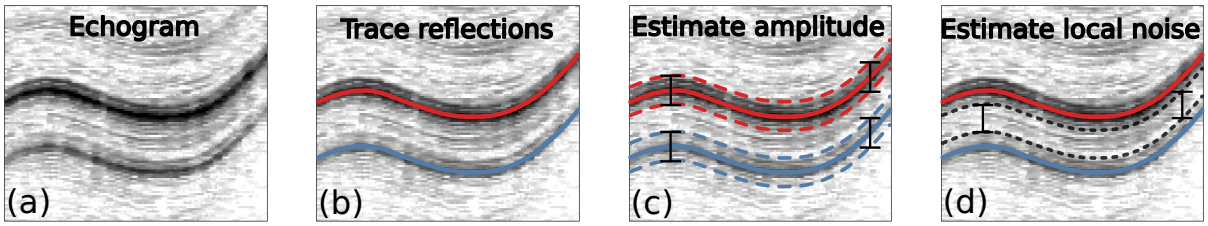

Figure S2: The workflow for deriving the amplitudes from the two reflections starts with picking the two reflections (b). Next, a window is applied around the reflections to identify the maximum value, which is used as the amplitude of the reflection (c). Finally, the region between the two reflections is used to estimate the background noise level (d).

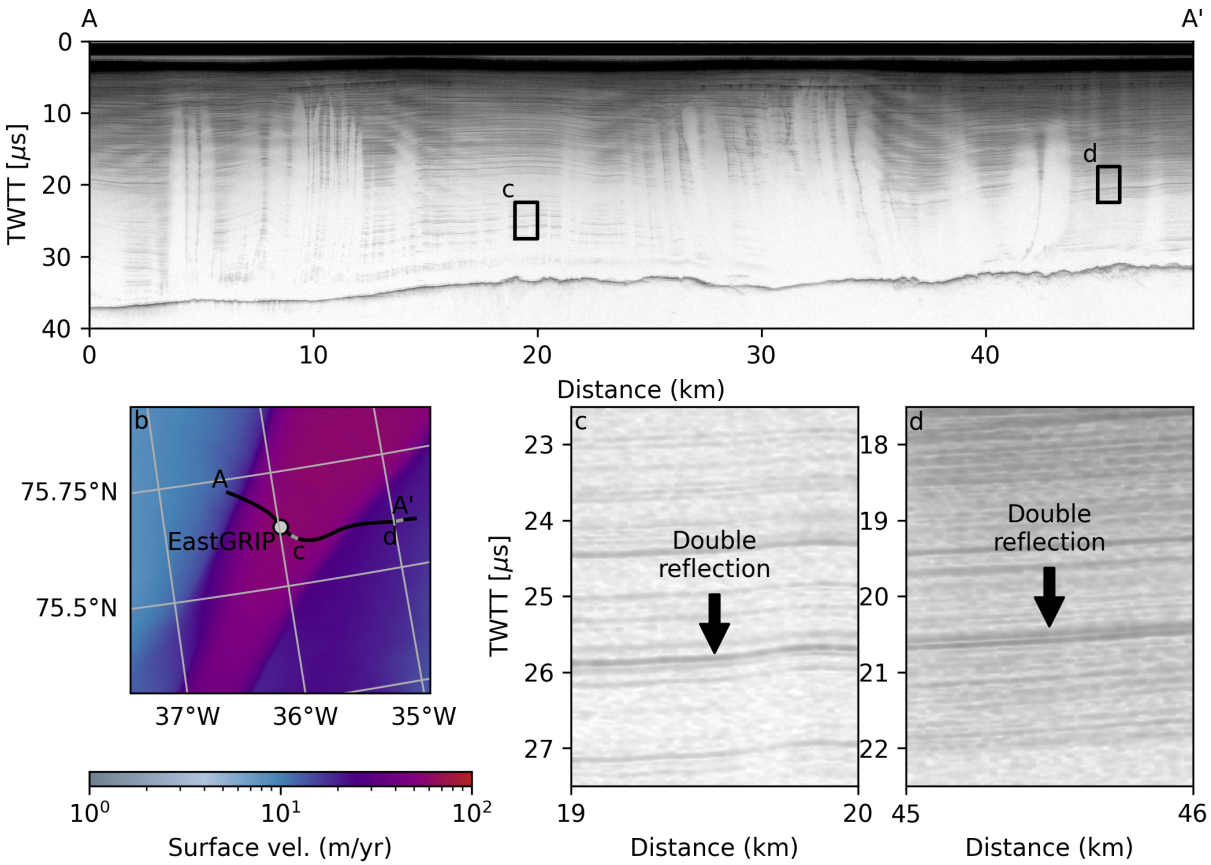

Figure S3: Radargram from MCoRDS (IRMCR1B_20190418_01_017) showing probable double reflections. The top panel displays a radargram crossing NEGIS with the two rectangular black boxes showing the outline of the zoomed radargrams in (c) and (d) with visible double reflections. (b) shows a surface velocity map of NEGIS, with the flight path in black and the along-track locations of c and d shown in gray.

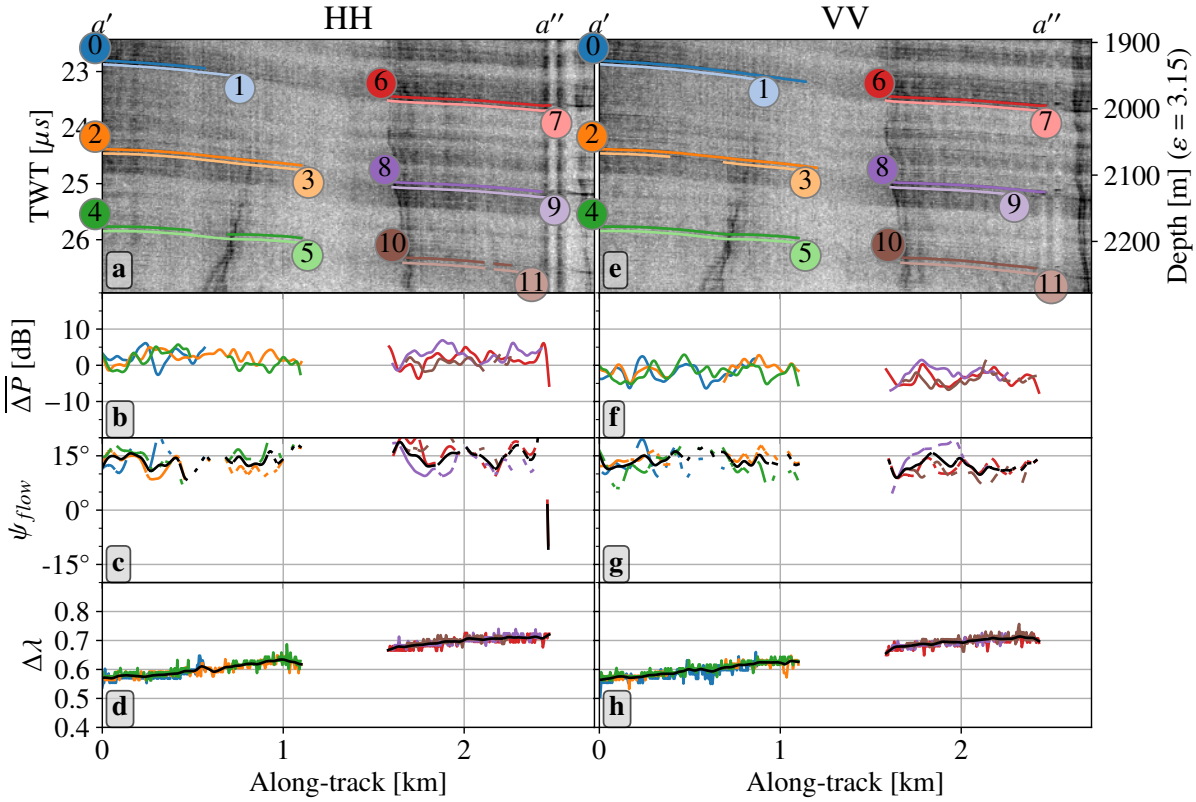

Figure S4: Detailed overview of results from the part of line 2022/06/27 that overlap with line A in Figure 1 of main manuscript. (a) HH-radargram where visible double reflections have been picked in pairs (0,1),(2,3) and so on, with the corrected amplitude differences plotted below in (b) for each layer. (c) calculated orientations of the smallest eigenvalue relative to flow for each layer with a smoothed mean plotted on top in black. (d) horizontal eigenvalue difference based on the travel-time difference of the reflection pairs picked in (a). (e)-(h) as in (a)-(d), but for VV. a' is the closest point to EastGRIP and a'' the furthest.

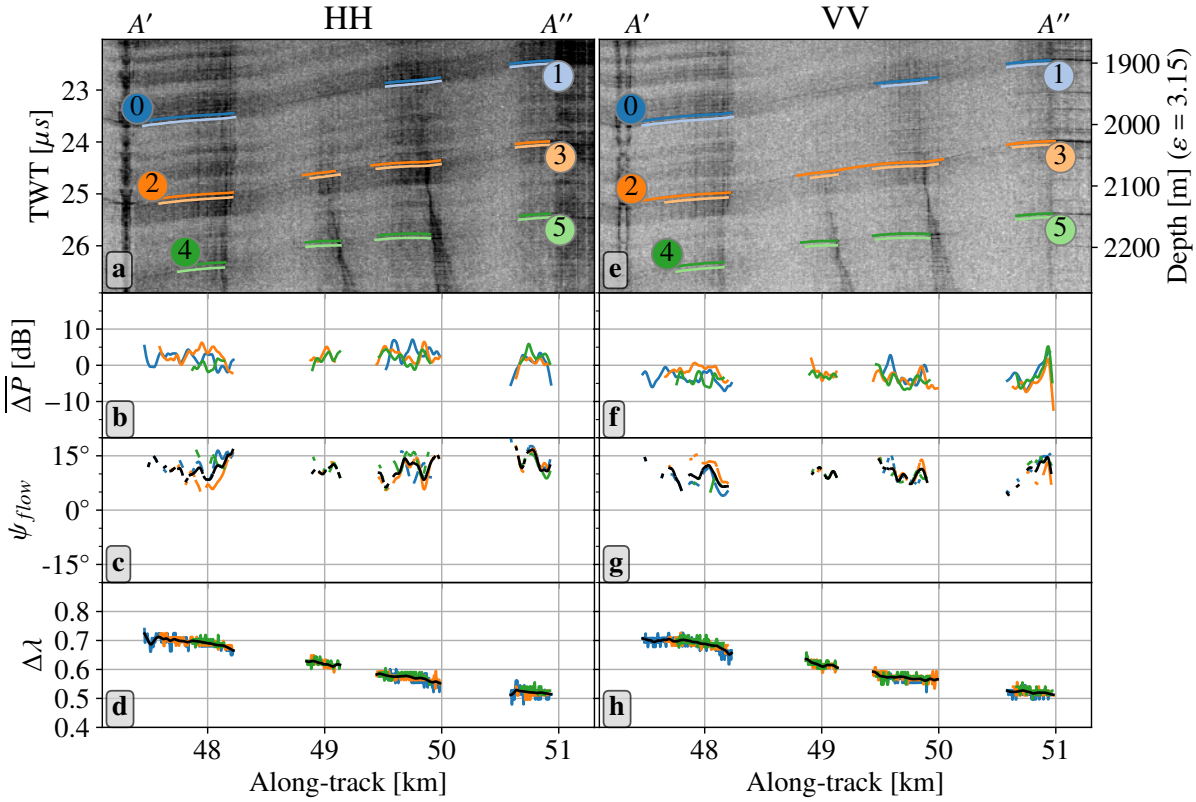

Figure S5: Detailed overview of results from line A in Figure 1 of main manuscript. (a) HH-radargram where visible double reflections have been picked in pairs (0,1),(2,3) and so on, with the corrected amplitude differences plotted below in (b) for each layer. (c) calculated orientations of the smallest eigenvalue relative to flow for each layer with a smoothed mean plotted on top in black. (d) horizontal eigenvalue difference based on the travel-time difference of the reflection pairs picked in (a). (e)-(h) as in (a)-(d), but for VV. A'' is the closest point to EastGRIP and A' the furthest.

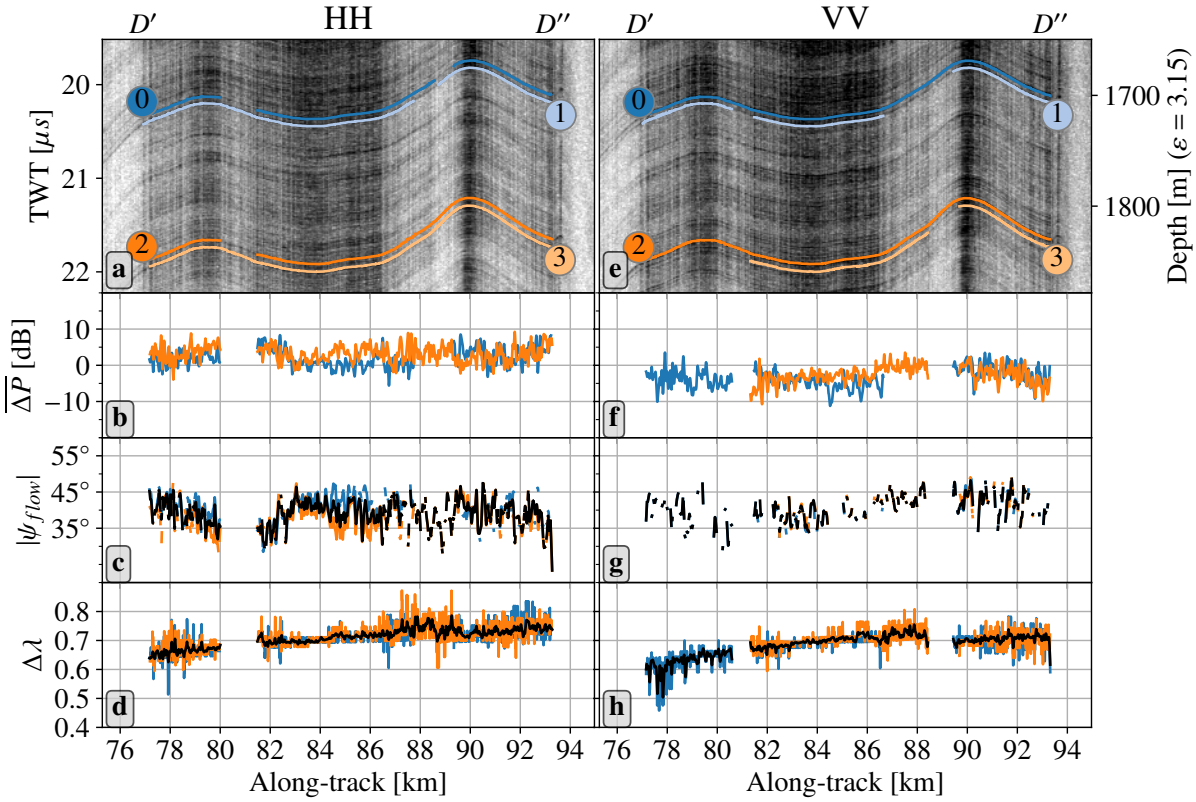

Figure S6: Detailed overview of results from line D in Figure 1 of main manuscript. (a) HH-radargram where visible double reflections have been picked in pairs (0,1) and (2,3), with the corrected amplitude differences plotted below in (b) for each layer. (c) calculated orientations of the smallest eigenvalue relative to flow for each layer with a smoothed mean plotted on top in black. (d) horizontal eigenvalue difference based on the travel-time difference of the reflection pairs picked in (a). (e)-(h) as in (a)-(d), but for VV.

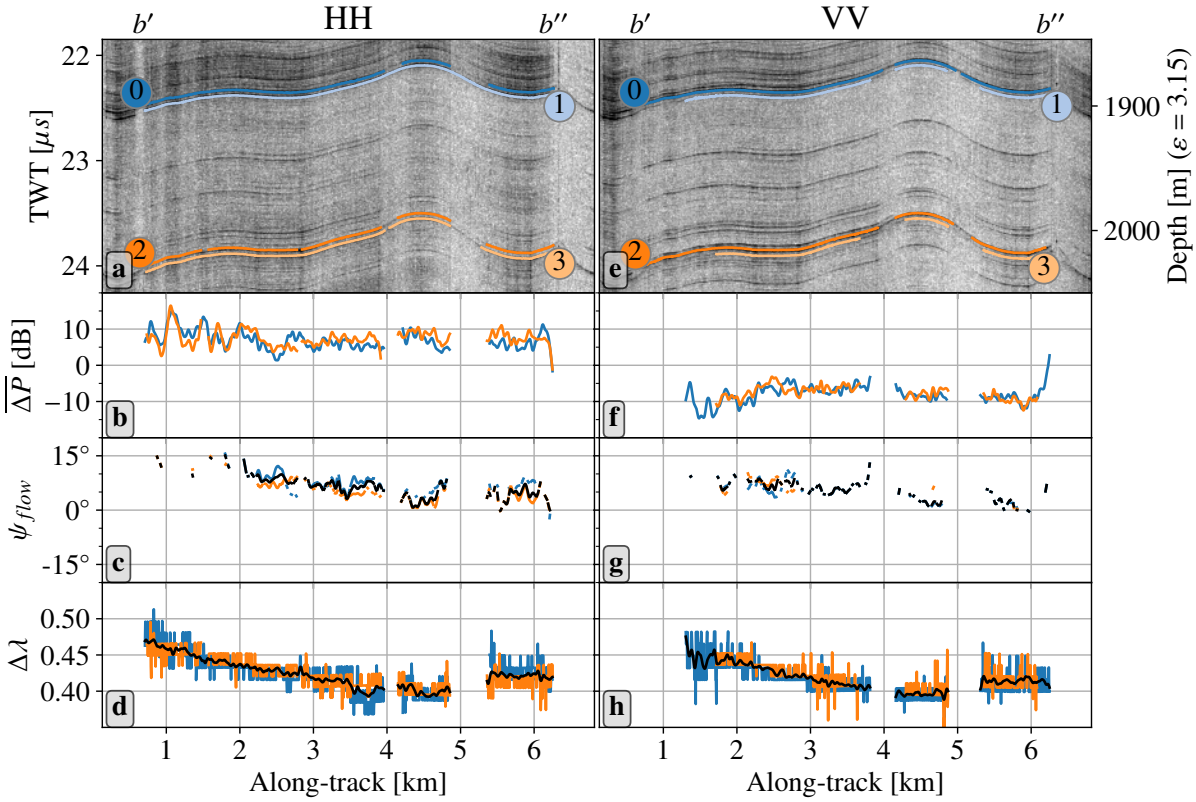

Figure S7: Detailed overview of results from the part of line 2022/07/05 that overlap with line *B* in Figure 1 of main manuscript. (a) HH-radargram where visible double reflections have been picked in pairs (0,1) and (2,3), with the corrected amplitude differences plotted below in (b) for each layer. (c) calculated orientations of the smallest eigenvalue relative to flow for each layer with a smoothed mean plotted on top in black. (d) horizontal eigenvalue difference based on the travel-time difference of the reflection pairs picked in (a). (e)-(h) as in (a)-(d), but for VV.

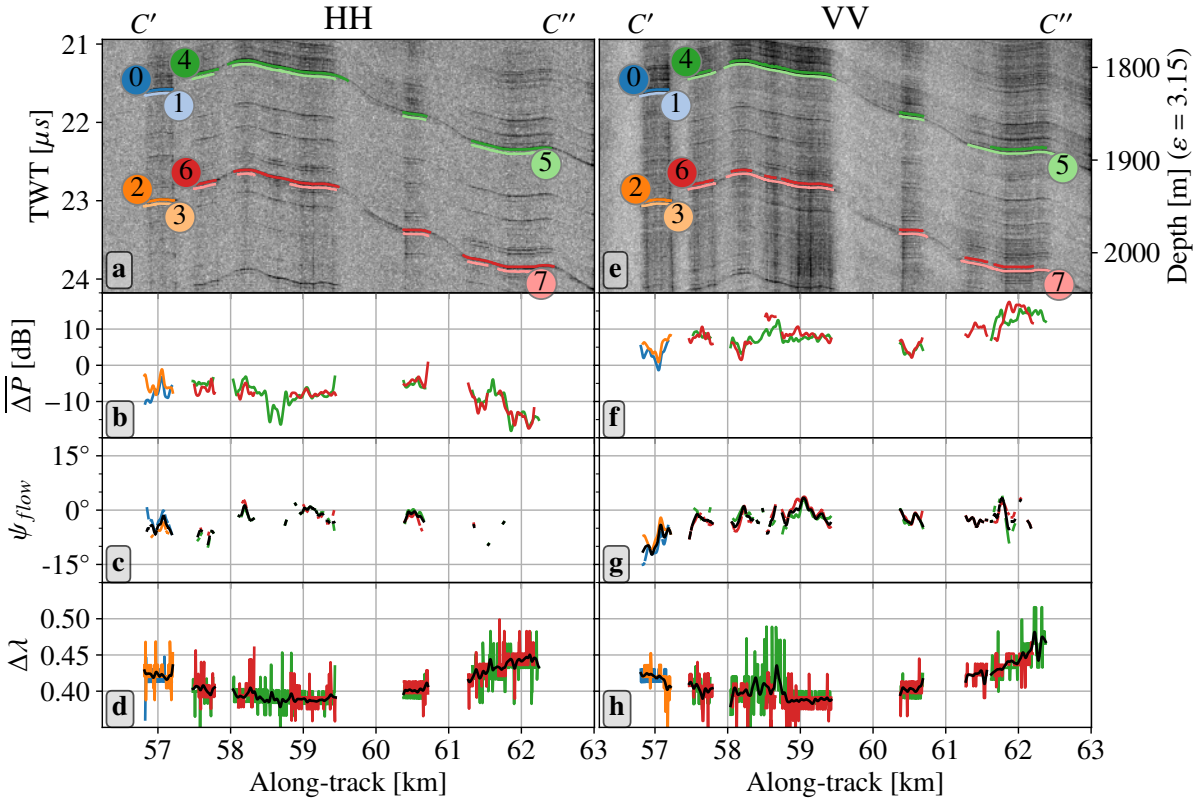

Figure S8: Detailed overview of results from line *D* in Figure 1 of main manuscript. (a) HH-radargram where visible double reflections have been picked in pairs (0,1),(2,3) and so on, with the corrected amplitude differences plotted below in (b) for each layer. (c) calculated orientations of the smallest eigenvalue relative to flow for each layer with a smoothed mean plotted on top in black. (d) horizontal eigenvalue difference based on the travel-time difference of the reflection pairs picked in (a). (e)-(h) as in (a)-(d), but for VV.

Movie S1: GIF of double reflections observed at NEGIS. Top panel is showing double reflections by rapidly flipping between the HH and VV radargrams also shown in Figure 1 of the main manuscript. The bottom panel shows the driving direction of the radar relative to flow. This demonstrated the two reflections marked by arrows stay fixed in travel-time but change amplitude when flipping between the HH and VV radargrams.

Appendix E

Polarimetric inversion

Analytical radar observables for $\theta(z) = \theta_0$

The HH power anomaly is for convenience defined defined as ($l = 2$),

$$\delta^2 P_{HH,n}(\gamma) = 20 \log_{10} \left(\frac{|s_{HH,n}(\gamma)|^2}{\frac{1}{\pi} \int_0^\pi |s_{HH,n}(\gamma')|^2 d\gamma'} \right) \tag{E.1}$$

where $|s_{HH,n}(\gamma)|^2$ can be calculated from equation 6.7,

$$\begin{aligned}
&|s_{HH,n}(\gamma)|^2 = s_{HH,n}(\gamma) s^*_{HH,n}(\gamma) \\
&= \big[\cos^2(\theta_0 - \gamma) s_{HH,n}(\theta_0) + \sin^2(\theta_0 - \gamma) s_{VV,n}(\theta_0) \big] \big[\cos^2(\theta_0 - \gamma) s^*_{HH,n}(\theta_0) + \sin^2(\theta_0 - \gamma) s^*_{VV,n}(\theta_0) \big] \\
&\propto \cos^4(\theta_0 - \gamma) S^2_{n,x} + \sin^4(\theta_0 - \gamma) S^2_{n,y} + \cos^2(\theta_0 - \gamma) \sin^2(\theta_0 - \gamma) S_{n,x} S_{n,y} \big(e^{j(\psi_{n,x} - \psi_{n,y})} + e^{-j(\psi_{n,x} - \psi_{n,y})} \big) \\
&= \cos^4(\theta_0 - \gamma) S^2_{n,x} + \sin^4(\theta_0 - \gamma) S^2_{n,y} + \tfrac{1}{2} \sin^2(2(\theta_0 - \gamma)) S_{n,x} S_{n,y} \cos(\psi_{n,x} - \psi_{n,y}) \\
&= S^2_{n,x} \Big(\cos^4(\theta_0 - \gamma) + r_n^2 \sin^4(\theta_0 - \gamma) + \tfrac{1}{2} r_n \sin^2(2(\theta_0 - \gamma)) \cos(\psi_{n,x} - \psi_{n,y}) \Big)
\end{aligned}$$

where $r_n \equiv \frac{S_{n,y}}{S_{n,x}}$. The proportionality factor is $D(z_n)^2$ but has been left out as it will be canceled out anyway. The integral then follows as,

$$\frac{1}{\pi} \int_0^\pi |s_{HH,n}(\gamma)|^2 d\gamma \propto S^2_{n,x} \frac{1}{8} \Big[3 + 3r_n^2 + 2r_n \cos(\psi_{n,x} - \psi_{n,y}) \Big]$$

Combined it yields an analyitical expression for the HH power anomaly,

$$\delta P^2_{HH,n}(\gamma) = 20 \log_{10} \Big[\frac{\cos^4(\theta_0 - \gamma) + r_n^2 \sin^4(\theta_0 - \gamma) + \frac{1}{2} r_n \sin^2(2[\theta_0 - \gamma]) \cos(\psi_{n,x} - \psi_{n,y})}{\frac{1}{8}[3 + 3r_n^2 + 2r_n \cos(\psi_{n,x} - \psi_{n,y})]} \Big]$$

The HV power anomaly is defined as,

$$\delta^2 P_{HV,n}(\gamma) = 20 \log_{10} \left(\frac{|s_{HV,n}(\gamma)|^2}{\frac{1}{\pi} \int_0^\pi |s_{HV,n}(\gamma')|^2 d\gamma'} \right) \tag{E.2}$$

where $|s_{HV,n}(\gamma)|^2$ can be calculated from equation 6.7,

$$\begin{aligned}|s_{HV,n}(\gamma)|^2 &= s_{HV,n}(\gamma)s^*_{HV,n}(\gamma)\\ =&\Big(|s_{HH,n}(\theta_0)|^2+|s_{VV,n}(\theta_0)|^2-s_{HH,n}(\theta_0)s^*_{VV,n}(\theta_0)-s^*_{HH,n}(\theta_0)s_{VV,n}(\theta_0)\Big)\cos^2(\theta_0-\gamma)\sin^2(\theta_0-\gamma)\\ &\propto S^2_{n,x}\Big(1+r_n^2-2r_n\cos(\psi_{n,x}-\psi_{n,y})\Big)\cos^2(\theta_0-\gamma)\sin^2(\theta_0-\gamma)\end{aligned}$$

The proportionality constant is $D(z_n)^2$ but has been left out as it will be canceled out anyway. The integral then follows as,

$$\frac{1}{\pi}\int_0^\pi |s_{HV,n}(\gamma)|^2 d\gamma \propto S^2_{n,x}\frac{1}{8}\Big(1+r_n^2-2r_n\cos(\psi_{n,x}-\psi_{n,y})\Big)$$

The HV power anomaly can then be written as,

$$\delta P^2_{HV,n}(\gamma) = 20\log_{10}\left[8\cos^2(\theta_0-\gamma)\sin^2(\theta_0-\gamma)\right], \tag{E.3}$$

The last observable, $\phi_{HHVV,n}(\gamma)$, can simply be expressed as, $\arg(s_{HH,n}(\gamma)s^*_{VV,n}(\gamma))$.

$$\begin{aligned}s_{HH,n}(\gamma)s_{VV,n}(\gamma)^* \propto&\Big[\cos^2(\theta_0-\gamma)e^{j\psi_{n,x}}+r_n\sin^2(\theta_0-\gamma)e^{j\psi_{n,y}}\Big]\Big[r_n\cos^2(\theta_0-\gamma)e^{-j\psi_{n,y}}+\sin^2(\theta_0-\gamma)e^{j\psi_{n,x}}\Big]\\ &= r_n\Big(\cos^4(\theta_0-\gamma)e^{j(\psi_{n,x}-\psi_{n,y})}+\sin^4(\theta_0-\gamma)e^{-j(\psi_{n,x}-\psi_{n,y})}\Big)\\ &\quad+\cos^2(\theta_0-\gamma)\sin^2(\theta_0-\gamma)\big(1+r_n^2\big)\\ =r_n\cos(\psi_{n,x}-\psi_{n,y})&\Big(\cos^4(\theta_0-\gamma)+\sin^4(\theta_0-\gamma)\Big)+\cos^4(\theta_0-\gamma)\sin^2(\theta_0-\gamma)(1+r_n)^2\\ &+jr_n\sin(\psi_{n,x}-\psi_{n,y})\Big(\cos^4(\theta_0-\gamma)-\sin^4(\theta_0-\gamma)\Big)\end{aligned}$$

The argument is then just the inverse tangent of the imaginary part divided by the real part, and slightly rewritten it becomes,

$$\phi_{HHVV,n}(\gamma) = \arctan\left[\frac{r_n\sin(\psi_{n,x}-\psi_{n,y})\big(1-\tan^4(\theta_0-\gamma)\big)}{r_n\cos(\psi_{n,x}-\psi_{n,y})\big(1+\tan^4(\theta_0-\gamma)\big)+\tan^2(\theta_0-\gamma)\big(1+r_n^2\big)}\right]$$

We see that for $\gamma=\theta_0$ the expression reduces to,

$$\phi_{HHVV,n}(\gamma=\theta_0) = \arctan\left(\frac{\sin(\psi_{n,x}-\psi_{n,y})}{\cos(\psi_{n,x}-\psi_{n,y})}\right) = \psi_{n,x}-\psi_{n,y}$$

which corresponds to the difference in the COF-aligned signal phases, as we would expect.

Jacobians

$$\frac{\partial\delta P^2_{HH,n}(\gamma)}{\partial r_n} = \frac{40}{\ln 10}\frac{\big(r_n^2-1\big)\cos(4x)\cos(y)-\cos(2x)\big(\big(r_n^2+1\big)\cos(y)+6r_n\big)}{(3r_n^2+2r_n\cos(y)+3)\big(r_n\big(2r_n\sin^4(x)+\sin^2(2x)\cos(y)\big)+2\cos^4(x)\big)}$$

$$\frac{\partial \delta P^2_{HH,n}(\gamma)}{\partial \theta_0} = \frac{40\left(4r_n^2\sin^3(x)\cos(x) + r_n\sin(4x)\cos(y) - 4\sin(x)\cos^3(x)\right)}{\log(10)\left(r_n\left(2r_n\sin^4(x) + \sin^2(2x)\cos(y)\right) + 2\cos^4(x)\right)}$$

where $x = \theta_0 - \gamma$ and $y = \psi_{n,x} - \psi_{n,y}$

$$\frac{\partial \delta P^2_{HV,n}(\gamma)}{\partial \theta_0} = \frac{40}{\ln 10}\big(\cot(\theta_0 - \gamma) - \tan(\theta_0 - \gamma)\big)$$

$$\frac{\partial \phi_{HHVV,n}(\gamma)}{\partial y} = \frac{2r_n\sec^4(x)\left(8\left(r_n^2+1\right)\cos(2x)\tan^2(x)\cos(y) + r_n\left(7\cos(2x)+\cos(6x)\right)\sec^4(x)\right)}{r_n^2\sec^8(x)\left((\cos(4x)+3)^2\cos^2(y) + 16\cos^2(2x)\sin^2(y)\right) + 8r_n\left(r_n^2+1\right)(\cos(4x)+3)\tan^2(x)\sec^4(x)\cos(y) + 16\left(r_n^2+1\right)^2\tan^4(x)}$$

where $x = \theta_0 - \gamma$ and $y = \psi_{n,x} - \psi_{n,y}$, and then,

$$\frac{\partial \phi_{HHVV,n}(\gamma)}{\partial \Delta\lambda_i} = \frac{\partial \phi_{HHVV,n}(\gamma)}{\partial y}\frac{\partial y}{\partial \Delta\lambda_i}$$

$$y = 2\sum_{i=1}^{n}\left[\Delta z_i(k_{i,x} - k_0)\right] - 2\sum_{i=1}^{n}\left[\Delta z_i(k_{i,y} - k_0)\right]$$

$$= 2\sum_{i=1}^{n}\left[\Delta z_i(k_{i,x} - k_{i,y})\right]$$

$$\left.\begin{aligned} k_{i,x} &= \tfrac{\omega}{c_0}\sqrt{\varepsilon_\perp + \Delta\varepsilon\lambda_{i,x}} \approx \tfrac{\omega}{c_0}\left(\sqrt{\varepsilon_\perp} + \tfrac{\Delta\varepsilon\lambda_{i,x}}{2\sqrt{\varepsilon_\perp}}\right) \\ k_{i,y} &= \tfrac{\omega}{c_0}\sqrt{\varepsilon_\perp + \Delta\varepsilon\lambda_{i,y}} \approx \tfrac{\omega}{c_0}\left(\sqrt{\varepsilon_\perp} + \tfrac{\Delta\varepsilon\lambda_{i,y}}{2\sqrt{\varepsilon_\perp}}\right) \end{aligned}\right\} = k_{i,x} - k_{i,y} = \frac{\omega}{c_0}\frac{\Delta\varepsilon}{2\sqrt{\varepsilon_\perp}}\Delta\lambda$$

$$y \approx \frac{\omega\Delta\varepsilon}{c_0\sqrt{\varepsilon_\perp}}\sum_{i=1}^{n}\Delta z_i\Delta\lambda_i$$

$$\frac{\partial y}{\partial \Delta\lambda_k} = \frac{\omega\Delta\varepsilon}{c_0\sqrt{\varepsilon_\perp}}\Delta z_k$$

and finally,

$$\frac{\partial \phi_{HHVV,n}(\gamma)}{\partial \Delta\lambda_i} = \frac{\partial \phi_{HHVV,n}(\gamma)}{\partial y}\frac{\omega\Delta\varepsilon}{c_0\sqrt{\varepsilon_\perp}}\Delta z_i$$